

Dynamic States in Rotating Rayleigh-Bénard Convection Systems

Thesis by

Eugenia Y. Kuo

In Partial Fulfillment of the Requirements

for the Degree of

Doctor of Philosophy

California Institute of Technology

Pasadena, California

1994

(Defended January 7, 1994)

© 1994

Eugenia Y. Kuo

All Rights Reserved

Acknowledgments

It gives me great pleasure to thank my advisor Prof. Mike Cross, whose guidance and patience over the years have made this thesis possible. From the very beginning, his insights and intuition have never ceased to amaze me, yet he has never sought to impose his ideas, allowing me the freedom to choose my own way. However, he was always ready to help with problems and guide with ideas.

I also want to thank Prof. Dan Meiron and Dr. Yuhai Tu for their efforts and ideas in making this thesis possible. I have enjoyed learning from both of them.

I also wish to thank Prof. Nai-Chang Yeh for her concern over the past few years.

Pat Stevens, who has made the atmosphere in Sloan Annex a friendly and warm one, has also always been very helpful. For this I would like to say *Thanks!*

I also wish to thank the many friends I have had at Caltech, without whom life would have been much more barren. Amongst these, I would especially like to mention Dr. Marissa La Madrid and Dr. Glen and Max Herrmannsfeldt, Dr. Chungyu Mou, Sima Setayeshgar, and Wei Zheng.

Finally, but certainly not least, I want to thank my family and Craig for their unconditional support and encouragement. Without them this thesis would not be here – Dean and Craig in particular know this full well even in a literal sense, having helped me put it all together at the very end!

Dynamic States in Rotating Rayleigh-Bénard Convection Systems

by

Eugenia Y. Kuo

Advisor: Dr. Michael C. Cross

Abstract

A new geometry-independent state – a traveling-wave wall state – is proposed as the mechanism whereby which the experimentally observed wall-localized states in rotating Rayleigh-Bénard convection systems preempt the bulk state at large rotation rates. Its properties are calculated for the illustrative case of free-slip top and bottom boundary conditions. At small rotation rates, this new wall state is found to *disappear*. A detailed study of the dynamics of the wall state and the bulk state in the transition region where this disappearance occurs is conducted using a Swift-Hohenberg model system. The Swift-Hohenberg model, with appropriate reflection-symmetry-breaking boundary conditions, is also shown to exhibit traveling-wave wall states, further demonstrating that traveling-wave wall states are a generic feature of nonequilibrium pattern-forming systems. A numerical code for the Swift-Hohenberg model in an annular geometry was written and used to investigate the dynamics of rotating Rayleigh-Bénard convection systems.

Contents

1	Introduction	1
1.1	Schematic Experimental Set-Up and Equations of Motion in Rayleigh-Bénard Convection Systems	4
1.2	Linear Stability or Instability Analysis	6
1.3	Amplitude Equations	9
2	Motivation and Background	11
3	Traveling-Wave Wall State in Rotating Rayleigh-Bénard Convection	16
3.1	Linear Stability Analysis	16
3.1.1	Equations of Motion and Boundary Conditions	16
3.1.2	Method of Solution	19
3.1.3	Results	23
3.1.4	Asymptotic Results	30
3.2	Amplitude Equation for the Traveling-Wave Wall State	34
4	Swift-Hohenberg Models	39

4.1	Swift-Hohenberg Model with Reflection-Symmetry-Breaking Boundary Conditions	41
4.1.1	Reflection-Symmetry-Breaking Boundary Conditions	41
4.1.2	Linear Instability Analysis for the Traveling-Wave Wall State	42
4.2	Küppers-Lortz Instability	45
4.2.1	Modified Swift-Hohenberg Model	51
4.3	Amplitude Equation for the Traveling-Wave Wall State	54
4.3.1	Calculation of the (lowest order) Nonlinear Coefficient in the Amplitude Equation	54
4.3.2	Solving for the Kernel of the Adjoint Operator	61
4.4	Numerical Study of the Traveling-Wave Wall State in the Swift-Hohenberg Model	66
4.4.1	Numerical Algorithm	67
4.4.2	Grid Selection in the y -direction	72
4.4.3	An (Unexplained) Observed Nonlinear Instability	75
4.5	The Wall State – Bulk State Transition	78
4.5.1	Numerical Study	80
4.5.2	The Phase Diagram and the Various States	81
	The Wall State	82
	The Wall-plus-Bulk State	87
	The Oscillating One-State	90

The Steady One-State	91
4.5.3 A Detailed Study of the Nonlinear Steady-State Frequency at $q_x = 1.2$	95
4.5.4 A Study of the Nonlinear Steady-State Frequency at $q_x = 1.278$	100
4.5.5 An Amplitude Equation to Describe the Dynamics	103
4.5.6 Solutions to the Amplitude Equation	105
4.5.7 Implications	108
4.5.8 Dynamical Mode Equations for the Boundary Region	111
4.5.9 Numerical Study of the Dynamical Mode Equations	115
 5 Conclusion and Future Work	 128
 A The Thermal Boundary Condition	 134
 References	 137

List of Figures

1-1	Schematic picture of a bulk roll pattern of infinite extent in a Rayleigh-Bénard convection system. (Reprint from Fig. 9 of [8].)	2
1-2	Schematic representation of the linear growth rate $\gamma = Re \sigma$ as a function of the wave vector q for different values of the control parameter $R \sim \epsilon$. (Reprint from [1].)	7
2-1	Principle of the shadowgraphic method. (Reprint from Fig. 10 of reference [8].)	14
2-2	Shadowgraph image of a convection pattern below the bulk onset Rayleigh number. (Reprint fom Fig. 7 of reference [13].)	14
3-1	Critical Rayleigh number as a function of the rotation rate Ω for different sidewall thermal boundary conditions for Prandtl number $\sigma = 6.4$.	24
3-2	Critical frequency ω_c for the same conditions as in Fig.(3-1).	25
3-3	Critical wave vector q_{xc} for the same conditions as in Fig.(3-1).	26

3-4	Critical Rayleigh number as a function of the wave number q_x for the fixed rotation rate $\Omega = 10$. The Prandtl number $\sigma = 6.4$, and the sidewall is perfectly insulating ($\mu = 0$). The point at which the wall state solution 'disappears' is indicated by a cross.	27
3-5	Normal wave vectors q_y for the same conditions as in Fig.(3-4).	28
3-6	Critical frequency for the same conditions as in Fig.(3-4).	29
3-7	Critical Rayleigh number, frequency and wave number and their asymptotic limits (the dashed lines) for the experimental sidewall thermal boundary conditions.	33
3-8	Amplitude equation time scale parameter τ_0 for the same conditions as in Fig.(3-1).	36
3-9	Amplitude equation group velocity s for the same conditions as in Fig.(3-1).	36
3-10	Amplitude equation length scale parameter ξ_0 for the same conditions as in Fig.(3-1).	37
3-11	Amplitude equation parameter c_0 for the same conditions as in Fig.(3-1).	37
3-12	Amplitude equation parameter c_1 for the same conditions as in Fig.(3-1).	38
4-1	Critical ϵ , ϵ_c , as a function of μ for $\lambda = -0.1$ for the wall state in the Swift-Hohenberg model. The critical onset solution for the wall state disappears when $\mu = \mu^*$ at the point denoted by a cross.	44
4-2	Critical frequency ω_c for $\lambda = -0.1$	44

4-3	Critical wave number q_{xc} for $\lambda = -0.1$	46
4-4	Critical wave numbers normal to the wall, q_y , for $\lambda = -0.1$	46
4-5	Critical ϵ as a function of q_x for $\lambda = -0.1$, $\mu = -15$. The point at which the wall state solution disappears is indicated by a cross.	47
4-6	Critical frequency as a function of q_x for $\lambda = -0.1$, $\mu = -15$	47
4-7	Critical q_y as a function of q_x for $\lambda = -0.1$, $\mu = -15$	48
4-8	Group velocity s in the amplitude equation for $\lambda = -0.1$	55
4-9	Length scale parameter ξ_0 in the amplitude equation for $\lambda = -0.1$	55
4-10	Amplitude equation parameter c_1 for $\lambda = -0.1$	56
4-11	Nonlinear coefficient scaling factors c_{g_i} for the amplitude equation when $\lambda = -0.1$	64
4-12	Nonlinear coefficient G for $g_1 = 1$, $g_2 = -2.078$, and $g_3 = 1.2$ when $\lambda = -0.1$	65
4-13	The quantity $1 + c_1 c_3$ in the Newell criterion for the Benjamin-Feir instability (see text), for the same parameters as in Fig.(4-12).	66
4-14	Schematic diagram for the numerical algorithm.	71
4-15	Wall state: For parameters see text. System size is $l_x = 128$, $l_y = 30$; grid is $\Delta x = 1$, $\Delta y = 1/3$ in both the boundary and bulk regions. The x -axis is from left to right, and the y -axis is from top to bottom. The wall state at $y = 0$ is traveling to the left (negative phase velocity), and that at $y = l_y$ is traveling to the right.	73

4-16	Fourier spectra at different times t at $y = 1.5$ for the initial condition $\psi_0 = 10^{-4} \sin(0.392699x)$ and $\epsilon = -0.02$; $\Delta x = 0.5$, and in the boundary region $\Delta y = 0.25$. (For more details see text.)	76
4-17	$\psi(t)$ at $(x = 4, y = 0)$ for various grids (Δy is for the boundary region).	77
4-18	Critical ϵ , ϵ_c^W , and critical frequency, ω_c , for the wall state for $\lambda = -0.6$ and $\mu = -10$. The point at which the wall state disappears is indicated by a cross. The wave number at which this occurs is q_x^* . Also shown is the critical ϵ , ϵ_c^B , for the bulk state.	79
4-19	The phase diagram for the wall state – bulk state transition region for $\lambda = -0.6$ and $\mu = -10$	83
4-20	Wall state: (a) $\psi(x,y)$ for $t = 1000$, $q_x = 1.2$ and $\epsilon = 0.19$. (x -axis is from left to right, y -axis from top to bottom.) Also note that the boundary regions are to a larger scale ($6\times$). The array density is $30 + 140 + 30$ for lengths of $5 + 140 + 5$. (b) $\psi(y,t)$ for $x = l_x/4$ and $0 \leq t \leq 1000$; the y -axis is from left to right, and the t -axis is from bottom to top. (c) $\psi(x,t)$ for $y = 0$ and $0 \leq t \leq 1000$; the x -axis is from left to right.	85
4-21	$\psi(t)$ for $(x,y) = (l_x/4,1)$ for the wall state in Fig.(4-20).	86
4-22	Frequency spectrum for Fig.(4-21) for $255 \leq t \leq 1000$	86

4-23	Wall-plus-bulk state: $q_x = 1.24$ and $\epsilon = 0.34$. (a) $\psi(x,y)$ for $t = 3000$. (b) $\psi(y,t)$ for $x = l_x/4$ and for $0 \leq t \leq 3000$. (c) $\psi(x,t)$ for $y = 1$ and $0 \leq t \leq 3000$. (d) For $y = 75$	88
4-24	$\psi(t)$ for $(x,y) = (l_x/4,1)$ for the wall-plus-bulk state in Fig.(4-23). . .	89
4-25	Frequency spectrum for $(x,y) = (l_x/4,1)$ and $1000 < t \leq 3000$; for the wall-plus-bulk state in Fig.(4-23).	90
4-26	Oscillating one-state: $q_x = 1.28$ and $\epsilon = 0.44$. (a) $\psi(x,y)$ for $t = 3000$. (b) $\psi(y,t)$ for $x = l_x/4$ and for $0 \leq t \leq 3000$. (c) $\psi(x,t)$ for $y = 1$ and $0 \leq t \leq 3000$. (d) For $y = 75$	92
4-27	$\psi(t)$ for $x = l_x/4$ and $y = 1$ and $y = 75$; for the oscillating one-state in Fig.(4-26).	93
4-28	$\psi(t)$ for $x = l_x/4$ and $y = 0$ and $y = 75$; for the steady state in Fig.(4-29). . .	93
4-29	Steady one-state: $q_x = 1.28$ and $\epsilon = 0.43$. (a) $\psi(x,y)$ for $t = 13,000$. (b) $\psi(x,t)$ for $y = 0$ and for $0 \leq t \leq 13,000$. (c) $\psi(y,t)$ for $x = l_x/4$ and for $0 \leq t \leq 13,000$	94
4-30	Nonlinear frequency ω as a function of ϵ at $q_x = 1.2$	96
4-31	$\psi(t)$ for $(x,y) = (l_x/4,1)$ at $q_x = 1.2$ and $\epsilon = 0.3483$	97
4-32	Part of the frequency spectrum for Fig.(4-31).	98
4-33	Fit to the data of Fig.(4-30) near the bifurcation point.	99
4-34	Nonlinear frequency ω and the type of steady-state as a function of ϵ at $q_x = 1.278$	101

4-35 (a) $\psi(x, y)$ at a time when the whole boundary region becomes near zero in amplitude. Here $q_x = 1.278, \epsilon = 0.445$. (b) $\psi(x, t)$ at $y = 0$. $\Delta T = 600$ for this sequence. (This is actually an oscillating one-state.) 102

4-36 $q_x = -0.1, \bar{\epsilon} = -0.36$. “Wall state” trajectory: (a) complex A-plane; (b) $Re(A) \sim \psi$ vs t ; (c) complex \tilde{A}_W -plane; (d) $a_B \cos \phi_B$ vs t . (For details see text.) 117

4-37 $q_x = -0.1, \bar{\epsilon} = -0.31$. “Wall-plus-bulk state” trajectory: (a) A-plane; (b) $Re(A) \sim \psi$ vs t ; (c) \tilde{A}_W -plane; (d) $a_B \cos \phi_B$ vs t 118

4-38 $q_x = -0.1, \bar{\epsilon} = -0.11$. “Wall-plus-bulk state” trajectory: (a) A-plane; (b) $Re(A) \sim \psi$ vs t ; (c) \tilde{A}_W -plane; (d) $a_W \cos \phi_W$ vs t 119

4-39 $q_x = -0.1, \bar{\epsilon} = -0.06$. “Steady one-state” trajectory: (a) $Re(A) \sim \psi$ vs t ; (b) $a_W \cos \phi_W$ vs t ; (c) $a_B \cos \phi_B$ vs t 120

4-40 $q_x = -0.02, \bar{\epsilon} = -0.0795$. “Steady one-state” trajectory: (a) A-plane; (b) $Re(A) \sim \psi$ vs t ; (c) \tilde{A}_W -plane. 121

4-41 $q_x = -0.02, \bar{\epsilon} = -0.07$. “Oscillating one-state” trajectory: (a) A-plane; (b) $Re(A) \sim \psi$ vs t ; (c) \tilde{A}_W -plane; (d) \tilde{A}_B -plane. 122

4-42 $q_x = -0.02, \bar{\epsilon} = -0.04$. “Wall-plus-bulk state” trajectory: (a) A-plane; (b) $Re(A) \sim \psi$ vs t ; (c) $a_W \cos \phi_W$ vs t ; (d) $a_B \cos \phi_B$ vs t 123

4-43 $q_x = -0.02, \bar{\epsilon} = -0.01$. “Steady one-state” trajectory: (a) $Re(A) \sim \psi$ vs t ; (b) $a_W \cos \phi_W$ vs t ; (c) $a_B \cos \phi_B$ vs t 124

4-44 $q_x = -0.005, \tilde{\epsilon} = -0.0185$. “Steady one-state” trajectory: (a) A-plane;
 (b) $Re(A) \sim \psi$ vs t ; (c) \tilde{A}_W -plane; (d) \tilde{A}_B -plane. 125

4-45 $q_x = -0.005, \tilde{\epsilon} = -0.017$. “Steady one-state” trajectory: (a) A-plane;
 (b) $Re(A) \sim \psi$ vs t ; (c) \tilde{A}_W -plane; (d) \tilde{A}_B -plane. 126

4-46 $q_x = -0.005, \tilde{\epsilon} = 0$. “Steady one-state” trajectory: $Re(A) \sim \psi$ vs t 127

5-1 $\psi(t)$ for $(x, y) = (l_x/4, 1)$ and $(l_x/2, l_y - 1)$ 130

5-2 $\psi(x, y)$ for $\epsilon = 0.2, \lambda = -0.1, \mu = -8, g_1 = 1, g_2 = 2.078$ and $g_3 = 1.2$;
 the system size is $l_x = 64, l_y = 85$ and grid points in the y-direction of
 50 + 35 + 50 for lengths of 25 + 35 + 25. 131

5-3 (a) $\psi(x, t)$ for $y = 49$; (b) $\psi(y, t)$ for $x = 32$; for the system of Fig.(5-2).
 Total time is about 1000. 132

A-1 Coordinate system for sidewall - fluid boundary 135

Chapter 1

Introduction

‘Patterns’ are seen in myriad aspects of nature, from snowflakes, sand dunes, and billowing clouds, to perhaps the grandest and most interesting of all – biological patterns. Indeed, one may ask the question, “What is a pattern?”

There is then the question of how patterns form. Progress has been made in answering this question for many classes of patterns in recent years. One such class of patterns are those which arise from homogeneous states due to the existence of linear instabilities [1]. This class includes Rayleigh-Bénard convection roll patterns, Turing patterns or patterns arising in reaction-diffusion systems, and Taylor-Couette flow. The common feature of this class of patterns is the initial instability of a state with spatial structure $e^{i\vec{q}\cdot\vec{x}}$, which grows and usually saturates. The evolution of the final pattern however, depends on many different factors, among them nonlinear effects, the influence of boundaries, and noise. It is in attempting to understand these effects that much work has been expended. It is also for these reasons that much work has concentrated on Rayleigh-Bénard convection systems, a system for which the basic ‘microscopic’ equations (in this case the fluid equations) are well known, and for

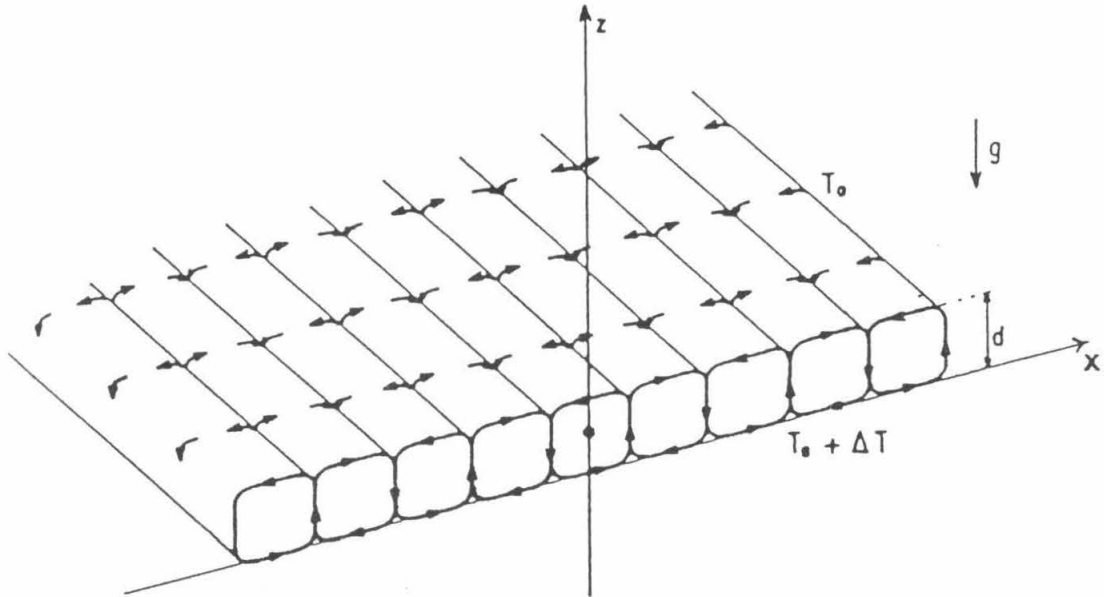


Figure 1-1: Schematic picture of a bulk roll pattern of infinite extent in a Rayleigh-Bénard convection system. (Reprint from Fig. 9 of [8].)

which well-controlled quantitative experiments are possible. This enables a rigorous comparison of theory and experiment in the testing of theories, models, and concepts.

One such concept is that of a geometry-independent ‘bulk’ state in an idealized, infinite, unbounded system [1, 2, 4]. By a ‘bulk’ state, we usually mean that a ‘pattern’ of ‘non-finite’ extent with spatial variation $e^{i\vec{q}\cdot\vec{x}}$ is formed. A standard example is the formation of convection rolls in a Rayleigh-Bénard convection system, where the wave number of the roll pattern is q . A schematic picture of a Rayleigh-Bénard convection roll pattern may be seen in Fig.(1-1).

In this thesis, it will be shown that another type of geometry-independent state – a wall-localized ‘wall’ state – can exist in nonequilibrium pattern-forming systems.

In analogy with the ‘bulk’ state mentioned above, it exists in a semi-infinite system – that is, a system bounded only by one straight, infinite sidewall.

The existence of such wall-localized states induced by the boundary conditions was previously suggested by Kramer and Hohenberg [5] based on general arguments. In [6], wall-localized solutions of traveling-wave amplitude equations with general boundary conditions were also found. It was not clear though, whether these solutions could exist in a physical system.

We will first demonstrate the existence of wall states in a real, physical system, namely in a rotating Rayleigh-Bénard convection system. Then we will use a model pattern-forming system (the Swift-Hohenberg model) with boundary conditions; by incorporating the essential features that lead to the existence of wall states, we shall show that wall states can be a generic feature of pattern-forming systems. The model system will also be investigated numerically to elucidate the nature of various aspects of the wall state, for example, the transition from wall to bulk state.

The influence of ‘walls’ or boundaries on patterns is a multifaceted question. In [30], for example, it was shown that even in a large laterally finite container, the allowed band of wave vectors is reduced from that of an ideal infinite system. The existence of wall states adds another dimension to the question, not only of its own merit, but also because it inspires the broader question of its influence on bulk patterns.

A natural system for such a study turns out to be rotating Rayleigh-Bénard con-

vection, a simple system which nonetheless possesses enough ingredients for a substantive study of dynamical patterns – of dynamical wall states, dynamical bulk states, and their interactions.

1.1 Schematic Experimental Set-Up and Equations of Motion in Rayleigh-Bénard Convection Systems

In a typical Rayleigh-Bénard convection experiment, a thin layer of fluid is sandwiched between two horizontal plates of good thermal conductivity relative to the fluid. The two plates are maintained at constant temperatures, with the lower plate at a higher temperature than the upper one. The (positive) temperature difference is ΔT . When the temperature difference ΔT is less than a certain critical temperature difference ΔT_c , the buoyancy force that drives convection is insufficient to overcome the thermal and viscous dissipation, and the stable state is one in which there is no convection, but a constant linear temperature gradient between the two plates, where heat is uniformly conducted from the lower to the upper plate. When $\Delta T > \Delta T_c$ however, the linear conduction state becomes unstable, and convection sets in. This is illustrated in Fig.(1-1).

It is usual to write the equations of motion describing the fluid in dimensionless variables. In the usual ones, length is measured in units of the cell height d , time

in units of the thermal diffusion time d^2/κ (where κ is the thermal diffusivity of the fluid), and temperature in units of $\kappa\nu/\alpha g d^3$ (ν is the kinematic viscosity, α the coefficient of thermal expansion, and g the gravitational acceleration). In these units, the equations of motion for the fluid velocity $\vec{v} = (u, v, w)$, the deviation of the temperature from its linear conduction profile, θ , the deviation of the pressure from its conduction profile, p , and the incompressibility condition, are

$$\sigma^{-1} \left[\frac{\partial \vec{v}}{\partial t} + (\vec{v} \cdot \vec{\nabla}) \vec{v} \right] = -\sigma^{-1} \vec{\nabla} \left(\frac{p}{\rho_0} \right) + \theta \hat{z} + \nabla^2 \vec{v} \quad (1.1)$$

$$\frac{\partial \theta}{\partial t} + (\vec{v} \cdot \vec{\nabla}) \theta = R w + \nabla^2 \theta \quad (1.2)$$

$$\vec{\nabla} \cdot \vec{v} = 0. \quad (1.3)$$

Here $R = \alpha g (\Delta T) d^3 / \kappa \nu$ is the Rayleigh number, and $\sigma = \nu / \kappa$ is the Prandtl number, while ρ_0 is the mean fluid density.

The above equations are derived from the Navier-Stokes equation and the heat equation, and are the well-known Oberbeck-Boussinesq equations, in which all fluid properties except the fluid density are regarded as constant, and variations in the density are included only when coupled to gravity, *i.e.*, involve the buoyancy force [3].

1.2 Linear Stability or Instability Analysis

We shall use the Rayleigh-Bénard convection system described above as a prototypical example of a pattern-forming system in which the formation of spatial pattern is governed by the change in the linear stability of a Fourier mode $e^{i\vec{q}\cdot\vec{x}}$, as a control parameter, commonly denoted by R , is varied. (In Rayleigh-Bénard convection the control parameter is the Rayleigh number.) As the control parameter is increased beyond a critical value R_c , a mode $\sim e^{i\vec{q}_c\cdot\vec{x}}$ ($q_c \neq 0$) becomes unstable and grows in amplitude, giving rise to a pattern with wave number q_c .

If we write the growth rate of any Fourier mode $e^{i\vec{q}\cdot\vec{x}}$ as $\gamma(q)$, (*i.e.*, the spatial and temporal variation of the mode is $e^{\gamma(q)t}e^{i\vec{q}\cdot\vec{x}}$) then when $R < R_c$, the growth rates of all modes are negative ($\gamma(q) < 0, \forall q$), and any instability will eventually decay away. If $R = R_c$, then one mode $e^{i\vec{q}_c\cdot\vec{x}}$ has zero growth rate, while all other modes have negative growth rates. And when $R > R_c$, a band of wave numbers centered about q_c have positive growth rates, and instabilities of wave number $q \approx q_c$ will grow (until nonlinear effects saturate the growth), and a spatial pattern with wave number $q \approx q_c$ will form. This is illustrated in Fig.(1-2). (This scenario is generally valid in the weakly nonlinear regime, where R is not too much larger than R_c .)

When studying the unstable convection modes in the Rayleigh-Bénard system, one must also consider the boundary conditions at the top and bottom plates. The two most commonly considered types of boundary conditions are the rigid (or no-slip) boundary conditions, and the free-slip boundary conditions. For both of these

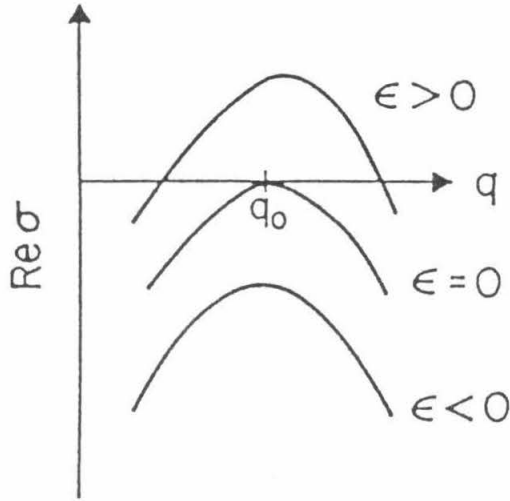


Figure 1-2: Schematic representation of the linear growth rate $\gamma = \text{Re } \sigma$ as a function of the wave vector q for different values of the control parameter $R \sim \epsilon$. (Reprint from [1].)

sets of boundary conditions, the thermal boundary condition is $\theta = 0$, owing to the fact that the plates are much better thermal conductors than the fluid. The fluid velocity boundary conditions though, differ. For the rigid boundary conditions, the fluid velocity is zero at the boundary ($u = v = w = 0$), and is the more physical. But the free-slip boundary conditions, where the normal velocity and the tangential stresses are zero ($w = \frac{\partial u}{\partial z} = \frac{\partial v}{\partial z} = 0$), is the more tractable one analytically. For this reason, the free-slip top and bottom boundary conditions are commonly used in the study of pattern formation problems in Rayleigh-Bénard convection, as they are usually sufficient to illustrate the basic behavior.

For free-slip boundary conditions, the most unstable onset mode with spatial

dependence $e^{i\vec{q}\cdot\vec{x}}$ is found by writing the physical variables as

$$\chi(x, y, z) = e^{i(q_x x + q_y y)} \begin{pmatrix} U_0 \cos \pi z \\ V_0 \cos \pi z \\ W_0 \sin \pi z \\ \Theta_0 \sin \pi z \end{pmatrix} + c.c.. \quad (1.4)$$

The coordinate system used is one in which the height of the cell is from $z = 0$ to $z = 1$, and the x and y directions extend laterally to infinity. By taking the physical variables to be of this form, the boundary conditions at the top and bottom ($\theta = w = \frac{\partial u}{\partial z} = \frac{\partial v}{\partial z} = 0$) are automatically satisfied. This is the advantage of using free-slip boundary conditions.

To find the critical Rayleigh number $R(q)$ for given q , one substitutes (1.4) into linearized versions of (1.1) to (1.3) and solves a determinant condition to find $R(q)$. The dependence $R(q)$ is known as the neutral stability curve. Minimizing $R(q)$ with respect to q leads to the critical Rayleigh number R_c and the critical wave number q_c . For free-slip boundary conditions, $R_c = 27\pi^4/4 = 657.511$, and $q_c = \pi/\sqrt{2} = 2.2214$. (For rigid boundary conditions $R_c = 1701.762$, and $q_c = 3.117$ [4].)

Thus for $R > R_c$, a bulk convection roll pattern of wave number $q = q_c$ arises in a convection cell of lateral size L large compared to q_c^{-1} . This is a standard example of a bulk state driven by a linear instability in a pattern-forming system.

1.3 Amplitude Equations

As mentioned in §1.2, when $R > R_c$, a *band* of wave numbers centered about q_c grows. The width of this band of unstable wave numbers Δq depends upon $\Delta R = R - R_c$. It is usual to define a reduced control parameter $\epsilon = \frac{(R-R_c)}{R_c}$, and when ϵ is small, $\Delta q \sim \epsilon^{\frac{1}{2}}$. This is due to the growth rate of any wave number close to q_c being

$$\gamma(q_c + \Delta q) = \gamma(q_c) - \tau_0^{-1} \xi_0^2 (\Delta q)^2 \quad (1.5)$$

as q_c is a maximum growth rate mode. Here τ_0 and ξ_0 are the appropriate time and length scale factors which depend on the actual system.

When ϵ is small, the unstable band of wave vectors, Δq , is small, and we can include the effects of having a band of unstable wave vectors in a modulating envelope of the basic instability $e^{iq_c \cdot x}$. The envelope is known as the ‘amplitude’ A , and the physical variables χ can now be described by

$$\chi(x, y, t) = A(x, y, t) \chi_0 e^{iq_c \cdot x} + c.c., \quad (1.6)$$

where $\chi_0 e^{iq_c \cdot x}$ is the most unstable mode. Since $\Delta q \sim \epsilon^{\frac{1}{2}}$, and $\gamma \sim \epsilon$, A varies on the slow length scale $\frac{\partial}{\partial x} \sim \epsilon^{\frac{1}{2}}$ and the slow time scale $\frac{\partial}{\partial t} \sim \epsilon$. From (1.5), it is clear that the linear part of the ‘amplitude equation’ for A is

$$\tau_0 \frac{\partial A}{\partial t} = \epsilon A + \xi_0^2 \frac{\partial^2 A}{\partial x^2}. \quad (1.7)$$

Since the linear growth usually saturates due to nonlinear effects, there is usually a cubic order saturating term $-g|A|^2A$ on the RHS, and the most basic form of the amplitude equation is

$$\tau_0 \frac{\partial A}{\partial t} = \epsilon A + \xi_0^2 \frac{\partial^2 A}{\partial x^2} - g|A|^2 A. \quad (1.8)$$

Here we have used the simplest case of a one-dimensional system with stationary instability $e^{iq_c x}$. More complicated cases exist; for example, for the traveling-wave instability $e^{i(q_c x - \omega t)}$, the amplitude equation would be

$$\tau_0 \left(\frac{\partial A}{\partial t} + s \frac{\partial A}{\partial x} \right) = \epsilon(1 + ic_0)A + \xi_0^2(1 + ic_1) \frac{\partial^2 A}{\partial x^2} - g(1 + ic_3)|A|^2 A, \quad (1.9)$$

where there is now a group velocity term $\sim s$, and complex coefficients.

A standard technique used in calculating the coefficients in an amplitude equation is the ‘multiple-scales’ approach adopted by Newell and Whitehead [7]. This involves separating the variation of χ into a fast varying part, $e^{iq_c x}$, and a slow varying part incorporated into A . One defines ‘slow’ variables $X = \epsilon^{\frac{1}{2}} x$ and $T = \epsilon t$, and the idea is then that A varies in space on the X length scale and in time on the T time scale. One can then expand in powers of $\epsilon^{\frac{1}{2}}$.

There are also other approaches to understanding the amplitude equation, one of which is the idea of ‘slaved’ and ‘central’ modes favored by [2].

Chapter 2

Motivation and Background

Experiments on rotating Rayleigh-Bénard convection in (necessarily) finite systems have a long history, motivated at least initially by interest in convection in the oceans and the atmosphere [9, 10], where the earth's rotation affects the dynamics. Rossby, in one of the earlier quantitative experiments, observed that there was a significant discrepancy between the observed critical temperature for the onset of convection in water in a rotating cell and that predicted by a linear stability analysis for infinite systems.

These observations were based on heat-transport measurements, where the heat transported across a cell (from lower to upper plate) is compared to that expected for a uniformly heat conducting state. An increase above that expected for the pure conduction state is usually taken as a signature of the onset of convection. Furthermore, the ratio of the heat transported to that expected for a uniformly conducting state is known as the Nusselt number, and is a measure of the convection intensity. Rossby found that the Nusselt number started increasing beyond unity at temperature differences ΔT much smaller than that predicted by the infinite system calculations.

This was especially surprising since for Rayleigh-Bénard convection in nonrotating systems, the convection onsets at higher temperature differences in a finite system than in the ideal infinite system; this is because the boundaries of a finite (real) system suppress the onset of convection, and the increase in ΔT_c is of the order of L^{-2} (L is the system size).

It was Buell and Catton [11] who first suggested that the early onset of convection in finite rotating systems was due to convection states localized near the sidewalls. They numerically solved for nonaxisymmetric modes in small aspect ratio cylindrical cells using the full fluid equations and realistic boundary conditions. Despite searching only for stationary modes, they found asymmetric modes localized near the sidewalls which had critical Rayleigh numbers below that of infinite unbounded systems.

More recent experiments employing the shadowgraph visualization technique by Zhong, Ecke and Steinberg [12] and Ning and Ecke [13] have clarified the nature of the convection states that occur at lower Rayleigh numbers than expected for unbounded systems. In the shadowgraph visualization technique, light is passed through the top plate (usually made of sapphire), passes through the fluid, and is then reflected off the top of the bottom plate (which in the experiments performed by Ning and Ecke is nickel-plated copper). It then passes again through the fluid (and the sapphire top plate) before being imaged and processed. The lateral density gradients due to the temperature differences between the rising fluid, which is warmer, and the falling fluid, which is colder, cause the light which passes through the fluid to be refracted to

different extents, mimicking a series of focussing and defocussing lenses. This leads to dark ‘stripes’ where the light has passed through rising (and hence warm) fluid, and bright ‘stripes’ where the light has passed through falling (and hence cold) fluid. (For a more detailed discussion of this technique, see for example [16].) Convection rolls can thus be ‘seen’ using the shadowgraph technique. (See Fig.(2-1).)

Using this technique, it became experimentally clear that the early onset of convection is indeed due to convection states localized near the sidewalls. In addition, it was observed that the sidewall convection states *precessed* counter to the direction of rotation. A shadowgraph image of such a wall localized convection state is shown in Fig.(2-2).

Furthermore, Goldstein *et al.* [17] performed a theoretical study of convection in rotating cylinders in which they solved for the fluid equations in a full cylindrical geometry for both insulating and conducting sidewalls. They found precessing modes localized near the sidewall of the cylinder at Rayleigh numbers below the critical Rayleigh number for unbounded, infinite systems.

This led us to propose [19] that these sidewall states are not just a feature of small-aspect-ratio systems as might be thought from the earlier studies [11], but a geometry-independent traveling-wave wall state, the existence of which depends only upon the presence of the sidewall, and the addition of the reflection-symmetry-breaking Coriolis force in the equations of motion of the fluid. This approach allows for much simplification in calculating the characteristics of the sidewall state, and

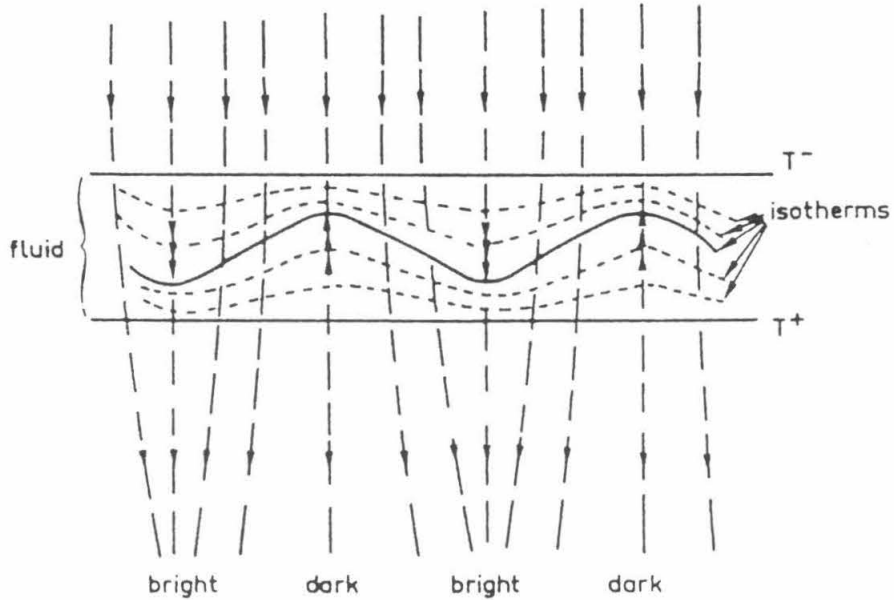


Figure 2-1: Principle of the shadowgraphic method. (Reprint from Fig. 10 of reference [8].)

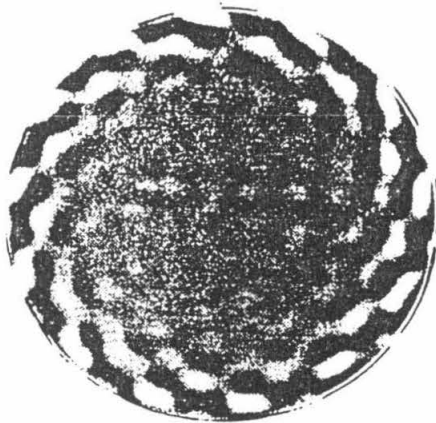


Figure 2-2: Shadowgraph image of a convection pattern below the bulk onset Rayleigh number. (Reprint from Fig. 7 of reference [13].)

also allows one to include the effect of realistic sidewall boundary conditions (*viz* sidewalls that are not necessarily perfectly conducting or insulating) with relative ease. The effects of a finite system can then be calculated as finite-size corrections to this ideal semi-infinite state, just as one treats the bulk convection state in a real, infinite system.

Chapter 3

Traveling-Wave Wall State in Rotating Rayleigh-Bénard Convection

3.1 Linear Stability Analysis

3.1.1 Equations of Motion and Boundary Conditions

We consider convection in a rotating semi-infinite horizontal layer of fluid with one straight infinite sidewall. The angular velocity $\vec{\Omega}_D = \Omega_D \hat{z}$ is constant and in the vertical direction.

The equations of motion are essentially the same as for Rayleigh-Bénard convection in a nonrotating system (1.1-1.3), but there is an additional term in the Navier-Stokes equation due to the Coriolis force. This reflection-symmetry-breaking term proves to make a crucial difference. With this addition, the equations of motion are now

$$\sigma^{-1} \left[\frac{\partial \vec{v}}{\partial t} + (\vec{v} \cdot \vec{\nabla}) \vec{v} \right] = -\sigma^{-1} \vec{\nabla} \left(\frac{p}{\rho_0} \right) + \theta \hat{z} + 2 \Omega \vec{v} \times \hat{z} + \nabla^2 \vec{v} \quad (3.1)$$

$$\frac{\partial \theta}{\partial t} + (\vec{v} \cdot \vec{\nabla}) \theta = R w + \nabla^2 \theta \quad (3.2)$$

$$\vec{\nabla} \cdot \vec{v} = 0, \quad (3.3)$$

where $\Omega = \Omega_D d^2 / \nu$ is the dimensionless angular velocity. The term due to the centrifugal term, $-(\theta \sigma^2 / 2 \tilde{g}) \vec{\nabla} |\vec{\Omega} \times \vec{r}|^2$, which would be on the right-hand-side of (3.1), has been neglected. In practice, this term is negligible compared to the gravitational buoyancy term if $\Omega_D^2 l / g \ll 1$, where l is the radius of the cell.

The coordinate system is taken to be such that the height of the cell is from $z = 0$ to $z = 1$, and the sidewall runs along the x -axis at $y = 0$, with the fluid occupying the positive y half of the xy -plane. The sidewall lies in the negative y half of the plane, and is of arbitrary thickness.

At the bottom, $z = 0$, and at the top, $z = 1$, we will be using the free-slip fluid velocity boundary conditions and the physical thermal boundary condition:

$$w = \frac{\partial u}{\partial z} = \frac{\partial v}{\partial z} = 0, \quad (3.4)$$

$$\theta = 0. \quad (3.5)$$

The boundary conditions at the sidewall, $y = 0$, are the physical no-slip fluid velocity boundary conditions,

$$u = v = w = 0, \quad (3.6)$$

and the condition for the continuity of heat,

$$\frac{\partial \theta}{\partial y} - \mu \theta = 0, \quad (3.7)$$

where μ depends not only on the thermal properties of the sidewall and the fluid, but also upon the nature of the solution in the fluid.

For the linear stability problem in rotating convection, there are reasons to believe that the solution found with free-slip boundary conditions to be quite accurate, and even exact in the large-rotation-rate limit. In their paper [17], Goldstein *et al.* showed that in finite cylindrical cells, at least for large rotation rates, the critical Rayleigh number, precession frequency and azimuthal mode number of the ‘fast mode’, which corresponds to the traveling-wave wall state, do not depend strongly upon whether one uses the free-slip or the no-slip boundary conditions at the top and bottom plates. Also, Clune and Knobloch [20] showed that for the bulk state, the no-slip and free-slip solutions to the linear stability problem become identical as $\Omega \rightarrow \infty$. The reason for this weak difference between free-slip and no-slip boundary conditions, particularly at large rotation rates, is the existence of thin ($\sim (\nu/\Omega_D)^{\frac{1}{2}}$) Ekman boundary layers in the case of no-slip boundary conditions. Outside the thin boundary layers, the dominant mode may be similar to the mode for free-slip boundary conditions, and thus the linear onset solution will have similar critical parameters. This, however, probably does not hold for nonlinear calculations, which involve coupling the dominant mode to other modes.

3.1.2 Method of Solution

Traveling-wave wall states in this coordinate system should have a basic space and time dependence that $\sim \exp[i(q_x x - \omega t)]$. Thus to find the lowest Rayleigh number critical onset wall state, we seek solutions of linearized versions of equations (3.1) - (3.3) of the form, (the components of χ are the physical variables u , v , w and θ)

$$\chi(x, y, z, t) = \chi_0(y, z) e^{i(q_x x - \omega t)} + c.c. \quad (3.8)$$

for different q_x , which also satisfy the boundary conditions (3.4) - (3.7), as well as the condition that χ not diverge as $y \rightarrow +\infty$. The solution with the lowest onset Rayleigh number is then the critical onset wall state, and we have thus found R_c , ω_c and q_{xc} , the critical Rayleigh number, precession frequency, and wave number of the traveling-wave wall state.

Writing the space and time dependence of the physical variables as

$$\chi(x, y, z, t) = \chi_0(y, z) e^{\Gamma t} e^{iq_x x} + c.c.; \quad (3.9)$$

where $\Gamma = \gamma - i\omega$ is complex, we can use the method of separation of variables to find a solution. The choice of free-slip boundary conditions at $z = 0$ and $z = 1$ now allows one to separate the y and z spatial dependences, and write the z -dependence of u and v as $\cos(n\pi z)$, and that of w and θ as $\sin(n\pi z)$, where n is an integer, so that the boundary conditions at $z = 0$ and $z = 1$ are automatically satisfied. It is

‘intuitively’ clear from dissipation considerations, and can also be shown, that $n = 1$ will be the solution with the lowest onset Rayleigh number, and from now on we will just take n to be 1.

It now remains to find the y -dependence of χ_0 such that the boundary conditions at $y = 0$, (3.6) - (3.7), and the condition that χ_0 not diverge as $y \rightarrow +\infty$ are satisfied. The modes we sum over to satisfy the boundary conditions are of the form $\exp(iq_y y)$, with $Im(q_y) \geq 0$, *i.e.*, we seek solutions of the form

$$\chi(x, y, z, t) = e^{\Gamma t} e^{iq_x x} \sum_{j=1} e^{iq_y j y} \begin{pmatrix} U_{0j} \cos \pi z \\ V_{0j} \cos \pi z \\ W_{0j} \sin \pi z \\ \Theta_{0j} \sin \pi z \end{pmatrix} + c.c.. \quad (3.10)$$

Equations (3.1) - (3.2) are four second-order differential equations in space. Thus upon linearizing and combining them, and using the incompressibility condition (3.3), one gets a fourth-order dispersion relation in $q_x^2 + q_y^2$ of the form,

$$(Q_1^2)^4 + A_3(Q_1^2)^3 + A_2(Q_1^2)^2 + A_1(Q_1^2) + A_0 = 0, \quad (3.11)$$

where

$$Q_1^2 = q_x^2 + q_y^2 + \pi^2 \quad (3.12)$$

and

$$\begin{aligned}
A_3 &= \Gamma(1 + 2\sigma^{-1}), \\
A_2 &= \sigma^{-1}\Gamma^2(2 + \sigma^{-1}) - R, \\
A_1 &= \sigma^{-2}\Gamma^3 - R\sigma^{-1}\Gamma + (R + (2\Omega)^2)\pi^2, \\
A_0 &= \Gamma\pi^2(\sigma^{-1}R + (2\Omega)^2).
\end{aligned}$$

Thus for each fixed q_x , four (in general, complex) values of q_y^2 would give modes satisfying the equations of motion, but of these pairs of q_y , only the one that allows $\chi \rightarrow 0$ when $y \rightarrow +\infty$ is included in the sum. Thus the index j in (3.10) runs from 1 to 4, summing over 4 complex q_y 's with $Im(q_y) \geq 0$.

For a solution of this form, the value of μ in (3.7) is (see Appendix A)

$$\mu = K_w k_w \tanh(k_w l_w), \quad (3.13)$$

where K_w is the ratio of the thermal conductivity of the sidewall to that of the fluid, l_w is the width of the sidewall, and with κ_w the thermal diffusivity of the sidewall,

$$k_w^2 = (q_x^2 + \pi^2 + \kappa_w^{-1}\Gamma). \quad (3.14)$$

One can also use the linearized versions of (3.1) - (3.2) to write the variables U_{0j} , V_{0j} and W_{0j} in terms of Θ_{0j} . Thus the four boundary conditions at $y = 0$ can be

written in the form of a *complex* boundary matrix condition on the Θ_{0j} :

$$\begin{pmatrix} a_1 & a_2 & a_3 & a_4 \\ b_1 & b_2 & b_3 & b_4 \\ c_1 & c_2 & c_3 & c_4 \\ d_1 & d_2 & d_3 & d_4 \end{pmatrix} \begin{pmatrix} \Theta_{01} \\ \Theta_{02} \\ \Theta_{03} \\ \Theta_{04} \end{pmatrix} = 0 \quad (3.15)$$

where

$$\begin{aligned} \text{with} \quad Q_{1j}^2 &= q_x^2 + q_{yj}^2 + \pi^2, \\ a_j &= \frac{\Gamma + Q_{1j}^2}{Q_{1j}^2 - \pi^2} \left(q_x + \frac{2\Omega q_{yj}}{\sigma^{-1}\Gamma + Q_{1j}^2} \right), \\ b_j &= \frac{\Gamma + Q_{1j}^2}{Q_{1j}^2 - \pi^2} \left(q_{yj} - \frac{2\Omega q_x}{\sigma^{-1}\Gamma + Q_{1j}^2} \right), \\ c_j &= \Gamma + Q_{1j}^2, \\ d_j &= i q_{yj} - \mu. \end{aligned}$$

For a non-trivial solution to exist, the determinant of the matrix in (3.15) must be zero. Since the determinant of this matrix is complex, and we are seeking for a critical onset traveling-wave state of the form $\exp[i(q_x x - \omega t)]$ (*i.e.*, $\Gamma = -i\omega$), for each fixed q_x , we can find, numerically using a nonlinear root-finding routine (we used the PORT library routine DZONE), R and ω , such that the (complex) determinant in (3.15) is zero. One can then also solve for the eigenvectors of the matrix to find the form of the onset solution.

This gives the onset Rayleigh number and frequency for a *given* q_x . Minimizing the onset Rayleigh number with respect to q_x , we find the critical Rayleigh number R_c , the critical frequency ω_c , and the critical wave number q_{xc} .

3.1.3 Results

In this section, we will present examples of results from the linear instability calculations and compare when possible with data from experiments. Specifically, we will show results for Prandtl number σ equal to 6.4 (which is that of water at around room temperature where experiments are mostly done), and for three types of sidewall thermal boundary conditions – the ideal limits of perfectly insulating ($\mu = 0$) and perfectly conducting ($\mu \rightarrow \infty$) sidewalls, and sidewall boundary conditions corresponding to the experiments of Ning and Ecke [13], for which we will also be able to compare some of our results with the experimental data.

In Fig.(3-1, 3-2, 3-3), the critical Rayleigh numbers R_c , frequencies ω_c , and wave vectors q_{xc} for the different sidewall thermal boundary conditions are plotted as a function of Ω , the dimensionless rotation rate. The critical Rayleigh number for the bulk state is also plotted. It can be seen that though the critical Rayleigh number for the wall state is generally lower than that for the bulk state at the same rotation rate, the reverse is true when the rotation rate is smaller than some rotation rate Ω_c . More interestingly, the critical solution for the wall state ‘*disappears*’ beyond some small rotation rate. At this rotation rate, the critical frequency goes to zero linearly,

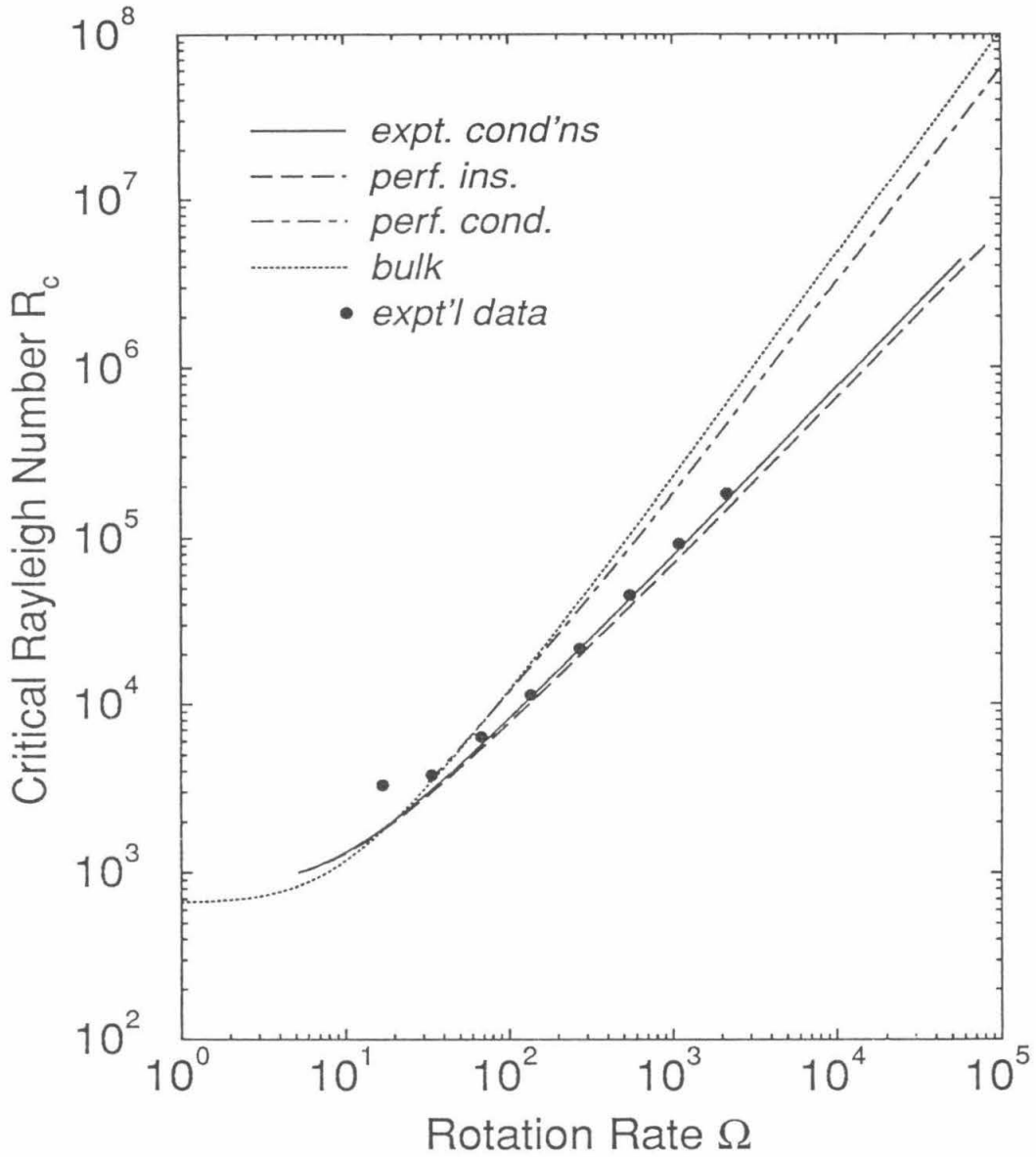


Figure 3-1: Critical Rayleigh number as a function of the rotation rate Ω for different sidewall thermal boundary conditions for Prandtl number $\sigma = 6.4$.

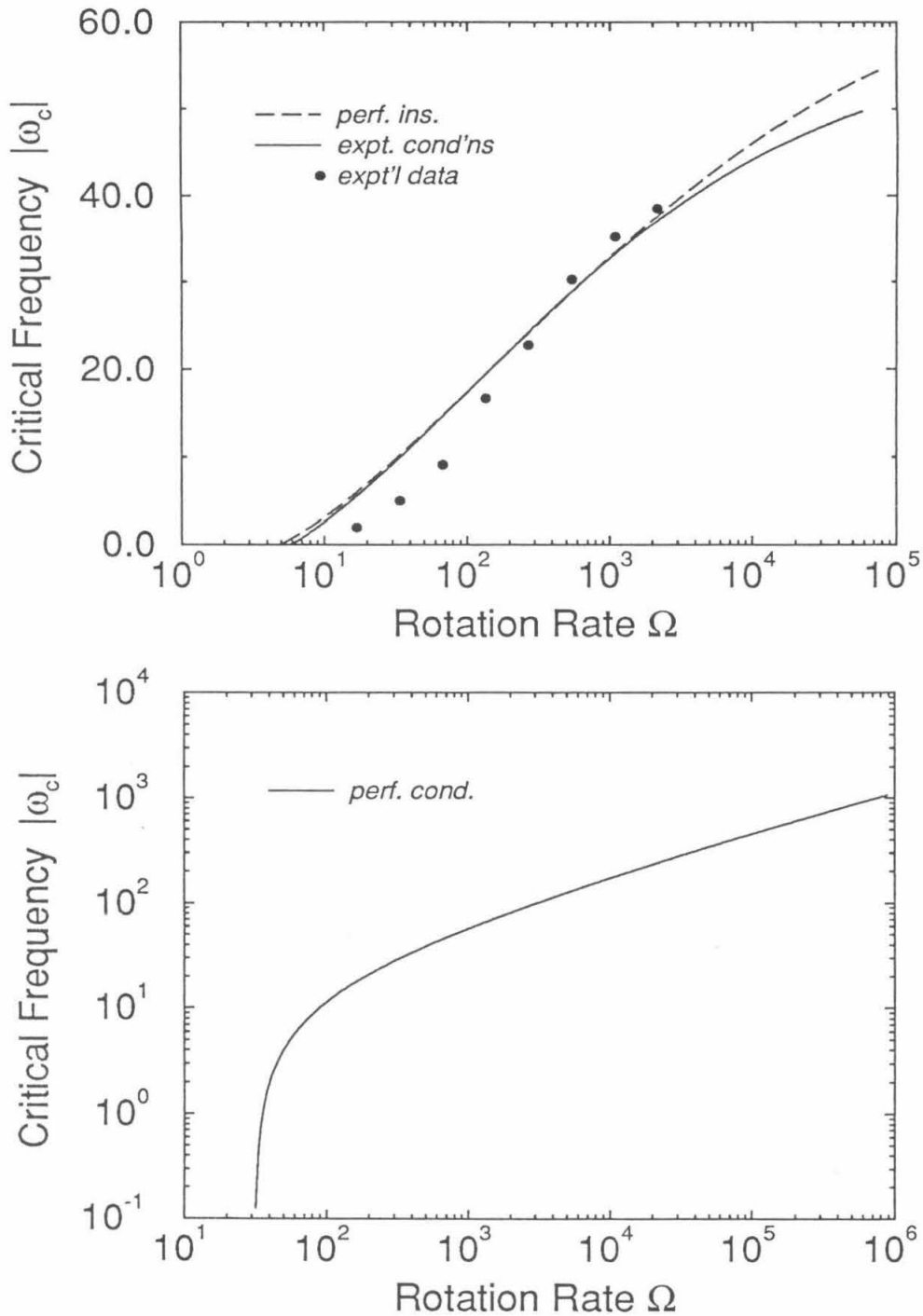


Figure 3-2: Critical frequency ω_c for the same conditions as in Fig.(3-1).

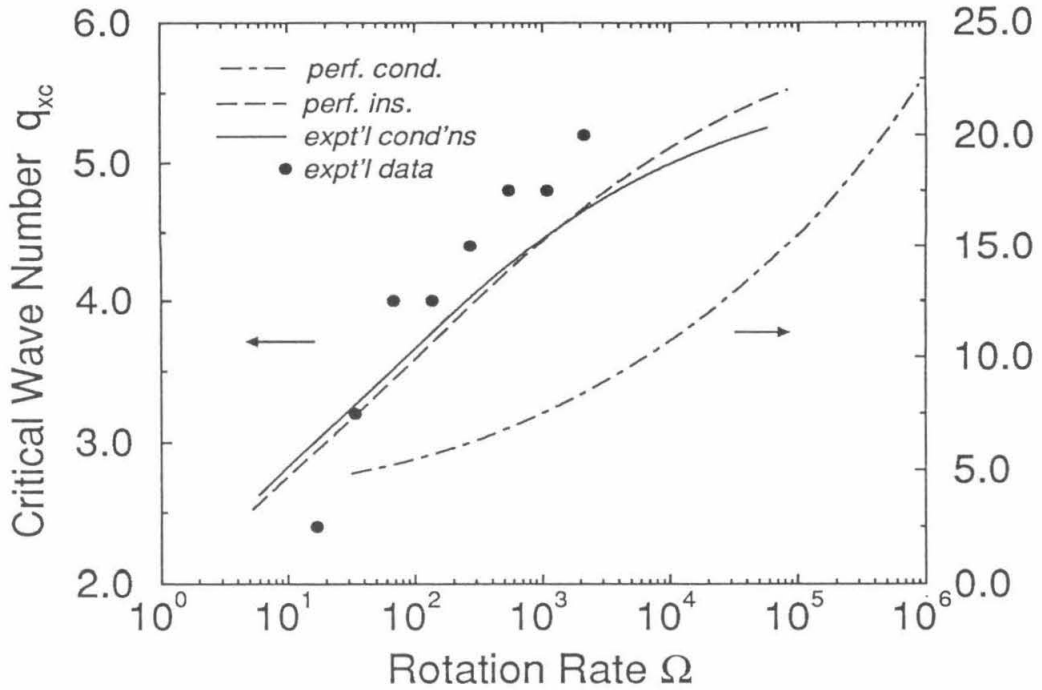


Figure 3-3: Critical wave vector q_{xc} for the same conditions as in Fig.(3-1).

as does the spatial decay rate $Im q_y$ for one of the q_y , while $Re q_y$ for this same q_y goes to a nonzero constant.

The situation becomes clearer if we fix the rotation rate, and find the critical onset solution as a function of the wave vector, q_x . In Fig.(3-4) we show this for $\Omega = 10$. The solution 'disappears' beyond some wave vector q_x^* , at which wave number the frequency ω goes to zero linearly, as does the spatial decay rate $Im q_y$ for one of the q_y . This is shown in Fig.(3-5, 3-6), where the other q_y 's are also plotted.

The nature of this point at which the traveling-wave wall state solution disappears will be further explored in Section 4 using the modified Swift-Hohenberg model which also shows these apparently generic features.

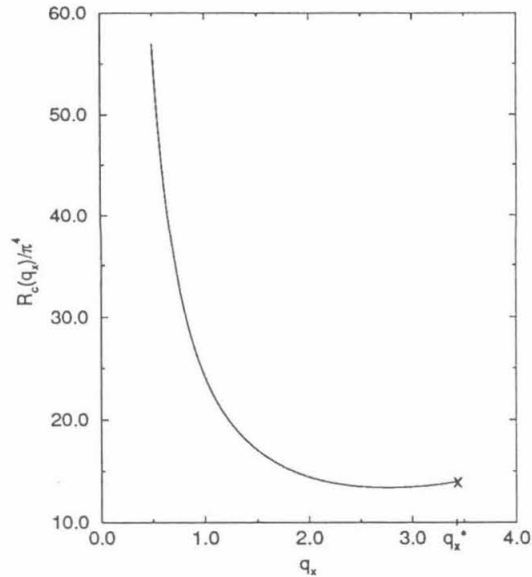


Figure 3-4: Critical Rayleigh number as a function of the wave number q_x for the fixed rotation rate $\Omega = 10$. The Prandtl number $\sigma = 6.4$, and the sidewall is perfectly insulating ($\mu = 0$). The point at which the wall state solution ‘disappears’ is indicated by a cross.

That the traveling-wave wall state should ‘disappear’ at some finite, non-zero value of the rotation rate Ω at which point its frequency also goes to zero linearly is very intriguing. This is additionally an unexpected finding as arguments based on bifurcation theory [18, 17] (in a finite system) predict that the frequency of the traveling-wave will go to zero linearly with the rotation rate, *i.e.*, $\omega \sim \Omega$. How to connect our finding for the semi-infinite system, and the bifurcation argument for a finite system poses an interesting question.

In Fig.(3-1, 3-2, 3-3), we have also included the experimental data from Ning and Ecke [13]. Their experiments were performed in an aspect-ratio-2.5 cylindrical cell in water at a mean temperature of about 23.5°C , for which the Prandtl number σ

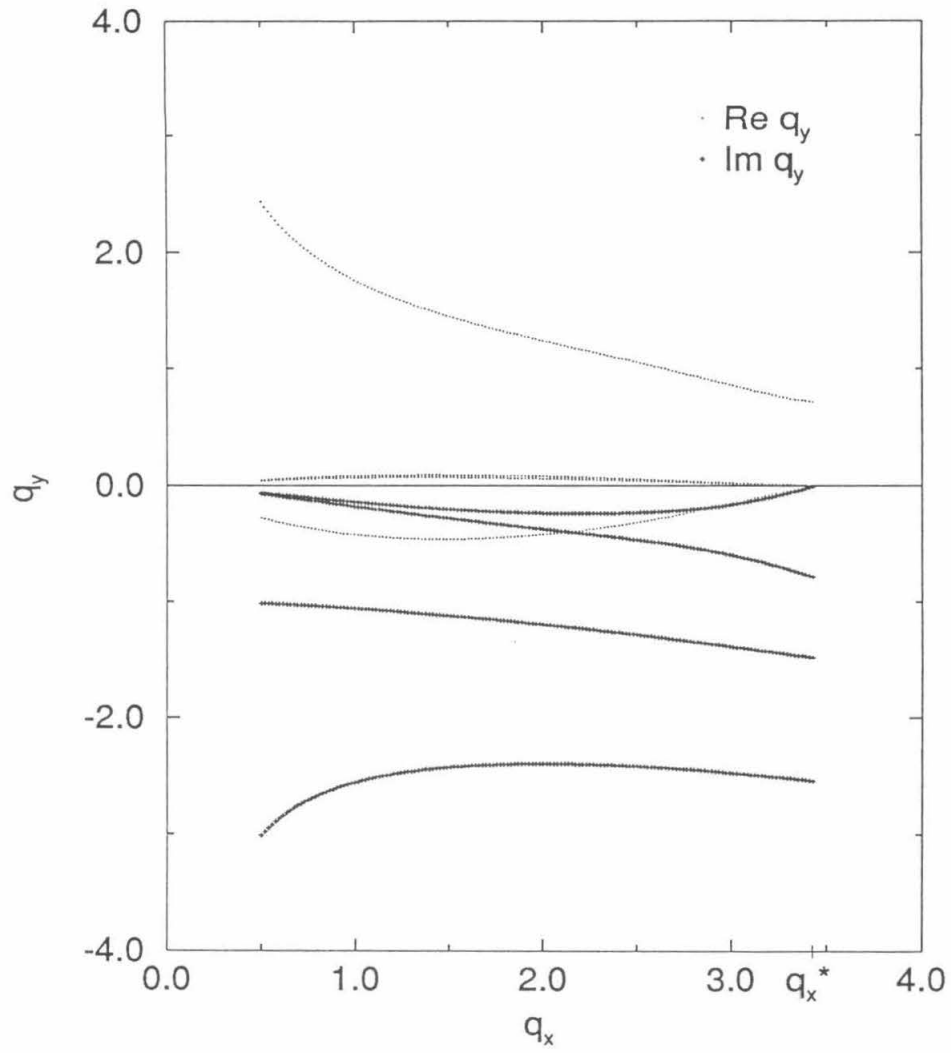


Figure 3-5: Normal wave vectors q_y for the same conditions as in Fig.(3-4).

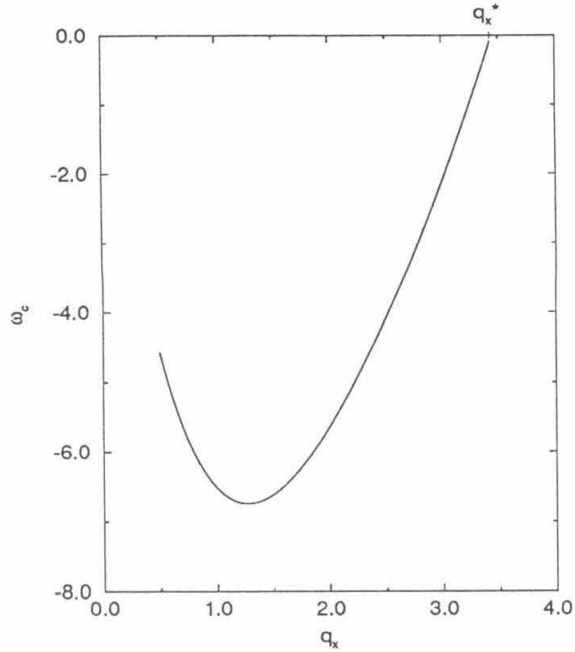


Figure 3-6: Critical frequency for the same conditions as in Fig.(3-4).

is about 6.4. The sidewall in their experiments was made of Plexiglas, and of width

$$l_w = \frac{0.31\text{cm}}{2.00\text{cm}} = 0.15 \text{ measured in units of the cell height.}$$

References [14] and [15] give the relative thermal conductivity of the sidewall to the fluid (water) as $K_w = \frac{1.5\text{mW.cm}^{-1}.\text{K}^{-1}}{6.0\text{mW.cm}^{-1}.\text{K}^{-1}} = 0.25$, and the relative thermal diffusivity as $\kappa_w \approx \frac{0.0012\text{cm}^2.\text{s}^{-1}}{0.0015\text{cm}^2.\text{s}^{-1}} = 1$. The calculation for which the results are shown in Fig.(3-1, 3-2, 3-3), was thus done for $l_w = 0.15$, $K_w = 0.25$, $\kappa_w = 1$, and $\sigma = 6.4$.

Considering that the calculations were done for free-slip boundary conditions, while the experimental boundary conditions were naturally rigid, the critical Rayleigh numbers show remarkably good agreement except for small rotation rates where the bulk mode begins to onset before the wall mode. At these small rotation rates, the discrepancy between calculation and experiment is also relatively larger for the

frequency and wave vector.

In a finite system, even the bulk mode would be expected to gain a small rotation rate (probably going as L^{-1} , where L is the size of the system). Thus how the wall and bulk modes merge in a finite system poses an interesting problem which we will study using the modified Swift-Hohenberg model in Section 4.

3.1.4 Asymptotic Results

In the case of the bulk convection state in an infinite unbounded system, Chandrasekhar [4] showed that, when the rotation rate is large, the asymptotic behavior of R_c and q_c for both free-slip and no-slip top and bottom boundary conditions is $R_c \sim \Omega^{\frac{4}{3}}$ and $q_c \sim \Omega^{\frac{1}{3}}$.

The traveling-wave wall state has a different asymptotic limit at large rotation rates, and this limit also depends upon the thermal boundary condition imposed at the sidewall. In the case of insulating, or nonperfectly conducting, sidewalls, we find the asymptotics to be $R_c \sim \Omega$, $q_{xc} \rightarrow \text{constant}$ and $\omega_c \rightarrow \text{constant}$, in the limit $\Omega \rightarrow \infty$. In the case of perfectly conducting sidewalls, the asymptotic behavior is $R_c \sim \Omega^{\frac{4}{3}}$, $q_{xc} \sim \Omega^{\frac{1}{3}}$, and $\omega_c \sim \Omega^{\frac{1}{3}}$, as $\Omega \rightarrow \infty$. These asymptotic limits can initially be ‘guessed’ at by considering the numerical results at large rotation rates, and by balancing the terms in the dispersion relation.

Using these asymptotic limits to scale the solutions, one can solve for the exact asymptotic solutions at large Ω . The case of insulating, or nonperfectly conducting,

sidewalls was solved for in both [21] and [19], and the case of perfectly conducting sidewalls was solved for in [21].

In the case of nonperfectly conducting sidewalls, it is observed in the numerics that in the limit $\Omega \rightarrow \infty$,

$$R_c \sim O(\Omega),$$

$$\omega_c \rightarrow \text{constant},$$

$$\text{and } Q_{11}^2 = q_x^2 + q_{y1}^2 + \pi^2 \sim O(\Omega^{-1}) + i(\omega + O(\Omega^{-1})),$$

$$Q_{12}^2 \sim O(\Omega^{\frac{2}{3}}) + i \cdot \text{constant},$$

$$Q_{13}^2 \sim O(\Omega^{\frac{2}{3}}) + i \cdot O(\Omega^{\frac{2}{3}}),$$

$$Q_{14}^2 \sim O(\Omega^{\frac{2}{3}}) + i \cdot O(\Omega^{\frac{2}{3}}),$$

$$q_{y1} \rightarrow \text{constant} + i \cdot \text{constant},$$

$$q_{y2} \sim O(\Omega^{-\frac{1}{3}}) + i \cdot O(\Omega^{\frac{1}{3}}),$$

$$q_{y3} \sim O(\Omega^{\frac{1}{3}}) + i \cdot O(\Omega^{\frac{1}{3}}),$$

$$q_{y4} \sim O(\Omega^{\frac{1}{3}}) + i \cdot O(\Omega^{\frac{1}{3}}),$$

where, furthermore, $q_{y4} \rightarrow -q_{y3}^*$, and consequently, $Q_{14}^2 \rightarrow Q_{13}^{2*}$.

Using these scalings, one can now solve for the exact asymptotic limit. The onset

Rayleigh number and frequency at wave vector q_x are found to be given by

$$(\pi + iq_x)(iq_{y1} - \mu) + i\bar{R}q_x = 0, \quad (3.16)$$

with $\mu(q_x, \omega)$ given by (3.13) and $\bar{R} = R/2\pi\Omega$, and where $q_{y1} = (i\omega - q_x^2 - \pi^2)^{\frac{1}{2}}$ is the complex wave vector component giving the decay normal to the sidewall. (Note the other wave vectors giving the decay normal to the sidewall, $q_{yj}, j = 2, 3, 4$, have decay lengths scaling as $\Omega^{-\frac{1}{3}} \rightarrow 0$.)

For the special case of perfectly insulating sidewalls, $\mu = 0$, one can solve (3.16) analytically to find

$$\begin{aligned} q_{xc} &\rightarrow \sqrt{2 + \sqrt{3}}\pi = 6.069, \\ R_c &\rightarrow 2\pi^2\sqrt{6\sqrt{3}}\Omega = 63.63\Omega, \\ \text{and } \omega_c &\rightarrow -2\pi^2\sqrt{6 + 3\sqrt{3}} = -66.05. \end{aligned}$$

For the parameters and boundary conditions corresponding to the experimental boundary conditions of [13], (3.16) can be solved numerically to give the asymptotic solution of $R_c \rightarrow 74.40\Omega$, $q_{xc} \rightarrow 5.545$ and $\omega_c \rightarrow -57.68$. Fits to the numerical results up to $\Omega = 50\,000$, assuming corrections to the asymptotic limit go as a polynomial in $\Omega^{-\frac{1}{3}}$ give good agreement with these values. These fits and the asymptotic limits are shown in Fig.(3-7).

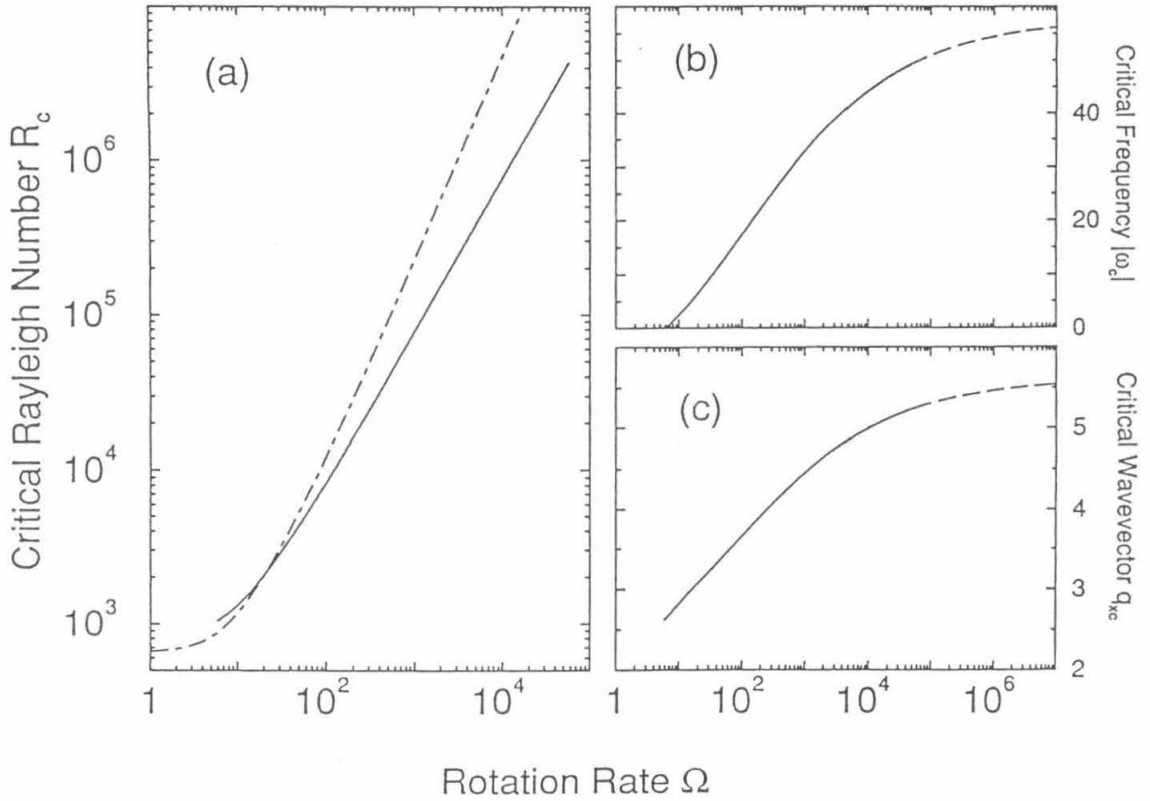


Figure 3-7: Critical Rayleigh number, frequency and wave number and their asymptotic limits (the dashed lines) for the experimental sidewall thermal boundary conditions.

3.2 Amplitude Equation for the Traveling-Wave Wall State

Near onset, the traveling-wave wall state may experience slow modulations in both space and time (along the wall), and the dynamics may be calculated by expanding in a small parameter $\epsilon = (R - R_c)/R_c$. The amplitude A is the complex envelope of the basic traveling-wave, $\exp[i(q_{xc} - \omega_c t)]$, *i.e.*, the physical quantities are

$$\chi(x, y, z, t) = A(x, t) e^{i(q_{xc}x - \omega_c t)} \chi_0(y, z) + c.c. + h.o.t.,$$

where $A \sim \epsilon^{\frac{1}{2}}$ and the higher order terms (h.o.t.) are $O(\epsilon)$. The amplitude equation is one-dimensional in the sense that the dynamics of the amplitude depend only upon the spatial variations parallel to the sidewall, and can be written as

$$\tau_0 \left(\frac{\partial A}{\partial t} + s \frac{\partial A}{\partial x} \right) = \epsilon(1 + ic_0)A + \xi_0^2(1 + ic_1) \frac{\partial^2 A}{\partial x^2} - g(1 + ic_3)|A|^2 A \quad (3.17)$$

to lowest nonlinear order. Here A is the complex envelope of the basic traveling-wave, and the parameters s , τ_0 , ξ_0 , g , c_0 , c_1 and c_3 are (real-valued) parameters that can be calculated and measured. s is easily seen to be the group velocity, and τ_0 and ξ_0 are the time and length scales of the modulation respectively. The cubic term turns out to have negative real part (g is positive), thus the solution A saturates when $|A| \sim \epsilon^{\frac{1}{2}}$, and the bifurcation is forward.

The parameters in the linear part of the amplitude equation can be calculated by finding (numerically) the complex growth rate $\Gamma = \gamma - i(\omega_c + \Delta\omega)$ as a function of $\epsilon = (R - R_c)/R_c$ and the wave number difference $k = q_x - q_{xc}$ for small ϵ and small k , such that, as in calculating the onset parameters, the dispersion relation and the boundary conditions are satisfied for the solutions found for the linearized equations of motion. Since the physical variables $\sim A(x, t) \exp[i(q_{xc}x - \omega_c t)]$, from the simple case $A(x, t) \sim \exp[(\gamma - i\Delta\omega)t] \exp(ikx)$, we find that

$$\tau_0^{-1} = \left. \frac{\partial \gamma}{\partial \epsilon} \right|_{\epsilon=k=0} \quad (3.18)$$

$$s = \left. \frac{\partial(\Delta\omega)}{\partial k} \right|_{\epsilon=k=0} \quad (3.19)$$

$$\xi_0^2 = -\frac{1}{2} \tau_0 \left. \frac{\partial^2 \gamma}{\partial k^2} \right|_{\epsilon=k=0} \quad (3.20)$$

$$c_0 = -\tau_0 \left. \frac{\partial(\Delta\omega)}{\partial \epsilon} \right|_{\epsilon=k=0} \quad (3.21)$$

$$\text{and } c_1 = \frac{1}{2} \tau_0 \xi_0^{-2} \left. \frac{\partial^2(\Delta\omega)}{\partial k^2} \right|_{\epsilon=k=0} \quad (3.22)$$

In Fig.(3-8, 3-9, 3-10, 3-11, 3-12) we show these parameters of the amplitude equation as a function of the rotation rate, for Prandtl number σ equal to 6.4, and the three types of thermal boundary conditions of before. It is worth pointing out that the group velocity s , which is positive, is in the opposite direction to the phase velocity ω_c/q_{xc} , which is negative. In Fig.(3-8, 3-9, 3-10, 3-11, 3-12), we also include one set of experimental measurements of these parameters at rotation rate $\Omega = 544$ from [13] for comparison. When comparing theory and experiment, one should bear

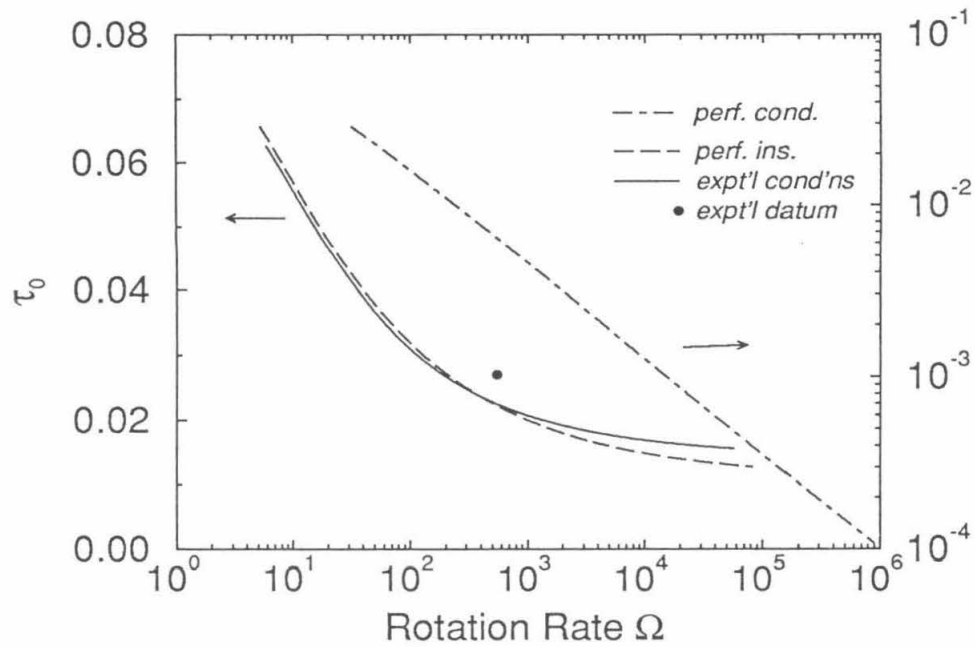


Figure 3-8: Amplitude equation time scale parameter τ_0 for the same conditions as in Fig.(3-1).

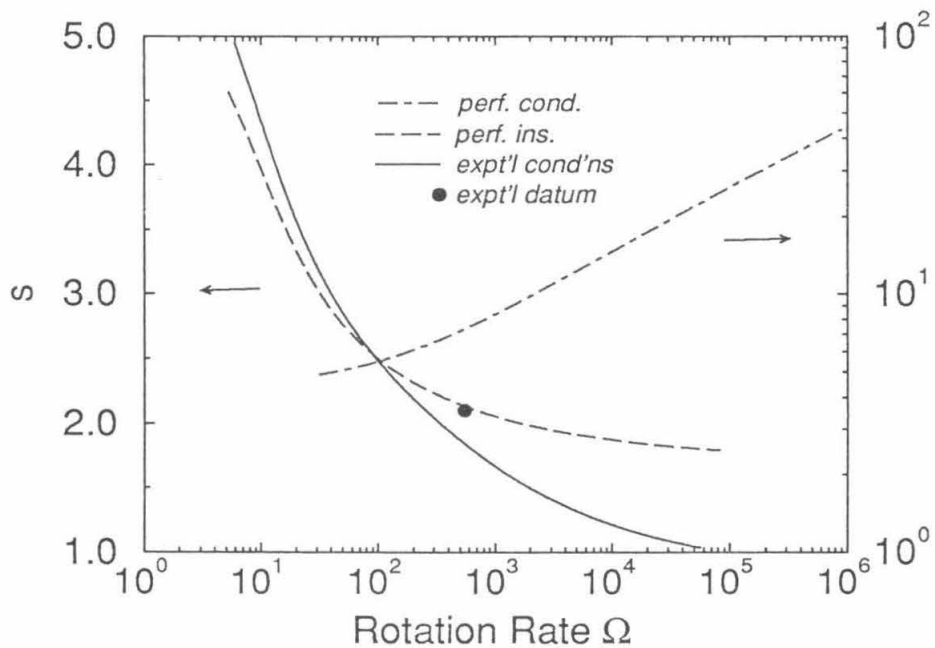


Figure 3-9: Amplitude equation group velocity s for the same conditions as in Fig.(3-1).

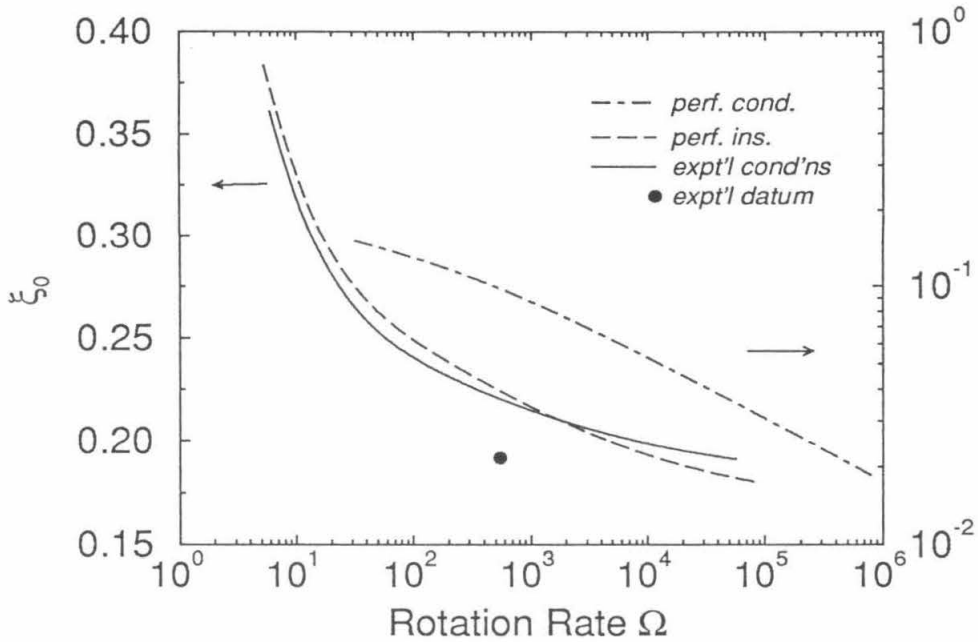


Figure 3-10: Amplitude equation length scale parameter ξ_0 for the same conditions as in Fig.(3-1).

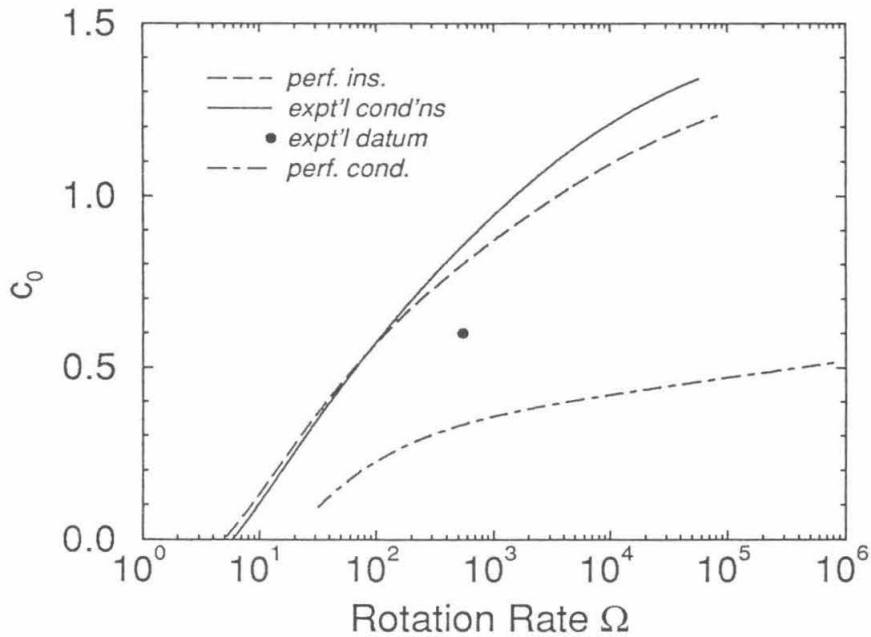


Figure 3-11: Amplitude equation parameter c_0 for the same conditions as in Fig.(3-1).

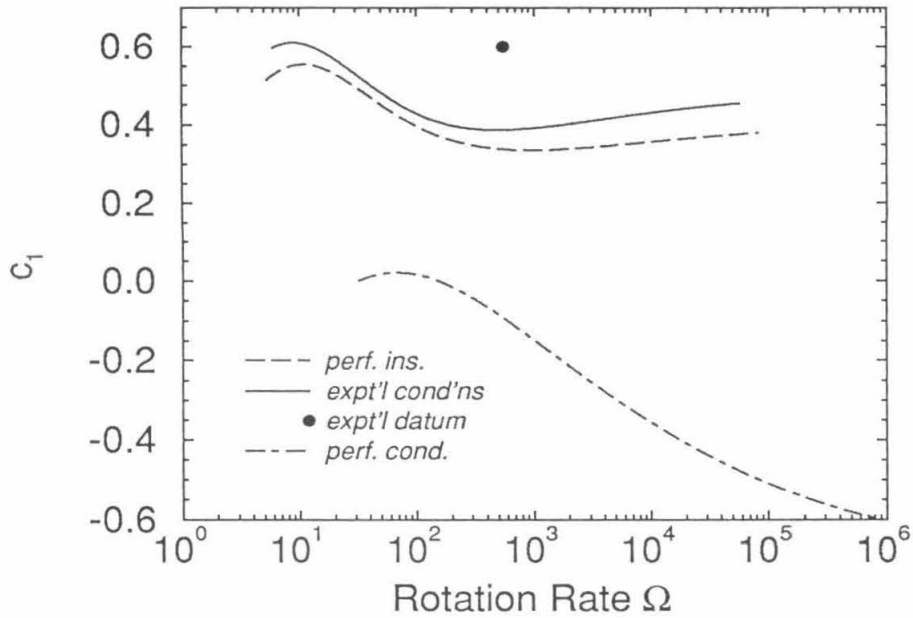


Figure 3-12: Amplitude equation parameter c_1 for the same conditions as in Fig.(3-1).

in mind the fact that the experiments were performed in a finite system, and that the measurements of c_0 and c_1 are relatively indirect [13]. Furthermore, the calculations were done for free-slip top-and-bottom boundary conditions, whereas the experiments were naturally done under rigid boundary conditions.

Chapter 4

Swift-Hohenberg Models

The Swift-Hohenberg model is a relatively simple ‘microscopic’ model that exhibits the same basic linear instabilities which lead to pattern formation as Rayleigh-Bénard convection systems (as well as other pattern-forming systems falling in the same class). For this reason, it has been used extensively to study pattern formation as it is generally much more tractable analytically and much easier to simulate numerically. The original Swift-Hohenberg model [23] is a two-dimensional system (here taken to be the $x - y$ plane) and takes the form

$$\frac{\partial \psi}{\partial t} = \epsilon \psi - (\nabla^2 + q_0^2)^2 \psi - \psi^3, \quad (4.1)$$

where q_0 is generally taken to be $q_0 = 1$.

Equation (4.1) exhibits a basic linear instability at the wave number q_0 when $\epsilon > 0$. Expanding about $\vec{q} = q_0 \hat{x}$, for example, we observe that the linear growth rate

Γ for wave number $\vec{q} = (q_0 + \Delta q_x) \cdot \hat{x} + \Delta q_y \cdot \hat{y}$ is

$$\Gamma(q) = \epsilon - (2q_0)^2 (\Delta q_x + \frac{1}{2q_0} (\Delta q_y)^2)^2 \quad (4.2)$$

which is of the same form as that for the basic linear instability in Rayleigh-Bénard convection. The cubic nonlinear term, here ψ^3 , leads to nonlinear saturation when $\psi \sim \epsilon^{\frac{1}{2}}$, and respects the symmetry $\psi \rightarrow -\psi$.

The nonlinear term is often modified to generate different patterns at the nonlinear level, but the linear terms are kept the same as they contain the ‘mechanism’ for the basic linearly unstable pattern at the wave number $q = q_0$.

In this section, the original Swift-Hohenberg model will be modified in two ways to mimic the effects of rotation in a real Rayleigh-Bénard convection system. We will show that the traveling-wave wall state seen in rotating Rayleigh-Bénard convection systems can be induced in a Swift-Hohenberg model by the addition of reflection-symmetry-breaking boundary conditions. This state, as mentioned previously, also disappears. We will therefore use this system to study in detail the wall state – bulk state transition region. A numerical study of this region will provide the basis for an understanding of this transition based on a phenomenological amplitude equation description of the transition region.

We will also discuss the other, historically better known, dynamical aspect of rotating Rayleigh-Bénard convection – the Küppers-Lortz instability and its Swift-Hohenberg model equivalent.

4.1 Swift-Hohenberg Model with Reflection-Symmetry-Breaking Boundary Conditions

In Section 3, we saw that the traveling-wave wall state in rotating Rayleigh-Bénard convection is due to a linear instability of the form $\exp(i(qx - \omega t))$ decaying away from the wall, and that the physical ingredients for the existence of this state are the existence of a wall allowing complex wave vectors in the direction normal to the wall, and the loss of the reflection symmetry $x \rightarrow -x$ along the wall.

We shall show that the traveling-wave wall states can also be seen in the original Swift-Hohenberg model (4.1), but with the addition of a semi-infinite straight wall at which boundary conditions breaking the reflection symmetry are imposed.

4.1.1 Reflection-Symmetry-Breaking Boundary Conditions

The boundary conditions imposed at the sidewall should

- be homogeneous, or linear, in ψ ,
- respect rotation symmetry,
- break reflection symmetry,

and include the orientation of the wall. One of the simplest sets of boundary conditions, which is non-trivial, and fulfills the above expectations, is

$$\hat{n} \cdot \nabla \psi = \lambda \psi, \tag{4.3}$$

$$\mu \hat{z} \cdot (\hat{n} \times \nabla)(\nabla^2 + q_0^2)\psi = \psi, \quad (4.4)$$

where \hat{n} is the unit normal vector pointing inwards from the boundary, and $\hat{z} = \hat{x} \times \hat{y}$ is the unit vector normal to the plane of the system (the $x - y$ plane). In (4.4), q_0 is taken to be the maximally unstable wave number, $q_0 = 1$, in the bulk, so that, in some sense, (4.4) represents the breaking of reflection symmetry with respect to the orientation of the ‘rolls’ to the wall. λ and μ are adjustable parameters, where μ is the parameter which represents the strength of the reflection-symmetry-breaking. For a wall state to exist, we will find it necessary for λ to be negative, representing a decay in the amplitude of the state away from the wall.

4.1.2 Linear Instability Analysis for the Traveling-Wave Wall State

The linear instability analysis for the wall state in the Swift-Hohenberg model with reflection-symmetry-breaking boundary conditions follows the same principles as the analysis in the case of Rayleigh-Bénard convection in a rotating system, but is much simpler.

In the Swift-Hohenberg model, the dispersion relation is second-order in $Q^2 = q_x^2 + q_y^2$, and is

$$\Gamma = \gamma - i\omega = \epsilon - (q_x^2 + q_y^2 - q_0^2)^2. \quad (4.5)$$

Thus the traveling-wave wall state can be written in the form

$$\psi(x, y, t) = e^{i(q_x x - \omega t)} \sum_{j=1,2} \tilde{\psi}_j e^{i q_{yj} y}, \quad (4.6)$$

where again, of each pair of q_y 's satisfying the dispersion relation with equal value of q_y^2 , only the one that has $Im(q_y) \geq 0$ is included. The boundary conditions (4.3 - 4.4) at $y = 0$ can again be written in the form of a complex boundary condition matrix of the form

$$\begin{pmatrix} a_1 & a_2 \\ b_1 & b_2 \end{pmatrix} \begin{pmatrix} \tilde{\psi}_1 \\ \tilde{\psi}_2 \end{pmatrix} = 0, \quad (4.7)$$

where

$$a_j = i q_{yj} - \lambda, \quad (4.8)$$

$$b_j = \mu i q_x (q_0^2 - q_x^2 - q_{yj}^2) + 1. \quad (4.9)$$

Thus for given q_x , we can find numerically, ϵ and ω , such that the characteristic equation of this complex matrix condition is satisfied. The eigenvectors of this matrix then give the form of the onset solution. Minimizing the onset ϵ with respect to q_x , we find the critical ϵ , ϵ_c , the critical frequency ω_c , and the critical wave number q_{xc} , as well as the form of the critical onset solution.

Figures (4-1,4-2,4-3) show an example of the critical ϵ , frequency and wave number as a function of μ , the symmetry-breaking parameter, for fixed λ . As presaged in Sec-

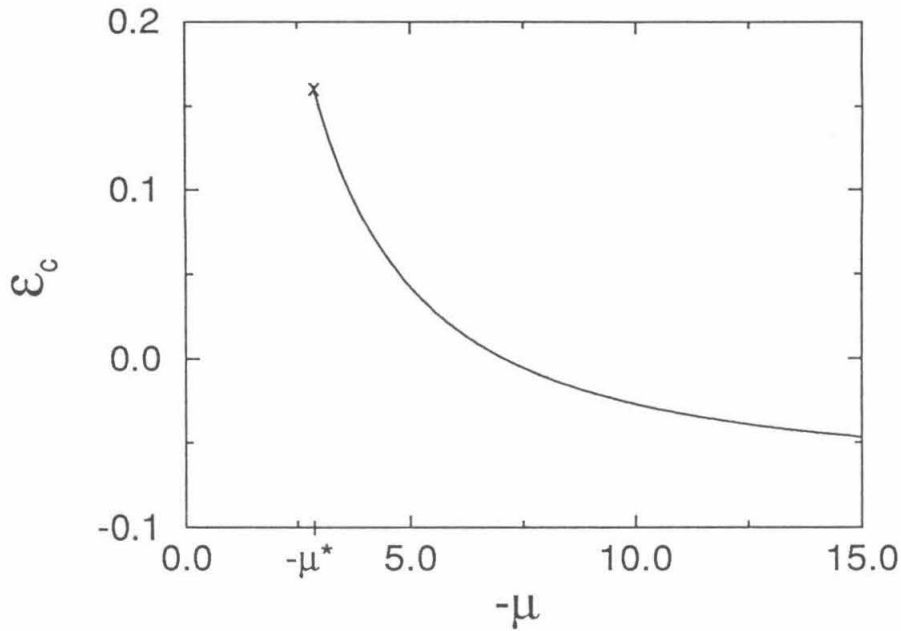


Figure 4-1: Critical ϵ , ϵ_c , as a function of μ for $\lambda = -0.1$ for the wall state in the Swift-Hohenberg model. The critical onset solution for the wall state disappears when $\mu = \mu^*$ at the point denoted by a cross.

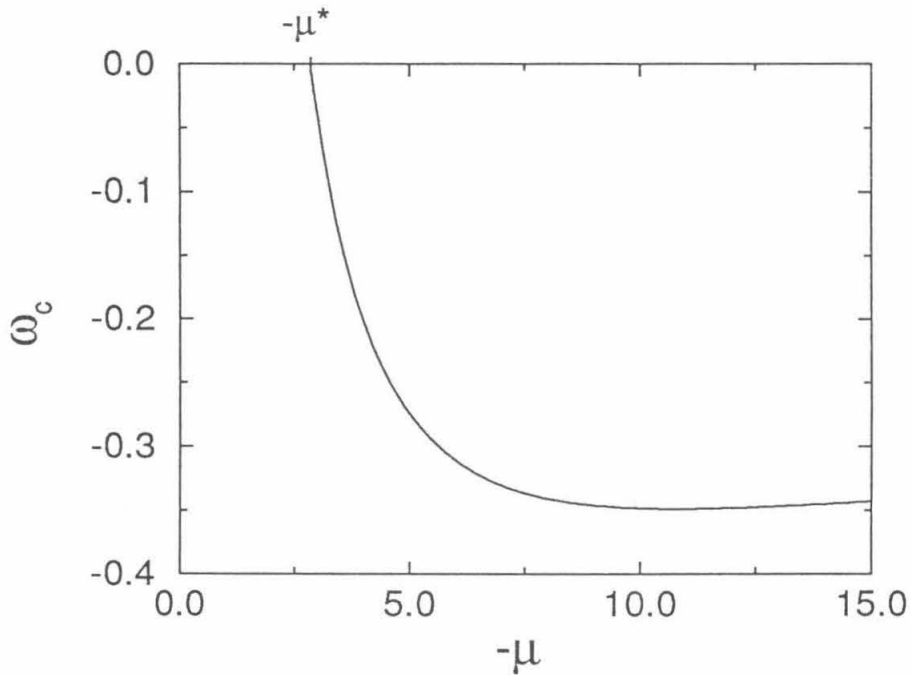


Figure 4-2: Critical frequency ω_c for $\lambda = -0.1$.

tion 3, the traveling-wave wall state in this model system exhibits the same interesting feature as the wall state in the rotating Rayleigh-Bénard convection system, *viz* the critical onset wall state disappears at some small value of the reflection-symmetry-breaking parameter, in the present case, μ . Again, the critical frequency goes to zero linearly at this point, and one of the complex wave vectors q_y becomes purely real, while the other one becomes purely imaginary (see Fig.(4-4)).

In Fig.(4-5,4-6,4-7), the onset ϵ and frequency ω , as well as the wave number normal to the wall, q_y , are shown as a function of q_x , the wave number parallel to the sidewall, for fixed λ and μ . Again, as in the the rotating Rayleigh-Bénard system, the wall state solution disappears beyond some wave number q_x^* , at which point the frequency ω approaches zero linearly, and one of the q_y becomes purely real, and the other purely imaginary.

4.2 Küppers-Lortz Instability

In 1969, Küppers and Lortz [24] showed that there exists a nonlinear instability of the parallel roll state in Rayleigh-Bénard convection in a rotating system. In this instance, they showed that for the special case of infinite Prandtl number ($\sigma \rightarrow \infty$) and free-slip boundary conditions, the parallel roll state is maximally unstable to a set of rolls oriented at 58° (in the sense of rotation) to the original set of rolls when the Taylor number ($T = (2\Omega)^2$) exceeds the critical value 2285. Later, Küppers [25] showed that the same phenomenon exists for finite Prandtl numbers and rigid

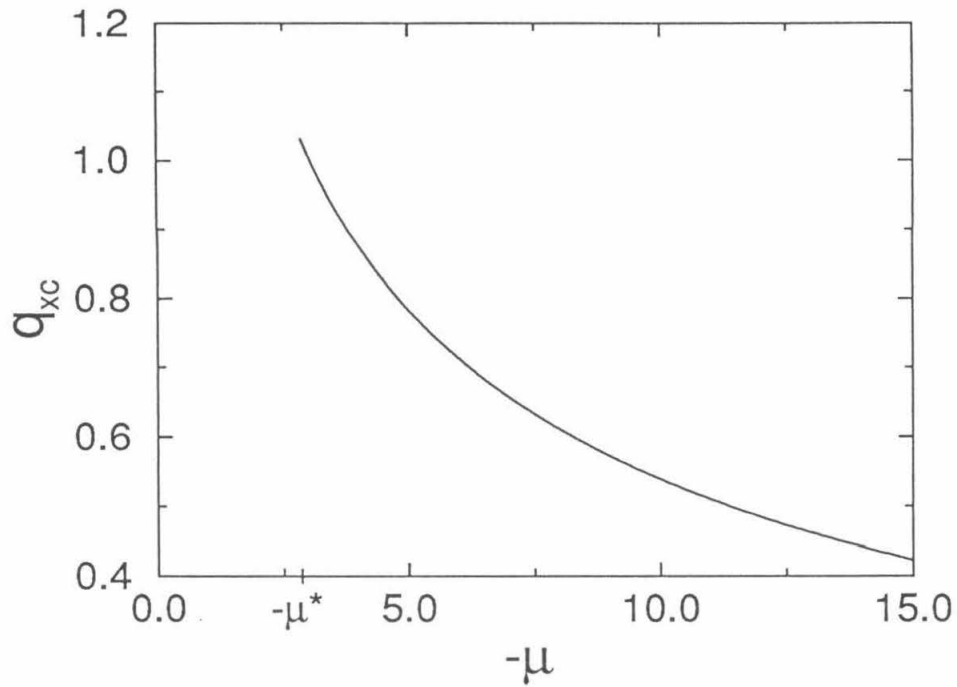


Figure 4-3: Critical wave number q_{xc} for $\lambda = -0.1$.

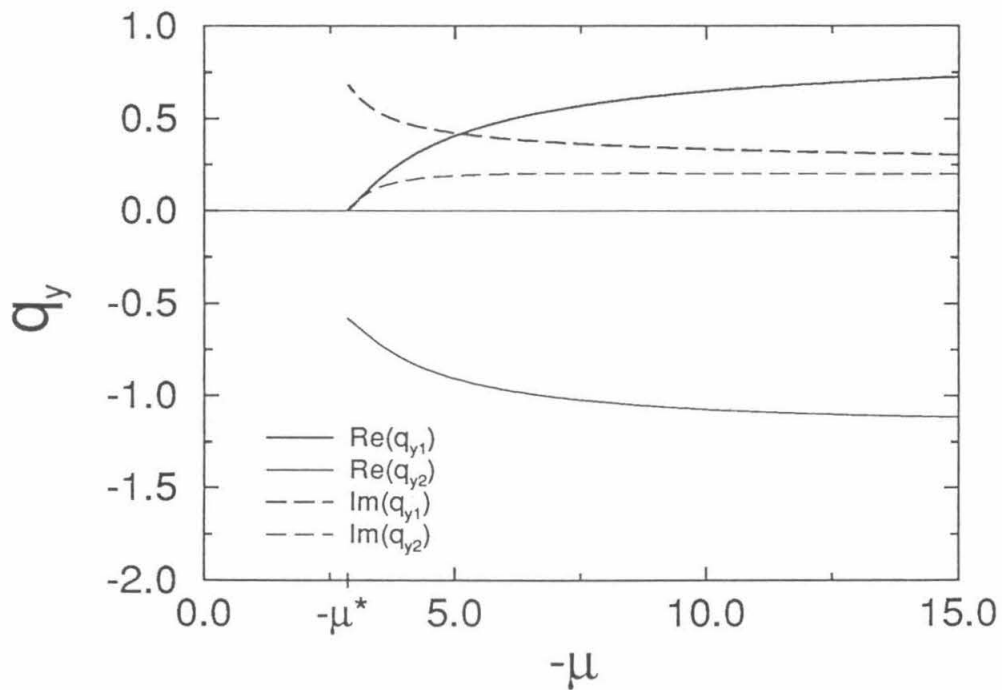


Figure 4-4: Critical wave numbers normal to the wall, q_y , for $\lambda = -0.1$.

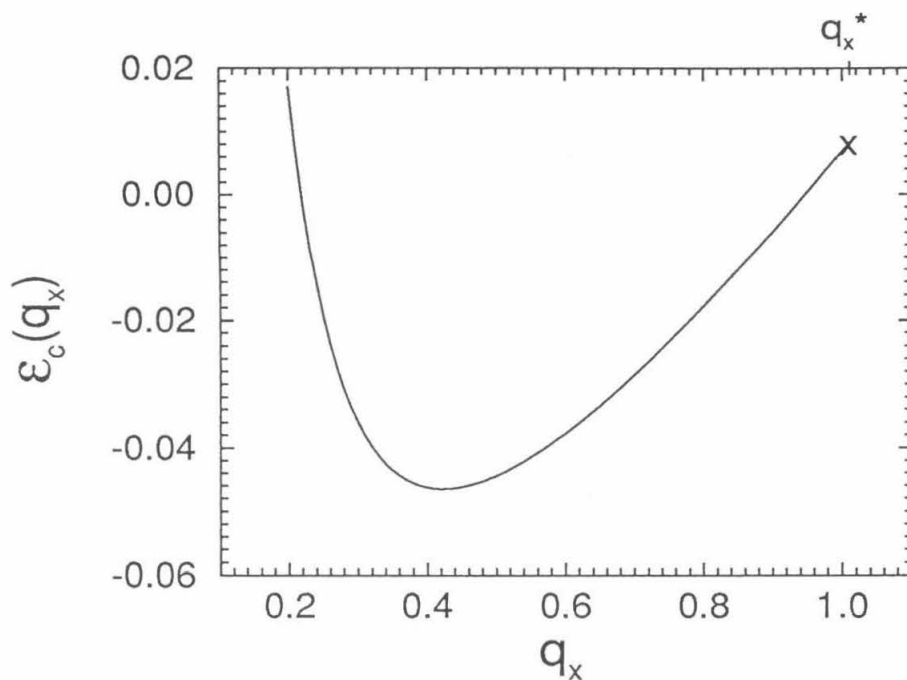


Figure 4-5: Critical ϵ as a function of q_x for $\lambda = -0.1$, $\mu = -15$. The point at which the wall state solution disappears is indicated by a cross.

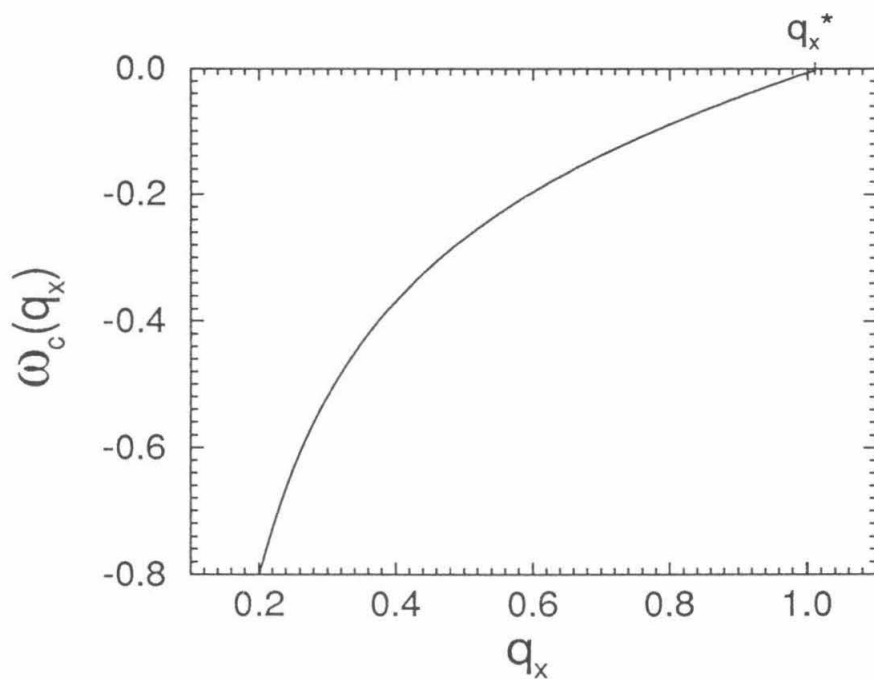


Figure 4-6: Critical frequency as a function of q_x for $\lambda = -0.1$, $\mu = -15$.

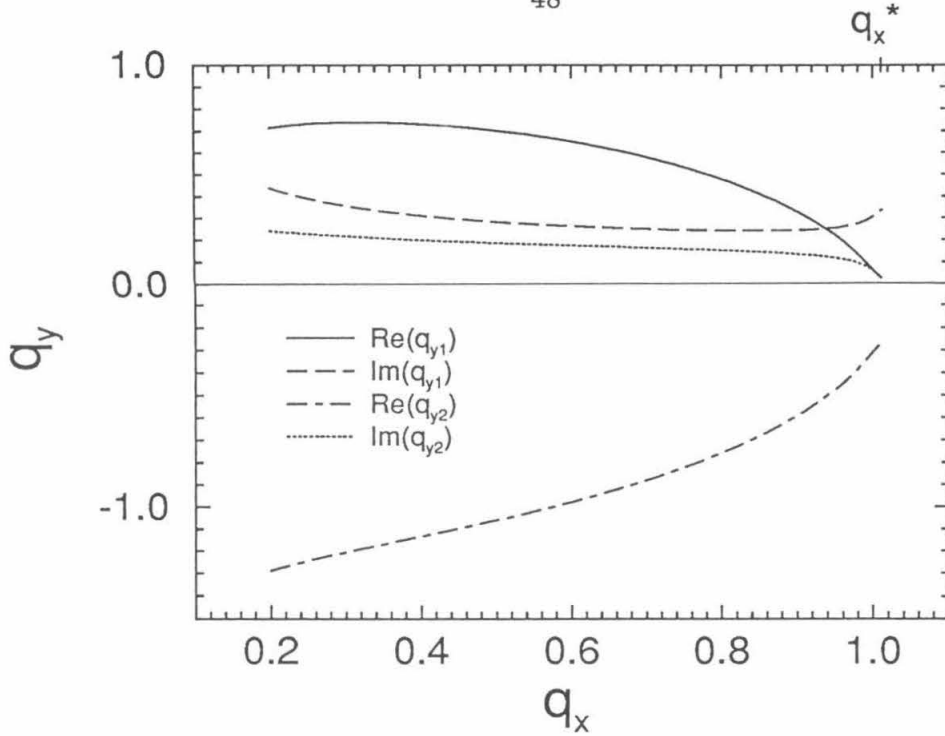


Figure 4-7: Critical q_y as a function of q_x for $\lambda = -0.1$, $\mu = -15$.

boundary conditions.

As the orientation of the set of rolls which is maximally unstable is at an angle of $58^\circ \approx 60^\circ$ with respect to the original set of rolls, Busse and Heikes [26] proposed a three mode dynamical model to study the dynamics of the system. Each mode variable A_j , with $j = 1, 2, 3$, represents the amplitude of the set of bulk rolls at a particular angle, with A_2 representing the amplitude of the set of rolls oriented at 120° with respect to the set represented by the amplitude A_1 , and so on.

The dynamical equations take the form

$$\tau_0 \frac{\partial A_j}{\partial t} = \epsilon A_j - \left(\sum_{m=1}^3 g_{jm} |A_m|^2 \right) A_j, \quad j = 1, 2, 3 \quad (4.10)$$

with $g_{11} = g_{22} = g_{33}$, and $g_{12} = g_{23} = g_{31} = g_+$, and $g_{21} = g_{32} = g_{13} = g_-$ due to the rotational symmetry. In the physical system, g_+ and g_- depend upon the rotation rate Ω . Scaling the A_j to set the $g_{jj} = 1$, the condition for the Küppers-Lortz instability to exist is $g_+ > 1$ and $g_- < 1$.

When $g_+ > 1$ and $g_- < 1$, the three variable dynamical system (4.10) has three unstable fixed points, each with two stable directions and one unstable direction. The three fixed points are, with $g_{jj} = 1$, $(A_1, A_2, A_3) = (A_0, 0, 0)$, $(0, A_0, 0)$ and $(0, 0, A_0)$, where $A_0^2 = \epsilon$, and are joined by a heteroclinic orbit. In the absence of noise or other disturbances, any orbit would gradually approach the heteroclinic orbit, thus the system would spend longer and longer periods of time in the neighborhood of each of the unstable fixed points, and the return time would eventually diverge. This was first shown by May and Leonard [27] for these equations in the context of competing and interacting species.

The case of diverging return times is not observed experimentally, and Busse and Heikes [26] proposed the addition of random noise to explain the finite but fluctuating return times observed. They also pointed out the likelihood of the importance of the spatial dependence of the rolls, which would be another source of disturbance. In 1992, Tu and Cross [28] studied the three mode model including the spatial dependence, and (4.10) becomes a set of coupled amplitude equations,

$$\frac{\partial A_1}{\partial t} = \frac{\partial^2 A_1}{\partial x_1^2} + A_1(1 - A_1^2 - g_- A_2^2 - g_+ A_3^2), \quad (4.11)$$

and the two equations with the permutations $1 \rightarrow 2 \rightarrow 3$,

(where x_1 is the coordinate in the direction of the wave vector \vec{q}_1 , *i.e.*, $x_1 = \vec{x} \cdot \vec{q}_1$, $|\vec{q}_1| = 1$), in a two-dimensional periodic geometry. Though they did not include random noise in their model, they found, amongst other things, that there is a finite characteristic switching time (which, not surprisingly, depends upon the nonlinear interaction coefficients, g_+ and g_-).

The above model, though it includes the aspect of diffusing domains of rolls, does not address the question of whether the three types of domains themselves are well-defined entities – the orientation of the domains of rolls could be changing in time, there could effectively be more than three domain orientations, and at any particular point, there may not be a well-defined domain or orientation. These aspects are not included in the three domain orientation model (4.11), but could exist in a real system, and may affect the long-term dynamics of the system. The effects of sidewall boundaries (as must exist in any real system) upon the dynamics is also not included as the boundary conditions were periodic in both directions.

4.2.1 Modified Swift-Hohenberg Model

A modified Swift-Hohenberg model, with a modified nonlinear term, can be used to mimic the Küppers-Lortz instability. A modified model [29] is

$$\frac{\partial \psi}{\partial t} = \epsilon \psi - (\nabla^2 + q_0^2)^2 \psi - g_1 \psi^3 + g_2 \hat{z} \cdot \nabla \times (|\nabla \psi|^2 \nabla \psi) + g_3 \nabla \cdot (|\nabla \psi|^2 \nabla \psi), \quad (4.12)$$

where, as before, the system is in the $x - y$ plane, \hat{z} is the unit vector normal to this plane, and q_0 is taken to be 1. Thus the nonlinear term $g_2 \hat{z} \cdot \nabla \times (|\nabla \psi|^2 \nabla \psi)$ breaks the reflection symmetry at the nonlinear pattern selection level.

We can write ψ in terms of the rolls at various orientations \vec{q}_j , ($|\vec{q}_j| = 1$):

$$\psi = A_1 e^{i\vec{q}_1 \cdot \vec{x}} + A_2 e^{i\vec{q}_2 \cdot \vec{x}} + \dots + c.c.. \quad (4.13)$$

The amplitude equations for the A_j take the form,

$$\frac{\partial A_j}{\partial t} = \epsilon A_j + (2q_0)^2 \left(\frac{\partial}{\partial x_j} - \frac{i}{2q_0} \frac{\partial^2}{\partial y_j^2} \right)^2 A_j - g_0 |A_j|^2 A_j - \sum_{k \neq j} g(\theta_{jk}) |A_k|^2 A_j, \quad (4.14)$$

where θ_{jk} is the angle from \vec{q}_j to \vec{q}_k ,

$$\text{and } g_0 = \frac{1}{2} g(\theta_{jj}) = 3(g_1 + g_3),$$

$$g(\theta_{jk}) = 6g_1 + 2g_2 \sin(2\theta_{jk}) + 4g_3 + 2g_3 \cos(2\theta_{jk}),$$

and the coordinates are $x_j = \vec{x} \cdot \vec{q}_j$ and $y_j = \vec{x} \cdot (\hat{z} \times \vec{q}_j)$. The reflection symmetry is

broken by the nonlinear term $g_2 \sin(2\theta_{jk})$.

Equation (4.14) has fixed points, the equivalent of parallel roll states, at

$$A_j = \sqrt{\frac{\epsilon}{g_0}},$$

$$A_k = 0, \quad k \neq j,$$

and their stability is determined by the nonlinear terms. A stability analysis reveals that the fixed point $A_j = \sqrt{\epsilon/g_0}$, $A_k = 0$, $k \neq j$, ‘parallel roll’ pattern is unstable to perturbations in the A_k direction if

$$1 - \frac{g(\theta_{jk})}{g_0} > 0,$$

$$i.e., \quad g(\theta_{jk}) = 6g_1 + 4g_3 + 2g_2 \sin(2\theta_{jk}) + 2g_3 \cos(2\theta_{jk}) < 3g_1 + 3g_3. \quad (4.15)$$

Differentiating with respect to θ , one finds that the maximum and minimum of $g(\theta)$ occur when $\tan 2\theta = g_2/g_3$, and thus that

$$g(\theta)_{min} = 6g_1 + 4g_3 - 2\sqrt{g_2^2 + g_3^2}, \quad (4.16)$$

$$g(\theta)_{max} = 6g_1 + 4g_3 + 2\sqrt{g_2^2 + g_3^2}. \quad (4.17)$$

Provided $g_1 > 0$ (which would be the usual case), (4.15) and (4.16) imply the nonlinear

roll state $A_j = \sqrt{\epsilon/g_0}$, $A_k = 0$, $k \neq j$, will lose its stability when

$$3 + \frac{g_3}{g_1} - 2\sqrt{\left(\frac{g_2}{g_1}\right)^2 + \left(\frac{g_3}{g_1}\right)^2} < 0. \quad (4.18)$$

Thus, for example, if we wish to mimic the Küppers-Lortz instability where the rolls are maximally unstable to another set of rolls at $\theta_c = \pi/3$ to the original rolls, we would set

$$\frac{g_2}{g_3} = \tan 2\theta_c = \tan 2\left(\frac{\pi}{3}\right) = -\sqrt{3}, \quad (4.19)$$

and require (4.18)

$$3 + \frac{g_3}{g_1} - 2\sqrt{\left(\frac{-\sqrt{3}g_3}{g_1}\right)^2 + \left(\frac{g_3}{g_1}\right)^2} < 0. \quad (4.20)$$

For $g_1 > 0$, this is just $g_3/g_1 > 1$ and $g_2 = -\sqrt{3}g_3$. Note that a band of orientations $\Delta\theta \sim (g_3/g_1 - 1)^{\frac{1}{2}}$ will actually be unstable. Also, with these conditions, the fixed point $A_j = \sqrt{\epsilon/g_0}$, $A_k = 0$, $k \neq j$, is stable to perturbations in the A_k direction for $\theta_{jk} = 2\pi/3$, as $g(\theta = 2\pi/3) > 0$.

Numerical studies of the modified Swift-Hohenberg model (4.12) in the equivalent of a two-dimensional annular geometry – periodic boundary conditions in one direction (x -direction) and ‘rigid’ boundary conditions in the other (y -direction) – should thus be able to further understanding of the effects of sidewalls on the domain dynamics of the Küppers-Lortz instability.

4.3 Amplitude Equation for the Traveling-Wave Wall State

As for the traveling-wave wall state in rotating Rayleigh-Bénard convection, we can calculate the amplitude equation for the wall state in the modified Swift-Hohenberg model. The linear terms τ_0 , s , ξ_0^2 , c_0 and c_1 in the amplitude equation

$$\tau_0 \left(\frac{\partial A}{\partial t} + s \frac{\partial A}{\partial x} \right) = r(1 + ic_0)A + \xi_0^2(1 + ic_1) \frac{\partial^2 A}{\partial x^2} - g(1 + ic_3)|A|^2 A \quad (4.21)$$

are derived and calculated numerically in a similar way as before by finding the complex growth rate $\Gamma = r - i(\omega_c + \Delta\omega)$ as a function of $r = \epsilon - \epsilon_c$ and $k = q_x - q_{xc}$. For the Swift-Hohenberg model, however, $\tau_0 = 1$ and $c_0 = 0$.

In Fig.(4-8,4-9,4-10), the linear coefficients are shown as a function of μ for fixed λ .

4.3.1 Calculation of the (lowest order) Nonlinear Coefficient in the Amplitude Equation

Though to calculate the the linear coefficients in the amplitude equation one can use the method described above, to calculate the lowest order nonlinear coefficient, one may follow a multiple scales approach. Here, we will denote the ‘small’ expansion

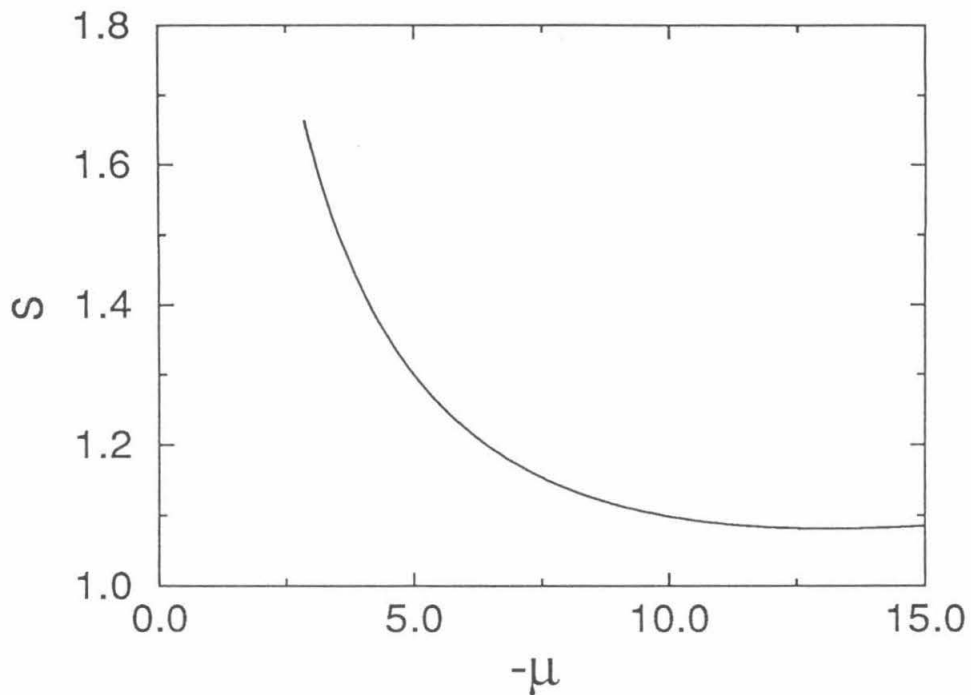


Figure 4-8: Group velocity s in the amplitude equation for $\lambda = -0.1$.

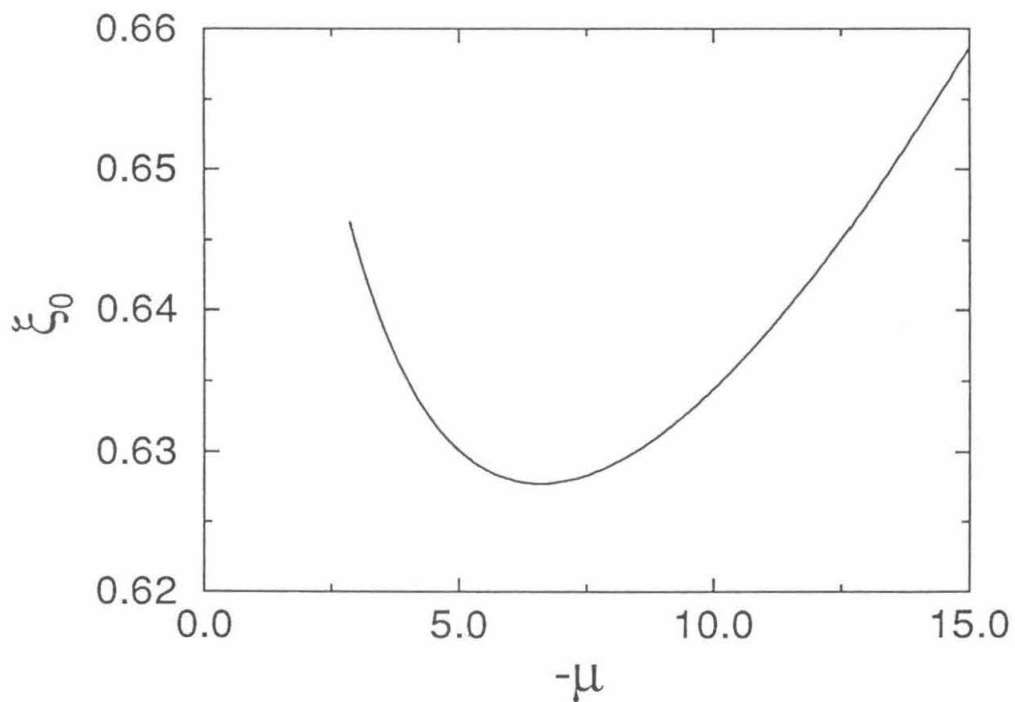


Figure 4-9: Length scale parameter ξ_0 in the amplitude equation for $\lambda = -0.1$.

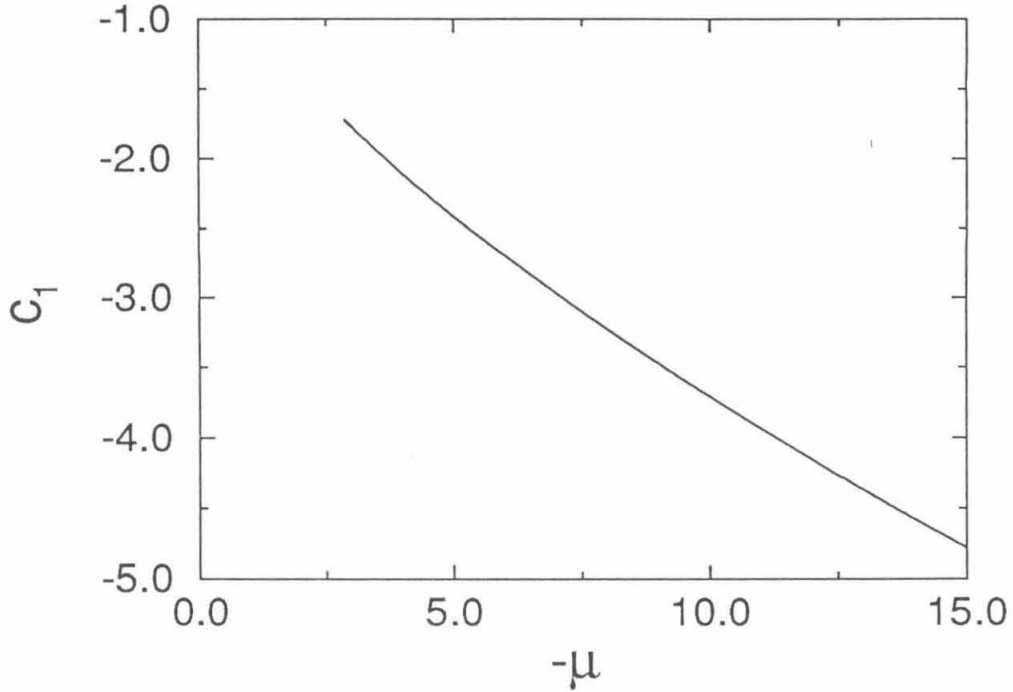


Figure 4-10: Amplitude equation parameter c_1 for $\lambda = -0.1$.

parameter as

$$r = \epsilon - \epsilon_c, \quad (4.22)$$

where ϵ_c is the critical ϵ at the instability onset of the traveling-wave wall state.

We can then expand ψ in powers of $r^{\frac{1}{2}}$ as

$$\psi = r^{\frac{1}{2}}\psi_0 + r\psi_1 + r^{\frac{3}{2}}\psi_2 + \dots, \quad (4.23)$$

where the ψ_j are formally of $O(1)$. We also introduce the slow scales T , and X by defining them as

$$X = r^{\frac{1}{2}}x,$$

$$T = rt.$$

We then separate the fast and slow variations in the differential operator by substituting

$$\begin{aligned}\frac{\partial}{\partial t} &\rightarrow \frac{\partial}{\partial t} + r \frac{\partial}{\partial T}, \\ \frac{\partial}{\partial x} &\rightarrow \frac{\partial}{\partial x} + r^{\frac{1}{2}} \frac{\partial}{\partial X},\end{aligned}$$

where $\frac{\partial}{\partial t}$ and $\frac{\partial}{\partial x}$ now act only on the fast variables t and x respectively, and $\frac{\partial}{\partial T}$ and $\frac{\partial}{\partial X}$ act correspondingly only on the respective slow variables, T and X .

Expanding (4.21) thus in powers of $r^{\frac{1}{2}}$ and defining the fast varying Laplacian to be $\tilde{\nabla}^2 = \frac{\partial^2}{\partial x^2} + \frac{\partial^2}{\partial y^2}$, we find

$O(r^{\frac{1}{2}})$:

$$\left[\frac{\partial}{\partial t} - \epsilon_c + (\tilde{\nabla}^2 + q_0^2)^2\right]\psi_0 = 0 \quad (4.24)$$

$O(r)$:

$$\left[\frac{\partial}{\partial t} - \epsilon_c + (\tilde{\nabla}^2 + q_0^2)^2\right]\psi_1 = -4(\tilde{\nabla}^2 + q_0) \frac{\partial}{\partial x} \frac{\partial}{\partial X} \psi_0 \quad (4.25)$$

and

$O(r^{\frac{3}{2}})$:

$$\begin{aligned}\left[\frac{\partial}{\partial t} - \epsilon_c + (\tilde{\nabla}^2 + q_0^2)^2\right]\psi_2 &= -4(\tilde{\nabla}^2 + q_0) \frac{\partial}{\partial x} \frac{\partial}{\partial X} \psi_1 \\ &+ \left\{-\frac{\partial \psi_0}{\partial T} + \psi_0 - (2(\tilde{\nabla}^2 + q_0^2) \frac{\partial^2}{\partial X^2} + 4 \frac{\partial}{\partial x} \frac{\partial}{\partial X})\psi_0\right.\end{aligned}$$

$$-g_1\psi_0^3 + g_2\hat{z} \cdot \tilde{\nabla} \times (|\tilde{\nabla}\psi_0|^2\tilde{\nabla}\psi_0) + g_3\tilde{\nabla} \cdot (|\tilde{\nabla}\psi_0|^2\tilde{\nabla}\psi_0)\} \quad (4.26)$$

Luckily however, since we have already calculated the linear coefficients, we can simplify the calculation by neglecting the slow spatial variation $\frac{\partial}{\partial X}$, and setting $\frac{\partial}{\partial X} \rightarrow 0$ in the equations. [Note that in (4.21) the linear group velocity term is actually ‘unbalanced’ as a power in r anyway!] Our main interest here then, is in calculating the coefficient for the nonlinear term.

The equations we wish to solve are then

$$\left[\frac{\partial}{\partial t} - \epsilon_c + (\tilde{\nabla}^2 + q_0^2)\right]\psi_0 = 0 \quad (4.27)$$

$$\left[\frac{\partial}{\partial t} - \epsilon_c + (\tilde{\nabla}^2 + q_0^2)\right]\psi_1 = 0 \quad (4.28)$$

$$\begin{aligned} \left[\frac{\partial}{\partial t} - \epsilon_c + (\tilde{\nabla}^2 + q_0^2)\right]\psi_2 &= -\frac{\partial\psi_0}{\partial T} + \psi_0 - g_1\psi_0^3 + g_2\hat{z} \cdot \tilde{\nabla} \times (|\tilde{\nabla}\psi_0|^2\tilde{\nabla}\psi_0) \\ &\quad + g_3\tilde{\nabla} \cdot (|\tilde{\nabla}\psi_0|^2\tilde{\nabla}\psi_0) \end{aligned} \quad (4.29)$$

and the boundary conditions

$$\hat{n} \cdot \tilde{\nabla}\psi_j = \lambda\psi_j \quad (4.30)$$

$$\mu\hat{z} \cdot (\hat{n} \times \tilde{\nabla})(\tilde{\nabla}^2 + q_0^2)\psi_j = \psi_j \quad (4.31)$$

to all orders in j .

The third equation, equation (4.29), provides the route to calculating the lowest order nonlinear coefficient in the amplitude equation – the Fredholm theorem, or

solvability condition, states that the RHS of (4.29) must be orthogonal to the kernel of the adjoint operator of the LHS, for a solution to (4.29) to exist. [The first two equations (4.27), (4.28) and boundary conditions (4.30 - 4.31) just state that $\psi_0(x, y, t) = A_0(X, T)u_0(x, y, t)$ and $\psi_1(x, y, t) = A_1(X, T)u_0(x, y, t)$ where $u_0(x, y, t)$ is the linear onset traveling-wave wall state solution found in §4.1.2.]

The adjoint operator L^\dagger is defined by

$$\langle v|Lu \rangle = \langle L^\dagger v|u \rangle \quad (4.32)$$

where $L = \frac{\partial}{\partial t} - \epsilon_c + (\tilde{\nabla}^2 + q_0^2)^2$ and the boundary conditions on L are (4.3), (4.4).

The scalar product $\langle v|u \rangle$ here is defined as

$$\int_{-\infty}^{\infty} dt \int_{-\infty}^{\infty} dx \int_0^{\infty} dy v^*(x, y, t)u(x, y, t). \quad (4.33)$$

The usual integration-by-parts method leads to the adjoint operator being

$$L^\dagger = -\frac{\partial}{\partial t} - \epsilon_c + (\tilde{\nabla}^2 + q_0^2)^2 \quad (4.34)$$

with boundary conditions

$$v = 0 \quad (4.35)$$

and

$$\mu\lambda\hat{z}\cdot(\hat{n}\times\tilde{\nabla})(\tilde{\nabla}^2+q_0^2)v-\mu\hat{z}\cdot(\hat{n}\times\tilde{\nabla})(\hat{n}\cdot\tilde{\nabla})[(\tilde{\nabla}^2+q_0^2)v+2(1-q_0^2)v]+(\hat{n}\cdot\tilde{\nabla})v=0. \quad (4.36)$$

Assuming the solutions to be of the form

$$v(x, y, t) = e^{i(q_x x - \omega t)} \tilde{v}(y) \quad (4.37)$$

leads to more practical expressions for the boundary conditions of

$$\tilde{v} = 0 \quad (4.38)$$

and

$$i\mu q_x \frac{\partial}{\partial y} \left(\left(\frac{\partial^2}{\partial y^2} - q_x^2 + q_0^2 \right) + 2(1 - q_0^2) \right) \tilde{v} - i\mu\lambda q_x \left(\frac{\partial^2}{\partial y^2} - q_x^2 + q_0^2 \right) \tilde{v} + \frac{\partial \tilde{v}}{\partial y} = 0 \quad (4.39)$$

$$\text{at } y = 0.$$

(Actually (4.35) and (4.36) were deduced from (4.38) and (4.39).)

4.3.2 Solving for the Kernel of the Adjoint Operator

As for solving the original problem, we will assume a solution in the kernel of the adjoint problem of the form

$$v(x, y, t) = \tilde{v}(y)e^{i(q_x x - \omega t)} = e^{i(q_x x - \omega t)} \sum_{j=1,2} \tilde{v}_j e^{i k_{yj} y} \quad (4.40)$$

where ω , q_x , k_{yj} satisfy the dispersion relation

$$0 = i\omega - \epsilon_c + (q_x^2 + k_{yj}^2 - q_0^2)^2. \quad (4.41)$$

As this is just the complex conjugate of the dispersion relation in the original problem, it follows that (since we still require $Im(k_{yj}) \geq 0$) the relevant wave vectors in the y -direction are

$$k_{y1} = -q_{y1}^*,$$

$$\text{and } k_{y2} = -q_{y2}^*,$$

where the q_{yj} would be the wave vectors for the original problem also with a traveling-wave dependence $e^{i(q_x x - \omega t)}$. Thus the kernel of the adjoint operator L^\dagger will be functions of the form

$$v(x, y, t) = e^{i(q_x x - \omega t)} \sum_{j=1,2} \tilde{v}_j e^{i k_{yj} y} = e^{i(q_x x - \omega t)} \sum_{j=1,2} \tilde{v}_j e^{-i q_{yj}^* y},$$

indexed by the wave number q_x , whilst the kernel of the operator L will be functions of the form

$$\psi(x, y, t) = e^{i(q_x x - \omega t)} \sum_{j=1,2} \tilde{\psi}_j e^{i q_{yj} y}, \quad (4.42)$$

with the \tilde{v}_j and $\tilde{\psi}_j$ determined by the appropriate respective boundary conditions (4.35 - 4.36) and (4.30 - 4.31). Not surprisingly, it turns out that for a given q_x , the frequency, ω , that leads to solutions satisfying both the original and the adjoint boundary conditions is the same. Thus it is easy to see, using boundary condition (4.35) that the kernel of the adjoint problem consists of functions of the form

$$v(x, y, t) = e^{i(q_x x - \omega t)} \sum_{j=1,2} \tilde{v}_j e^{-i q_{yj}^* y} \quad (4.43)$$

$$\text{with } \tilde{v}_2 = -\tilde{v}_1,$$

and with ω and q_{yj} for a given q_x determined through the original problem.

To calculate the nonlinear coefficient of the amplitude equation we expand the RHS of (4.29) and take its scalar product with the kernel of the adjoint operator given by (4.43). The normalization we will choose is

$$|\tilde{u}_{01} + \tilde{u}_{02}| = 1 \quad (4.44)$$

so that the maximum of ψ at $y = 0$ is

$$\psi_{max} = 2r^{\frac{1}{2}} |A_0|, \quad (4.45)$$

since

$$\psi(x, y, t) = r^{\frac{1}{2}} A_0 e^{i(q_0 x - \omega t)} \sum_{j=1,2} \tilde{u}_{0j} e^{iq_{yj} y} + c.c.. \quad (4.46)$$

Thus we find that the amplitude equation (without its spatial derivative part) is

$$\frac{\partial A_0}{\partial T} = A_0 - \left(g_1 \frac{\eta_1}{\eta_0} - g_2 \frac{\eta_2}{\eta_0} - g_3 \frac{\eta_3}{\eta_0} \right) |A_0|^2 A_0, \quad (4.47)$$

where

$$\begin{aligned} \eta_0 &= i \sum_{j,m=1,2} \frac{\tilde{v}_j^* \tilde{u}_m}{q_{yj} + q_{ym}}, \\ \eta_1 &= 3i \sum_{j,l,m,n=1,2} \frac{\tilde{v}_j^* \tilde{u}_l^* \tilde{u}_m \tilde{u}_n}{(q_{yj} - q_{yl}^* + q_{ym} + q_{yn})} \\ \eta_2 &= 2iq_x \sum_{j,l,m,n=1,2} \frac{1}{(q_{yj} - q_{yl}^* + q_{ym} + q_{yn})} \{ -2q_x^2 \tilde{v}_j^* (q_{yl} \tilde{u}_l)^* \tilde{u}_m \tilde{u}_n \\ &\quad + 2q_x^2 \tilde{v}_j^* \tilde{u}_l^* \tilde{u}_m (q_{yn} \tilde{u}_n) - \tilde{v}_j^* (q_{yj}^2 \tilde{u}_l)^* \tilde{u}_m (q_{yn} \tilde{u}_n) \\ &\quad + \tilde{v}_j^* (q_{yl} \tilde{u}_l)^* \tilde{u}_m (q_{yn}^2 \tilde{u}_n) + \tilde{v}_j^* \tilde{u}_l^* (q_{ym} \tilde{u}_m) (q_{yn}^2 \tilde{u}_n) \\ &\quad - \tilde{v}_j^* (q_{yl} \tilde{u}_l)^* (q_{ym} \tilde{u}_m) (q_{yn} \tilde{u}_n) \} \end{aligned}$$

and

$$\begin{aligned} \eta_3 &= i \sum_{j,l,m,n=1,2} \frac{1}{(q_{yj} - q_{yl}^* + q_{ym} + q_{yn})} \{ -3q_x^4 \tilde{v}_j^* \tilde{u}_l^* \tilde{u}_m \tilde{u}_n \\ &\quad - 3q_x^2 \tilde{v}_j^* \tilde{u}_l^* (q_{ym} \tilde{u}_m) (q_{yn} \tilde{u}_n) - 2q_x^2 \tilde{v}_j^* (q_{yl} \tilde{u}_l)^* (q_{ym} \tilde{u}_m) \tilde{u}_n \\ &\quad + 3\tilde{v}_j^* (q_{yl}^2 \tilde{u}_l)^* (q_{ym} \tilde{u}_m) (q_{yn} \tilde{u}_n) - 6\tilde{v}_j^* (q_{yl} \tilde{u}_l)^* (q_{ym} \tilde{u}_m) (q_{yn}^2 \tilde{u}_n) \\ &\quad + q_x^2 \tilde{v}_j^* (q_{yl}^2 \tilde{u}_l)^* \tilde{u}_m \tilde{u}_n - 2q_x^2 \tilde{v}_j^* \tilde{u}_l^* \tilde{u}_m (q_{yn}^2 \tilde{u}_n) \}. \end{aligned}$$

Thus the cubic order nonlinear coefficient in the amplitude equation

$$\frac{\partial A}{\partial t} + s \frac{\partial A}{\partial x} = r^{\frac{1}{2}} A + \xi_0^2 (1 + i c_1) \frac{\partial^2 A}{\partial x^2} - G |A|^2 A \quad (4.48)$$

for the traveling-wave wall state is

$$G = \eta_0^{-1} (g_1 \eta_1 - g_2 \eta_2 - g_3 \eta_3), \quad (4.49)$$

with the normalization $\psi_{max} = 2|A|$ at $y = 0$.

Examples of $c_{g1} = \eta_0^{-1} \eta_1$, $c_{g2} = \eta_0^{-1} \eta_2$, $c_{g3} = \eta_0^{-1} \eta_3$ and G are shown in Fig.(4-11,4-12).

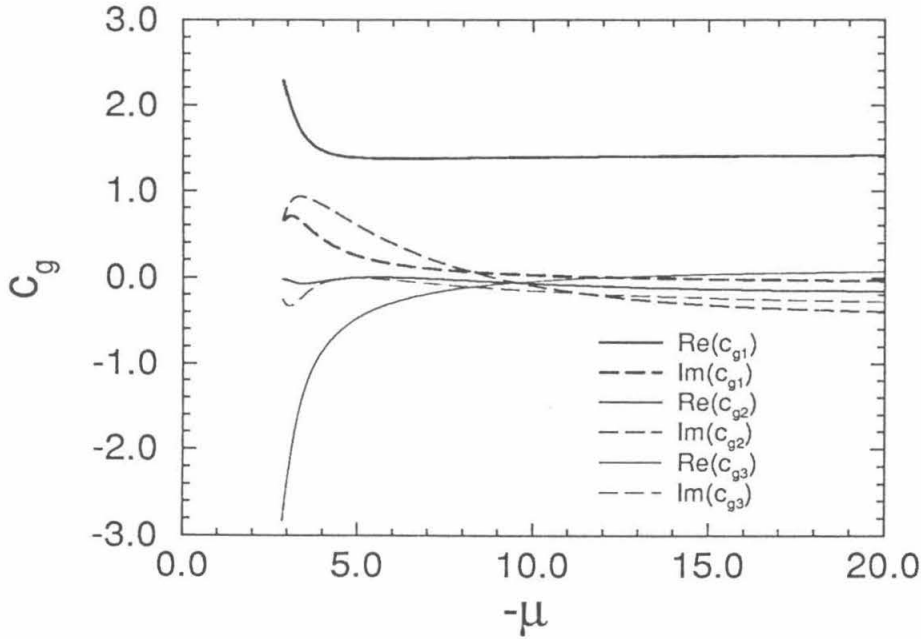


Figure 4-11: Nonlinear coefficient scaling factors c_{g_i} for the amplitude equation when $\lambda = -0.1$.

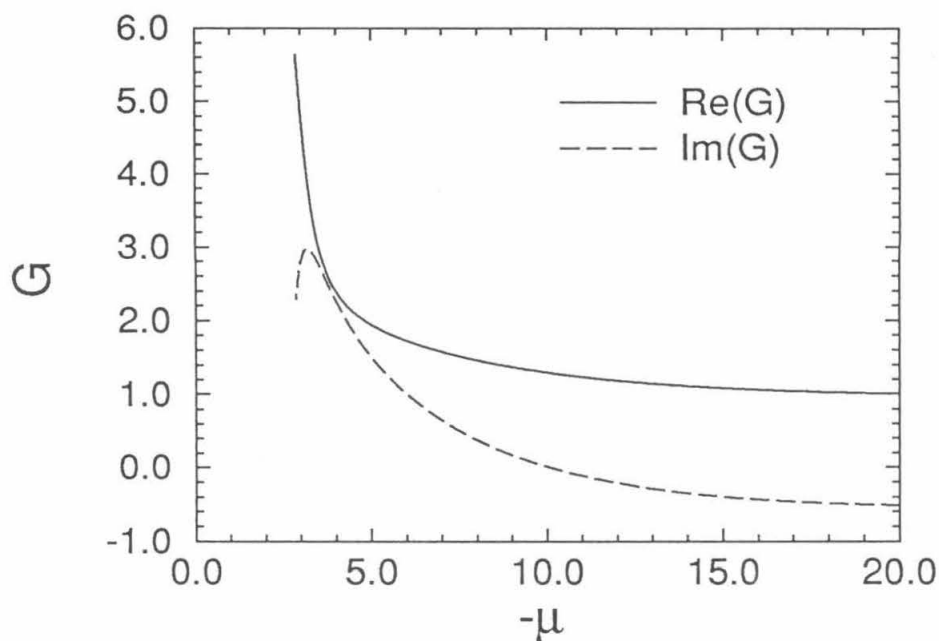


Figure 4-12: Nonlinear coefficient G for $g_1 = 1$, $g_2 = -2.078$, and $g_3 = 1.2$ when $\lambda = -0.1$.

An important known nonlinear instability for traveling-waves is the Benjamin-Feir instability [1]. The Newell criterion for the instability is

$$1 + c_1 c_3 < 0$$

when all plane wave solutions become unstable. Thus we will also be interested in the quantity

$$1 + c_1 \cdot \frac{\text{Im}(G)}{\text{Re}(G)},$$

an example of which is shown in Fig.(4-13).

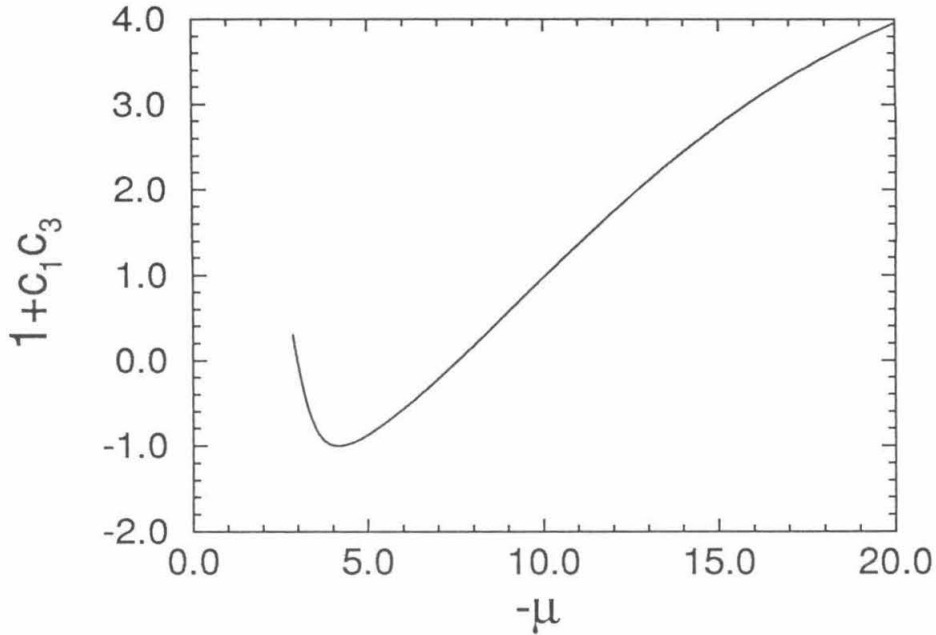


Figure 4-13: The quantity $1 + c_1c_3$ in the Newell criterion for the Benjamin-Feir instability (see text), for the same parameters as in Fig.(4-12).

4.4 Numerical Study of the Traveling-Wave Wall State in the Swift-Hohenberg Model

A numerical study of Swift-Hohenberg models in an annular geometry – periodic boundary conditions in the x -direction and ‘rigid’ boundary conditions in the y -direction – provides the means for

- understanding the wall state – bulk state transition at the point where the wall state ‘disappears’, and

- investigating the effects of the traveling-wave wall state (and the effects of finite-size) on the bulk state, especially the chaotic dynamics associated with the Küppers-Lortz instability.

In this section, we will describe the algorithm used in the numerical study, and some general observations of the numerics. In the next section we will study in detail the wall – bulk transition region. A true investigation of the effects of the wall state and the finite-size effects on the chaotic dynamics must be left to the future, though a sample simulation will be included to give a foretaste of what may be found.

4.4.1 Numerical Algorithm

The advantage, which is also the reason, for having periodic boundary conditions in one of the directions (here, the x -direction) lies in the ability thus to decompose the problem into Fourier modes in this direction and to incorporate the pseudospectral method. In the other direction (the y -direction), since there are ‘rigid’ boundary conditions, one uses finite differences to approximate the spatial derivatives, and iterates in time (for each Fourier mode) using the Crank-Nicholson method. A more detailed exposition of the method follows.

The basic idea underlying the pseudospectral method is that it is easier to calculate nonlinear terms in real space than in Fourier space where a cubic term, for example, would involve three summations over all possible wave vectors. This would necessitate of the order of M^3 operations when there are M wave vectors. The spatial derivatives,

on the other hand, are much better calculated in Fourier space, since the derivative $\frac{\partial}{\partial \mathbf{x}}$ is just multiplication by $i\mathbf{q}$ in Fourier space. The pseudospectral method thus alternates between real and Fourier space, calculating the nonlinear term in real space, but stepping forward in time and calculating the spatial derivatives in Fourier space. The transforms between real and Fourier space, through the use of the Fast Fourier Transform (FFT's), involve only of the order $M \log M$ operations at each time step.

The actual iteration scheme used for stepping forward in time is the Crank-Nicholson scheme, which is accurate to second-order in time. In this method the differential equation is discretized in time in the following way:

$$\begin{aligned} \frac{\psi(t + \Delta t) - \psi(t)}{\Delta t} &= \frac{1}{2}[\epsilon - (\nabla^2 + 1)^2](\psi(t + \Delta t) + \psi(t)) \\ &\quad + 1.5N[\psi(t)] - 0.5N[\psi(t - \Delta t)] \end{aligned} \quad (4.50)$$

where N stands for the nonlinear term. This can be rewritten with the unknown values at time $t + \Delta t$ on the LHS of the equation as

$$\begin{aligned} 2\frac{\psi(t + \Delta t)}{\Delta t} - (\epsilon - (\nabla^2 + 1)^2)\psi(t + \Delta t) &= 2\frac{\psi(t)}{\Delta t} + (\epsilon - (\nabla^2 + 1)^2)\psi(t) \\ &\quad + 3N[\psi(t)] - N[\psi(t - \Delta t)]. \end{aligned} \quad (4.51)$$

For the Fourier mode e^{iqx} , this can be written as

$$\begin{aligned}
& \frac{\partial^2 \zeta_q(t + \Delta t)}{\partial y^2} + 2(1 - q^2)\zeta_q(t + \Delta t) + ((q^2 - 1)^2 - \epsilon + \frac{2}{\Delta t})\tilde{\psi}_q(t + \Delta t) \\
&= -\left[\frac{\partial^2 \zeta_q(t)}{\partial y^2} + 2(1 - q^2)\zeta_q(t) + ((q^2 - 1)^2 - \epsilon + \frac{2}{\Delta t})\tilde{\psi}_q(t)\right] + \frac{4}{\Delta t}\tilde{\psi}_q(t) \\
&\quad + 3N_q[\psi(t)] - N_q[\psi(t - \Delta t)]
\end{aligned} \tag{4.52}$$

$$\frac{\partial^2 \tilde{\psi}_q(t + \Delta t)}{\partial y^2} - \zeta_q(t + \Delta t) = 0 \tag{4.53}$$

$$\text{where } \zeta_q = \frac{\partial^2 \tilde{\psi}_q}{\partial y^2}.$$

The coupled equations (4.52 - 4.53) for $\tilde{\psi}_q(t + \Delta t)$ and $\zeta_q(t + \Delta t)$ are now solved by discretizing in space in the y -direction, and using fourth-order finite differencing to approximate the spatial derivatives. The resulting equations are then a matrix

equation of the form ($j = 0, 1, \dots, m - 1, m$ are the y -grid points)

$$\mathbf{M}_q \begin{pmatrix} \tilde{\psi}_q^0(t + \Delta t) \\ \zeta_q^0(t + \Delta t) \\ \tilde{\psi}_q^1(t + \Delta t) \\ \zeta_q^1(t + \Delta t) \\ \vdots \\ \tilde{\psi}_q^{m-1}(t + \Delta t) \\ \zeta_q^{m-1}(t + \Delta t) \\ \tilde{\psi}_q^m(t + \Delta t) \\ \zeta_q^m(t + \Delta t) \end{pmatrix} = \mathbf{R}_q(t, t - \Delta t) \quad (4.54)$$

where \mathbf{R}_q is a vector containing the known values of the RHS of (4.52) - (4.53), and \mathbf{M}_q is a band diagonal matrix since one only needs four neighboring grid points for the fourth-order finite differencing approximation of the spatial derivatives, and there are otherwise no non-local terms in the differential equation. The boundary conditions (4.3)-(4.4) are imposed at the points $j = 0$ and $j = m$, so that the first and last two rows of \mathbf{M}_q 'express' the discretized version of the boundary conditions.

The vector of unknown $\tilde{\psi}_q^j$'s and ζ_q^j 's at time $t + \Delta t$ in (4.54) can now be solved essentially by inverting the matrix \mathbf{M}_q in the matrix equation (4.54). In practice however, (4.54) is solved using the LU decomposition method for a band diagonal matrix. The factored matrix \mathbf{M}_q for each q only needs to be calculated once at the

beginning of a numerical run and is then stored. Furthermore, because the matrix is of compact diagonal form, the number of memory locations required for each matrix M_q is only of the order m instead of m^2 . The specific 'blackbox' algorithm code we used for this was from the library LINPACK. The algorithm procedure can be summarized in the schematic diagram of Fig.(4-14).

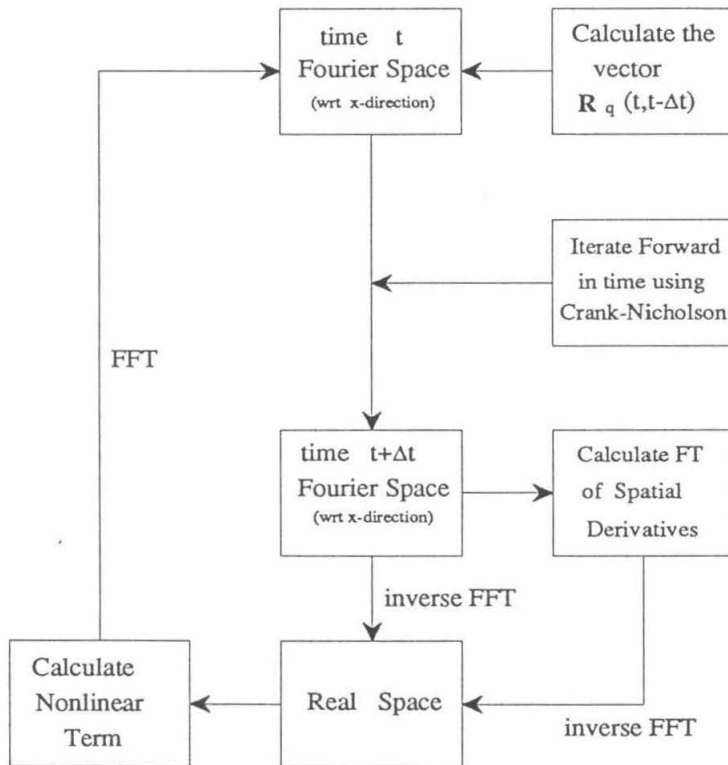


Figure 4-14: Schematic diagram for the numerical algorithm.

The code was tested in various ways. First, the linear part was tested by using as the initial condition a known time-independent analytic solution and checking that the output solution was the input solution (with allowances made for 'errors' due to the use of the finite-difference approximations for the spatial derivatives in y). Other

tests of the linear part included checking that the error in the solution scales with Δt as $(\Delta t)^2$ when Δt is small, and that the error scales with Δy as $(\Delta y)^4$ when Δy is small. There was no noticeable error scaling with Δx , which is as expected, since this error should scale as $\exp(-q_{max}^4 t)$.

The nonlinear part was tested by making the nonlinear term a linear function and checking the results against the equivalent linear problem. It was also checked by testing observed saturation amplitudes against expected saturation values. The flexible grid code (see next section) was further tested against the even grid code, with the time evolution at corresponding positions checked against one another.

In Fig.(4-15) we show a wall state for the parameters $\lambda = -0.5, \mu = -15, g_1 = 1, g_2 = g_3 = 0$ at $\epsilon = -1.15$.

4.4.2 Grid Selection in the y -direction

The grid division in the y -direction was in the initial phase an evenly spaced grid (the actual grid size naturally was variable). But because the boundary layers usually require a finer grid size than the bulk region to support the traveling-wave state, this presents a limitation on the size of the system one can simulate. To circumvent this problem, the y -direction was later divided into three regions – the two boundary regions on the two ends, and a bulk region. Within each of these regions, the grid division was again an evenly spaced one for simplicity of definition. The two boundary regions, in practice, always had the same sized grid spacings. This method allows one

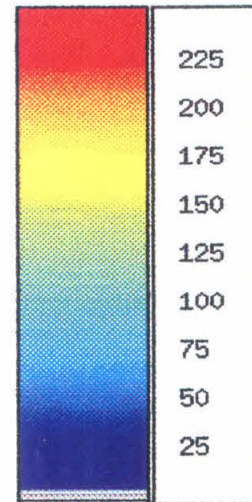
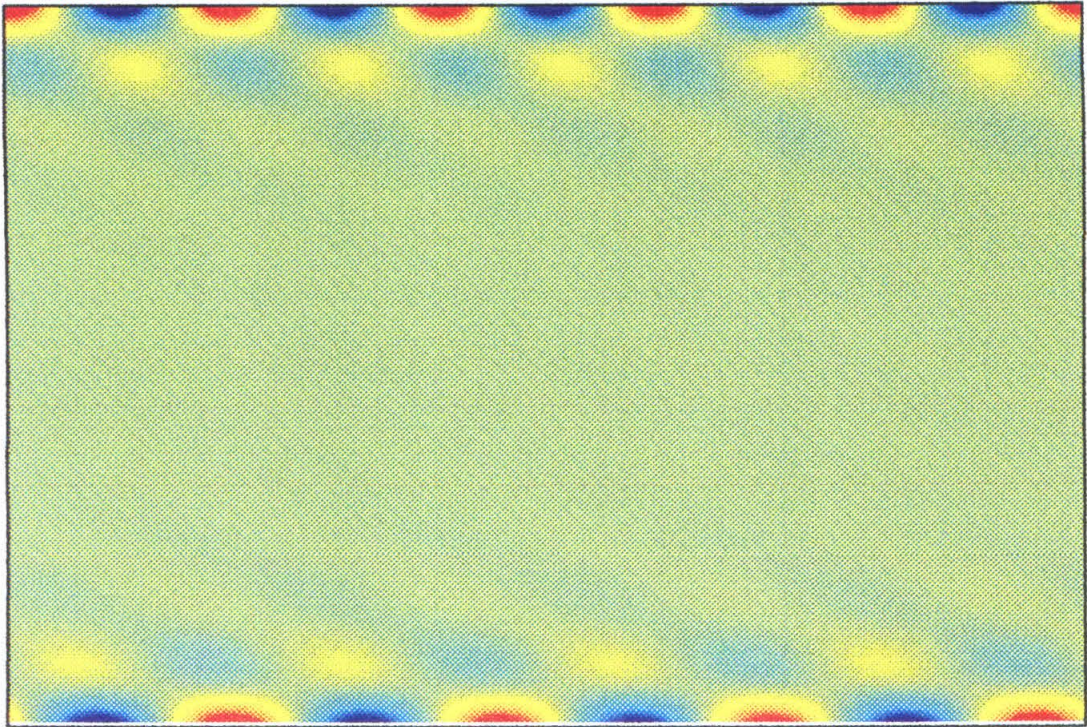


Figure 4-15: Wall state: For parameters see text. System size is $l_x = 128, l_y = 30$; grid is $\Delta x = 1, \Delta y = 1/3$ in both the boundary and bulk regions. The x -axis is from left to right, and the y -axis is from top to bottom. The wall state at $y = 0$ is traveling to the left (negative phase velocity), and that at $y = l_y$ is traveling to the right.

to simulate much larger systems. The choice of grid size and width of the boundary region was made mainly through the method of ‘guess and test’. The initial choice of grid was usually arrived at through the method described below.

Since there are two complex q_y modes in the linear wall state, there are two decay lengths and two oscillatory wavelengths. Usually, the width of the boundary region was chosen to be ‘several’ (*e.g.*, three) times the more slowly decaying decay length ($e^{-3} < 0.05$), and the grid size was chosen such that there would be ‘several’ (*e.g.*, five) grid points per decay length of the faster decaying decay length. Furthermore, it was then checked that there was at least six to ten grid points per wavelength of the faster oscillating wavelength. The actual grid densities needed for the same accuracy in the amplitude seemed to also depend on the values of the g_j . The grid size in the bulk region was usually chosen to be $q_0^{-1} = 1$, because this gives approximately six grid points per bulk wavelength (2π). Note that if the decay length and oscillating wavelength of the more slowly decaying wavelength were sufficiently large that the bulk grid size would meet the requisite criteria, then the boundary region can be appropriately decreased in width.

With the above method for choosing the initial grid size and boundary regions, the choice was then tested by seeing if the amplitude of the wall state was in sufficient agreement with the prediction of the amplitude equation. Another method consisted of doubling the grid density and/or doubling the width of the boundary regions and checking that the basic dynamics did not change.

4.4.3 An (Unexplained) Observed Nonlinear Instability

An instability that cannot obviously be explained within the amplitude equation description of the traveling-wave wall state was observed for certain parameters. More specifically, it seems to occur sometimes when $g_3 \neq 0$. In the following, we will describe a fairly detailed investigation of this instability, including the tests performed to check that it is not (obviously) a numerical problem but a ‘physical’ instability of the equations.

The instability was observed in one instance for the parameters $\lambda = -0.1$, $\mu = -15$, $g_1 = g_2 = 0$ and $g_3 = -20$. The instability appears to be caused by the size of the nonlinearity as it occurs where $\epsilon = -0.02$ but not when $\epsilon = -0.0455066$. For these parameters the critical onset traveling-wave wall state has $\epsilon_c = -0.0465066$, $q_{xc} = 0.422675$, ($\lambda_c = 14.8653$), and $\omega_c = -0.343127$. The coefficients of its amplitude equation are $s = 1.0847$, $\xi_0^2 = 0.43348$, $c_1 = -4.7863$ and $G = (0.68526, -4.7623) = g(1 + ic_3)$. For these parameters then, we observe that there should be no Benjamin-Feir instability as $1 + c_1c_3 = 34.263 > 0$. The feature that may be relevant to understanding the instability is perhaps the large (absolute values) of c_1 and c_3 .

The instability manifests itself (numerically at least) as a delta-function-like peak in the x -direction, and a decaying oscillation in the y -direction. If one starts with a periodic initial condition, then one gets a periodic series of delta-function-like peaks. A Fourier spectrum analysis at fixed y near the boundary shows the higher q_x modes growing in amplitude. An example is shown in Fig.(4-16).

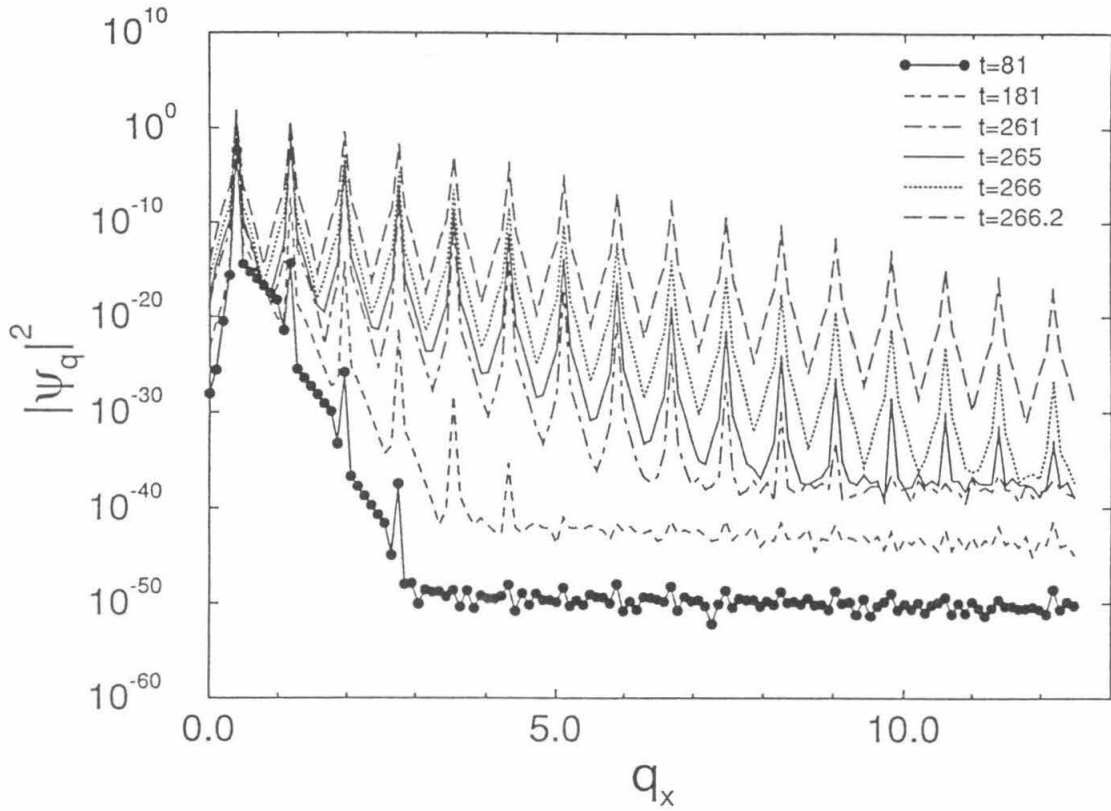


Figure 4-16: Fourier spectra at different times t at $y = 1.5$ for the initial condition $\psi_0 = 10^{-4} \sin(0.392699x)$ and $\epsilon = -0.02$; $\Delta x = 0.5$, and in the boundary region $\Delta y = 0.25$. (For more details see text.)

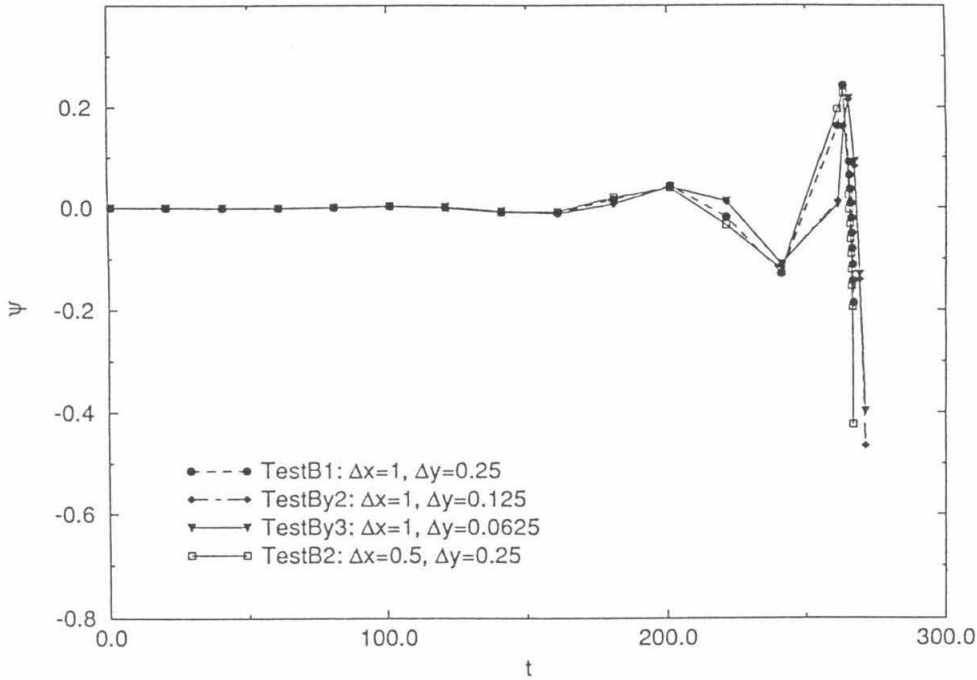


Figure 4-17: $\psi(t)$ at $(x = 4, y = 0)$ for various grids (Δy is for the boundary region).

To check that this instability was not due to the choice of grid size in either the x or y directions, the grid size in each direction was successively halved (with the width of the boundary region kept at 20). Plotting the change in ψ as a function of time for example, we observe (see Fig.(4-17)) that the ‘blow-up’ occurs at about the same time independent of the grid size. This is indicative of a finite-time singularity [22].

One item, however, remains that should make one somewhat wary about concluding that this is definitely a physical nonlinear instability. We observed that for the grid size of $\Delta y = 0.5$ in the boundary region,

- there was a ‘blow-up’ even for $\epsilon = -0.0455066$ (which does not occur for $\Delta y = 0.25$ or smaller), and
- for $\epsilon = -0.02$, the ‘blow-up’ happened at an earlier time than that for the

smaller grid sizes shown in Fig.(4-17).

4.5 The Wall State – Bulk State Transition

As mentioned earlier, an interesting and peculiar feature of the traveling-wave wall state is its ‘disappearance’ at some point as the wave number q_x is increased. (This would be for a fixed rotation rate Ω in the case of Rayleigh-Bénard convection, and for fixed λ and μ in the Swift-Hohenberg model.) In this section we explore this transition region numerically for the Swift-Hohenberg model for fixed λ and μ , and propose an amplitude equation to model and explain the transition region and the phenomena observed there.

The parameters picked for the detailed study are $\lambda = -0.6$ and $\mu = -10$. For this set of boundary condition parameters, the wall state disappears at approximately $q_x = 1.314$. Thus we will study the transition region in the $q_x - \epsilon$ plane for $1.20 \leq q_x \leq 1.32$.

In Fig.(4-18) we show the critical ϵ , ϵ_c^W and the critical frequency, ω_c , for the wall state as a function of q_x for $\lambda = -0.6$ and $\mu = -10$. We also show the critical ϵ , ϵ_c^B , for the lowest onset bulk state of the same wave vector q_x . It is worth pointing out that $\epsilon_c^B - \epsilon_c^W$ changes sign at around $q_x = 1.253$, and the bulk state becomes the state with the lower onset ϵ for wave vectors greater than $q_x = 1.253$. This turns out to be important in understanding the transition.

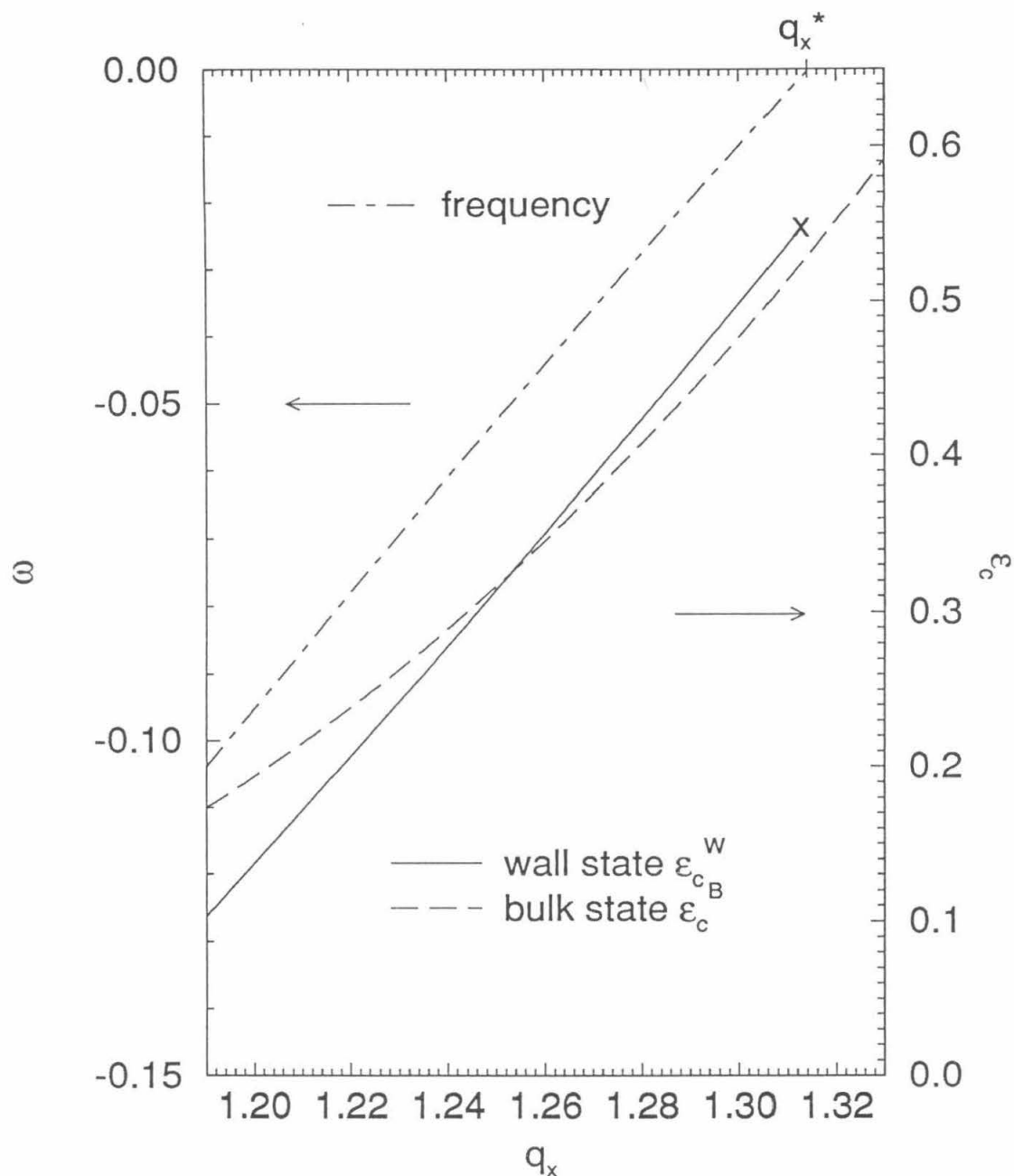


Figure 4-18: Critical ϵ , ϵ_c^W , and critical frequency, ω_c , for the wall state for $\lambda = -0.6$ and $\mu = -10$. The point at which the wall state disappears is indicated by a cross. The wave number at which this occurs is q_x^* . Also shown is the critical ϵ , ϵ_c^B , for the bulk state.

4.5.1 Numerical Study

The transition region was investigated numerically by simulating the Swift-Hohenberg model, equation (4.12), with $g_1 = 1$, and $g_2 = g_3 = 0$. Since we are only interested in, for this study, the wall state – bulk state transition and not the dynamics associated with the Küppers-Lortz instability it is only necessary to include the simplest nonlinear term, $-g_1\psi^3$. The goal of the numerical study is a ‘phase diagram’ of the steady-state solutions of the Swift-Hohenberg equation with q_x and ϵ as the variables. One can then use the phase diagram to understand how the wall state disappears and merges with the bulk state at the nonlinear, steady-state level.

For the phase diagram study, the Swift-Hohenberg equations were iterated in time in an annular geometry with dimensions $l_x = \frac{2\pi}{q_x}$ in the periodic direction (x -direction), and $l_y = 150$ in the direction with ‘rigid’ boundary conditions (y -direction). By restricting l_x to be $\frac{2\pi}{q_x}$, we wish to ensure that only modes with wave number equal to q_x are excited (modes with wave vector nq_x , where n is an integer greater than 1 are strongly damped). However, it turned out to be also necessary to modify the numerical code for this study, and always set the amplitude of the mode with $q_x = 0$ to zero. Otherwise, the state with $q_x = 0$ would grow and end up dominating, thwarting any study of the transition region. This is understandable since the bulk state with $q_x = 0$ (and $q_y = 1$) has a critical onset ϵ of $\epsilon_c = 0$, and the transition region has $\epsilon > 0$.

The grid choice was the same for all of the runs. The number of grid points in the

x -direction was $n_x = 16$, and in the y -direction, the boundary region, where there is a finer grid, was of width 5 and a mesh size of 6 grid points per unit length. For the bulk region of the y -direction the mesh size was 1 grid point per unit length. Thus the total number of grid points in the y -direction is $30 + 140 + 30 + 1 = 200 + 1$.

This choice of grid in the y -direction was checked to be sufficient by increasing the size of the boundary region and/or doubling the grid density and then comparing the results of the simulation on the new ‘higher-grade’ grid with the results on the original chosen grid. This was done for a few (hopefully representative) parameters. The basic dynamics and final steady-state solutions on the different grids were found to be essentially the same for these parameters. There were differences in the actual values which grew with time, but the underlying dynamics did not change.

The phase diagram was arrived at by setting up grids for various q_x ’s, and simulating the Swift-Hohenberg equations for different values of ϵ for each q_x . The final runs were continued until an approximate steady-state solution was arrived at for each ϵ .

4.5.2 The Phase Diagram and the Various States

Apart from the trivial solution ($\psi = 0$), the nonlinear steady-state solutions can be classified into four classes – what we will here call

- the wall state,
- the wall-plus-bulk state,

- the oscillating one-state, and
- the steady one-state.

In Fig.(4-19), we show the phase diagram, with the different types of states observed in the simulations identified.

The Wall State

The ‘wall state’ is easily understood – it exists when one is above the critical onset ϵ , $\epsilon_c^W(q_x)$, for the traveling-wave wall state, and below the critical onset ϵ , $\epsilon_c^B(q_x)$, for the bulk state, and just consists, as its name implies, of the traveling-wave wall state. This picture is confirmed by the parameter values (ϵ, q_x) for which this is the steady-state in the phase diagram.

We will be using various types of pictures and figures to identify and characterize the different classes of states. The wall state for $q_x = 1.2$, and $\epsilon = 0.19$ will be analyzed and presented in this way, even though it is not essential for classification purposes.

Since movies are hard to include in a thesis, we will just present one or more frames from what would be a series of color intensity plots of ψ in time that would go to making up the frames of a ‘movie’ showing the time evolution of ψ . Other types of pictures and figures we will use are

- color intensity plots of ψ as a function of y and t for fixed x ,
- color intensity plots of ψ as a function of x and t for fixed y ,

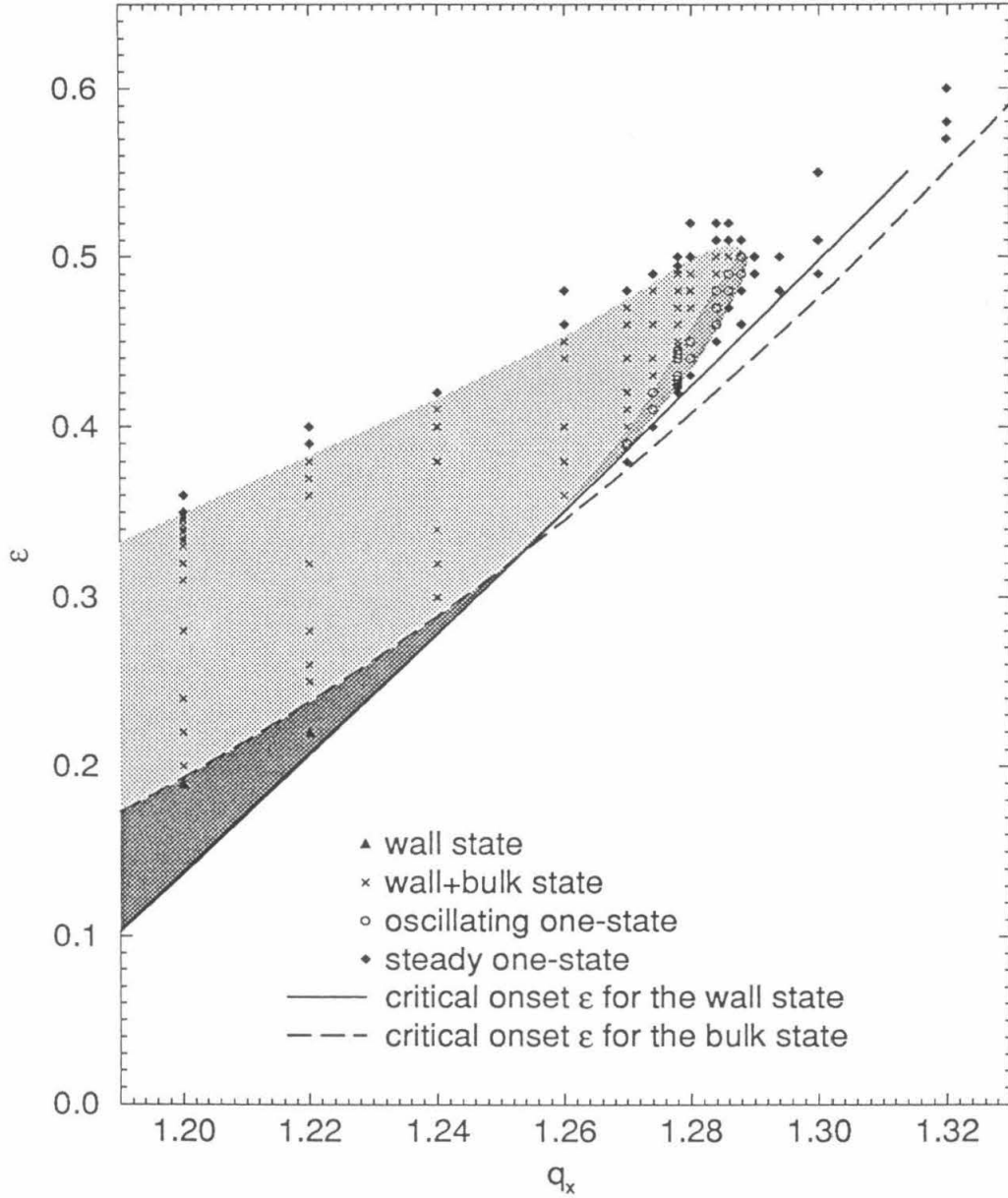


Figure 4-19: The phase diagram for the wall state - bulk state transition region for $\lambda = -0.6$ and $\mu = -10$.

- plots of ψ vs t for fixed (x, y) , and
- the frequency spectra of the ψ vs t plots.

Fig.(4-20(a)) is a frame from a simulation for the parameters $q_x = 1.2$, and $\epsilon = 0.19$. The nonlinear steady-state is a traveling-wave wall state. The traveling-wave at $y = 0$ (top of the picture) is traveling to the left (negative phase velocity) and the traveling-wave at $y = l_y = 150$ (bottom of the picture) is traveling to the right. A plot of ψ vs t for $x = l_x/4$ and $y = 1$ is shown in Fig.(4-21), and the Fourier spectrum (Welch window) for $250 < t \leq 1000$ in Fig.(4-22). Thus the nonlinear steady-state is a pure traveling-wave with frequency $\omega = -0.08$. This is smaller in magnitude than the frequency of the linear wall state - $\omega_c = -0.095$.

Figure (4-20) shows two types of time-slice plots. Fig.(4-20(b)) is a color intensity plot of ψ vs y and t for fixed $x = l_x/4$. Notice that in both boundary regions there is an 'even' cycling through of high and low intensities, indicative of the existence of a pure traveling-wave. And in the bulk, we essentially have a $\psi = 0$ state. Probably the most useful type of plot for identifying the type of steady-state that exists is of the kind shown in Fig.(4-20(c)); it is a color intensity plot of ψ vs x and t for fixed y . In Fig.(4-20(c)), this value of y is 0, *i.e.*, we are looking at the points on the boundary. In this simple illustrative case, we note that the oscillations in ψ , *e.g.*, those of Fig.(4-20(c)), can be seen as arising from a traveling-wave because if ψ is viewed as $\psi = ae^{i\phi} + c.c.$, (a and ϕ real), then

- the constant ϕ contours are clearly the straight lines $\phi = qx - \omega t$ in (x, t) space,

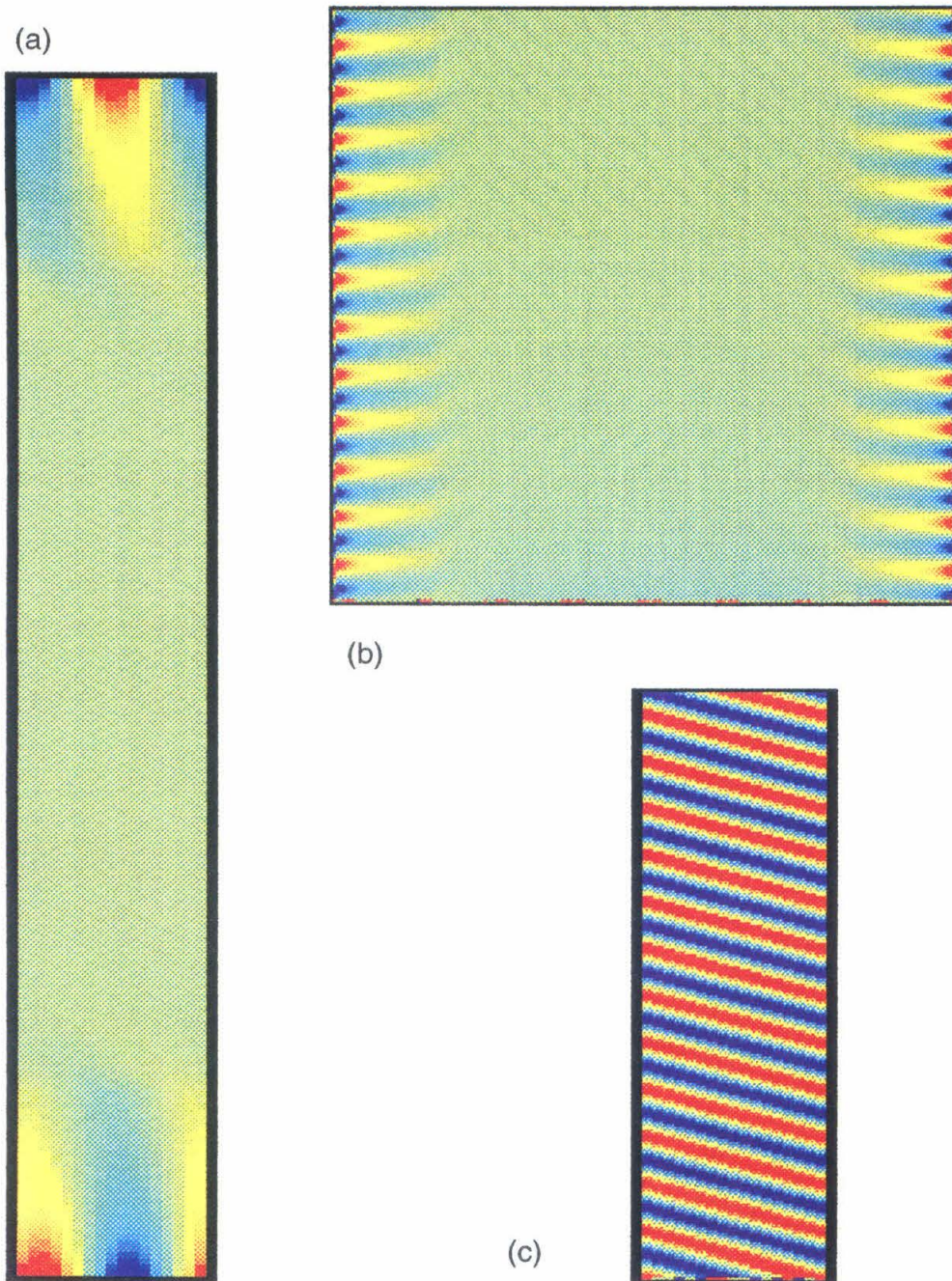


Figure 4-20: Wall state: (a) $\psi(x,y)$ for $t = 1000$, $q_x = 1.2$ and $\epsilon = 0.19$. (x -axis is from left to right, y -axis from top to bottom.) Also note that the boundary regions are to a larger scale ($6\times$). The array density is $30 + 140 + 30$ for lengths of $5 + 140 + 5$. (b) $\psi(y,t)$ for $x = l_x/4$ and $0 \leq t \leq 1000$; the y -axis is from left to right, and the t -axis is from bottom to top. (c) $\psi(x,t)$ for $y = 0$ and $0 \leq t \leq 1000$; the x -axis is from left to right.

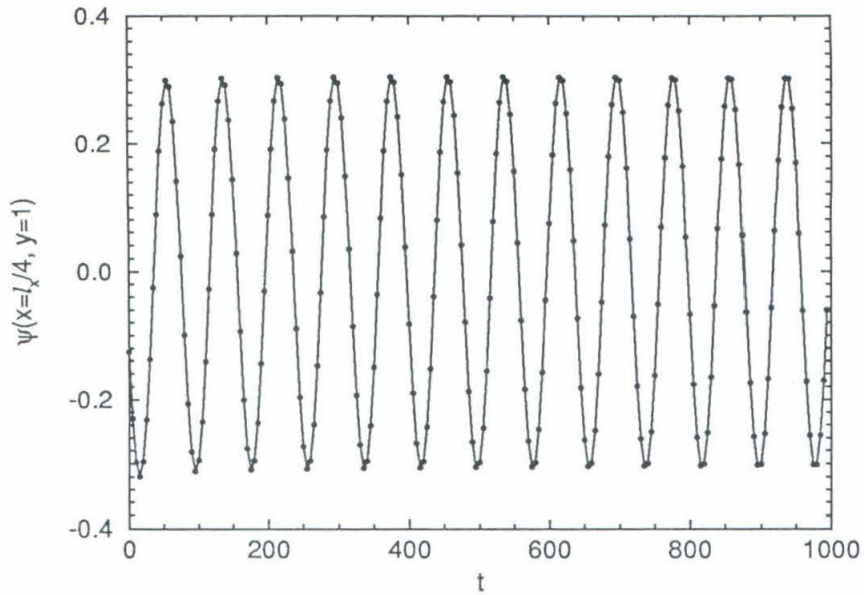


Figure 4-21: $\psi(t)$ for $(x,y) = (l_x/4,1)$ for the wall state in Fig.(4-20).

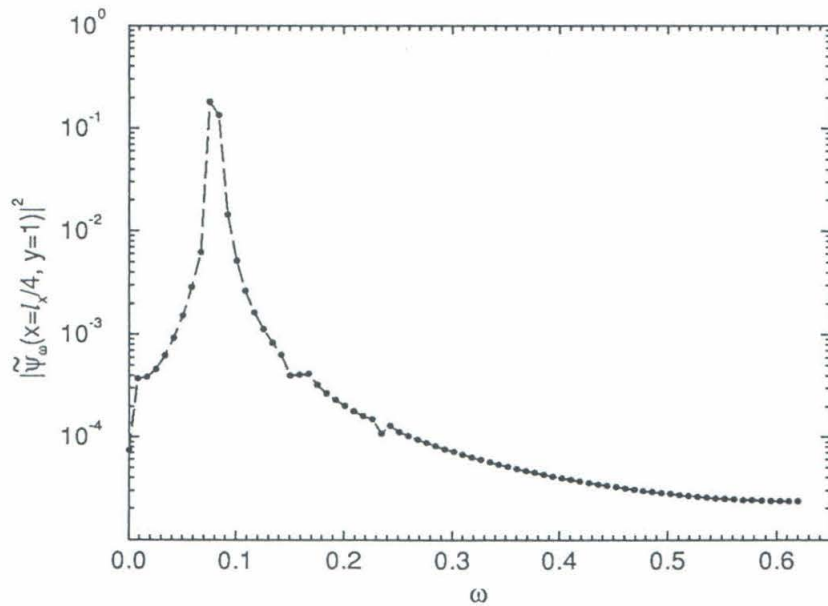


Figure 4-22: Frequency spectrum for Fig.(4-21) for $255 \leq t \leq 1000$.

or in more generalizable terms,

- for all x , the phase ϕ can be seen as a monotonically increasing (or decreasing) function of time when one takes into account the 2π periodicity of the phase variable.

The Wall-plus-Bulk State

At a linear level, the ‘wall-plus-bulk’ state is easy to understand. It is just what one would expect when both the wall and the bulk state are excited. However, the dynamics of the wall-plus-bulk state is more complicated than what would just be the linear superposition of the wall state and the bulk state. We will also here state the criteria for classification as a wall-plus-bulk state – they are

- the existence of a bulk state in the bulk region,
- the existence in the boundary regions of a state which at any point has a monotonically increasing (or decreasing) phase.

In the following, we will use the wall-plus-bulk steady-state at $q_x = 1.24$ and $\epsilon = 0.34$ as an illustration. Fig.(4-23(a)) is a plot of ψ vs (x, y) (at $t = 3000$ for comparison with the next figures). In the central region, there is a steady bulk state, and in the boundary regions, what at first seems to be just a traveling-wave. A more careful analysis however, shows that the value of ψ at the boundaries might be better interpreted as the sum of a steady (but spatially oscillating) value due to the bulk state and an oscillating superposed value due to a traveling-wave. The value of ψ at

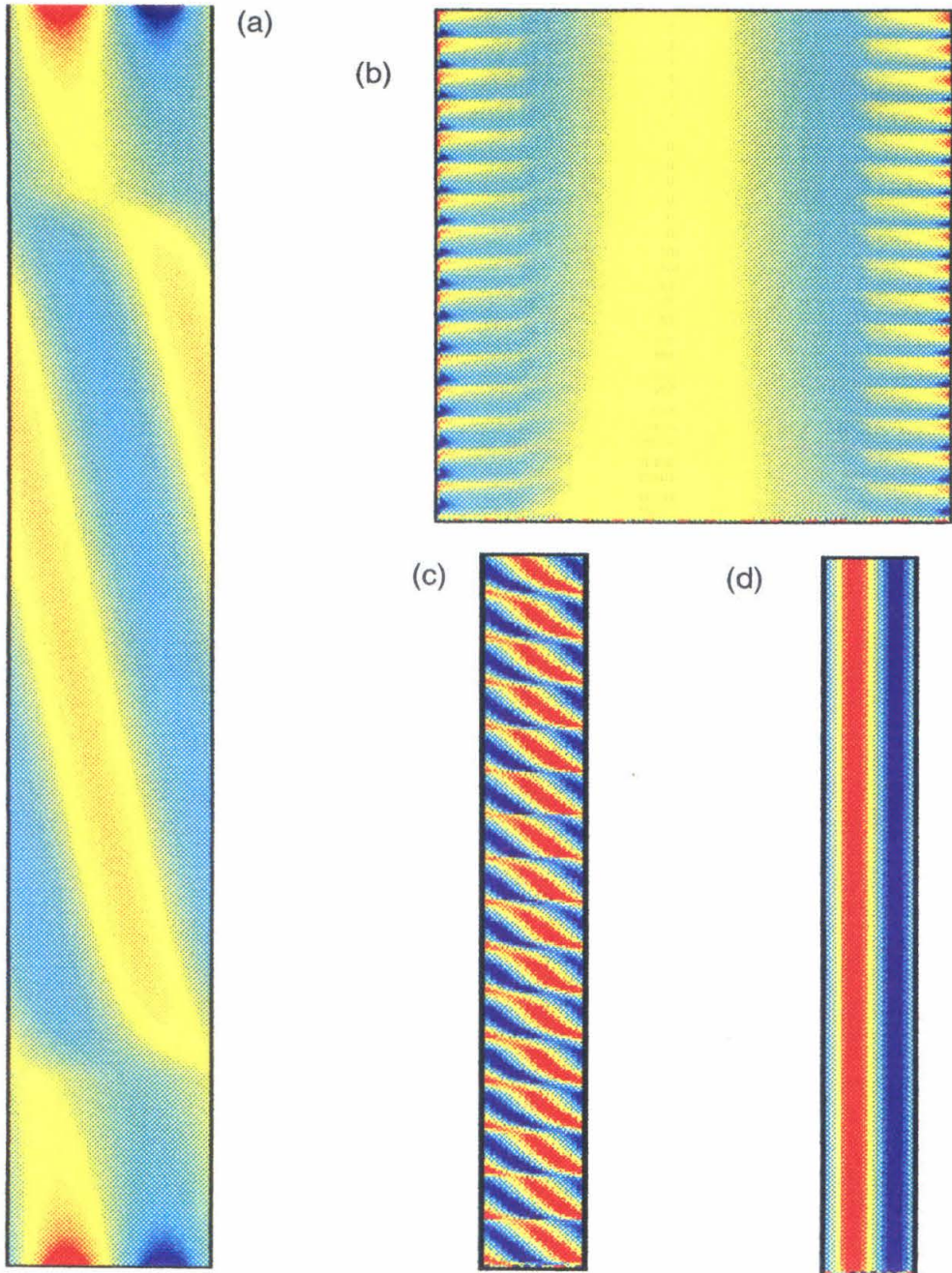


Figure 4-23: Wall-plus-bulk state: $q_x = 1.24$ and $\epsilon = 0.34$. (a) $\psi(x,y)$ for $t = 3000$. (b) $\psi(y,t)$ for $x = l_x/4$ and for $0 \leq t \leq 3000$. (c) $\psi(x,t)$ for $y = 1$ and $0 \leq t \leq 3000$. (d) For $y = 75$.

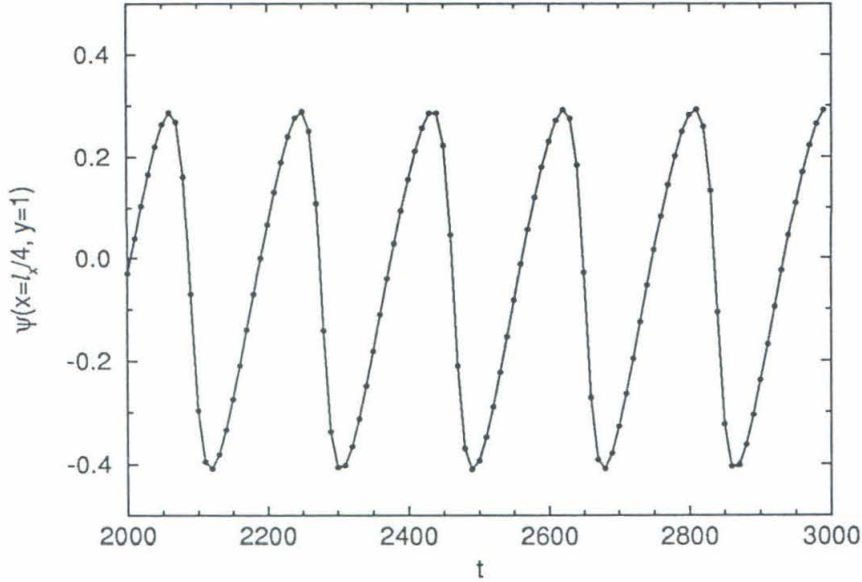


Figure 4-24: $\psi(t)$ for $(x,y) = (l_x/4,1)$ for the wall-plus-bulk state in Fig.(4-23).

$x = l_x/4$ and $y = 1$ is plotted against time in Fig.(4-24). It is clear that ψ is oscillating – unlike for the pure wall state – about a nonzero mean. Furthermore, ψ no longer has a pure harmonic oscillation – the dynamics of the traveling-wave is distorted by the presence of the bulk, with the traveling-wave preferring to ‘sit’ aligned with the bulk state ‘rolls’ as in Fig.(4-23(a)). A spectral analysis of ψ – see Fig.(4-25) – reveals the presence of higher harmonics as one would expect. It is also worth noting that the fundamental frequency here is about $\omega = -0.035$ though the linear frequency is $\omega_c = -0.0609$.

Fig.(4-23(c)) and Fig.(4-23(d)), color intensity plots of ψ vs x and t for $y = 1$ and $y = 75$ respectively, show that we do indeed have a traveling-wave in the boundary region and a steady-state bulk state in the central region. Fig.(4-23(b)), a color

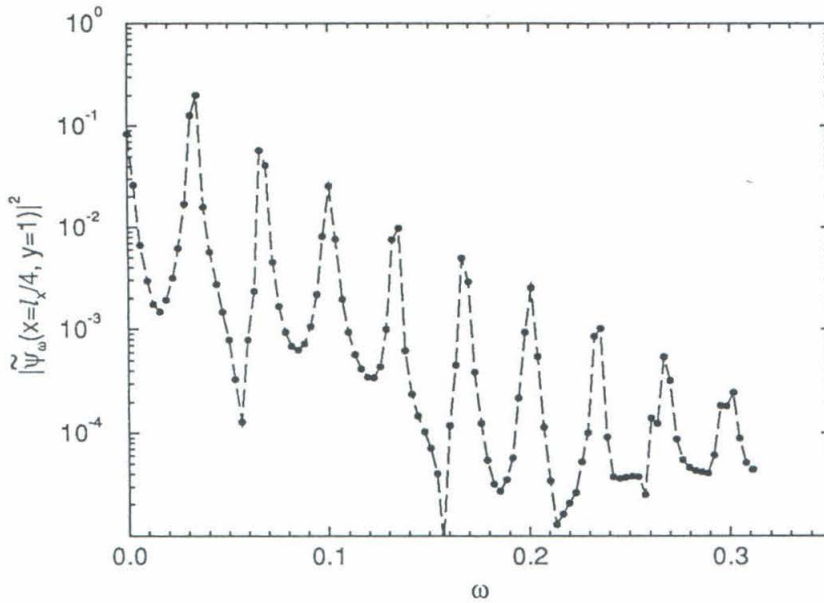


Figure 4-25: Frequency spectrum for $(x,y) = (l_x/4,1)$ and $1000 < t \leq 3000$; for the wall-plus-bulk state in Fig.(4-23).

intensity plot of ψ vs y and t for $x = l_x/4$ indicates the presence of ‘distorted’ traveling-waves (*i.e.*, traveling-waves which are not purely harmonic) in the boundary regions, and a steady bulk state in the bulk.

The Oscillating One-State

The oscillating one-state was an unexpected discovery. Fig.(4-26(a)) provides a ‘snapshot’ of this state for the parameters $\epsilon = 0.44$, $q_x = 1.28$. The difference between this state and the wall-plus-bulk state lies in the boundary region dynamics – there no longer seems to be a traveling-wave, however distorted, in the boundary regions, instead, a spatial wave e^{iq_x} seems to ‘slosh’ jerkily back and forth, as if oscillating at the bottom of a potential well. In the bulk region, there is no difference – there is

just a steady bulk state. The identifying feature of this state is that in contrast to the wall-plus-bulk state, the phase ϕ at any particular point in the boundary region *cannot* be viewed as a monotonically increasing or decreasing function of time. This is most clearly brought out in the color intensity plots of ψ as a function of x and t for fixed y . In Fig.(4-26(c)), we show such a plot for $y = 1$.

In Fig.(4-26(d)), we show the same, but for $y = 75$. This is in the bulk region, and as expected, the state is steady. Fig.(4-26(b)), a plot of ψ as a function of y and t for fixed $x = l_x/4$ also shows that the boundary regions are no longer traveling-waves, but that there however is an oscillation. It also shows that the bulk region is steady.

Fig.(4-27), plots of ψ as a function of t for $x = l_x/4$, $y = 1$ and $x = l_x/4$, $y = 75$, shows an oscillation in time in the boundary region, and a steady-state in the bulk region. From just such a plot however, one cannot distinguish between traveling-wave wall-plus-bulk states and oscillating one-states.

The Steady One-State

The steady one-state is just as its name implies – after its steady-state is reached, there is no dynamics. Fig.(4-29(a)) is a picture of such a state occurring at the parameters $q_x = 1.28$ and $\epsilon = 0.43$. Figures (4-29(b)) and (4-29(c)) are the color intensity plots of ψ as a function of (x, t) for fixed $y = 0$, and as a function of (y, t) for fixed $x = l_x/4$, respectively. And Fig.(4-28) shows the time-evolution of ψ at a boundary point, $(x, y) = (l_x/4, 0)$, and a bulk region point, $(x, y) = (l_x/4, 75)$. All these figures confirm the lack of dynamics in the steady-state.

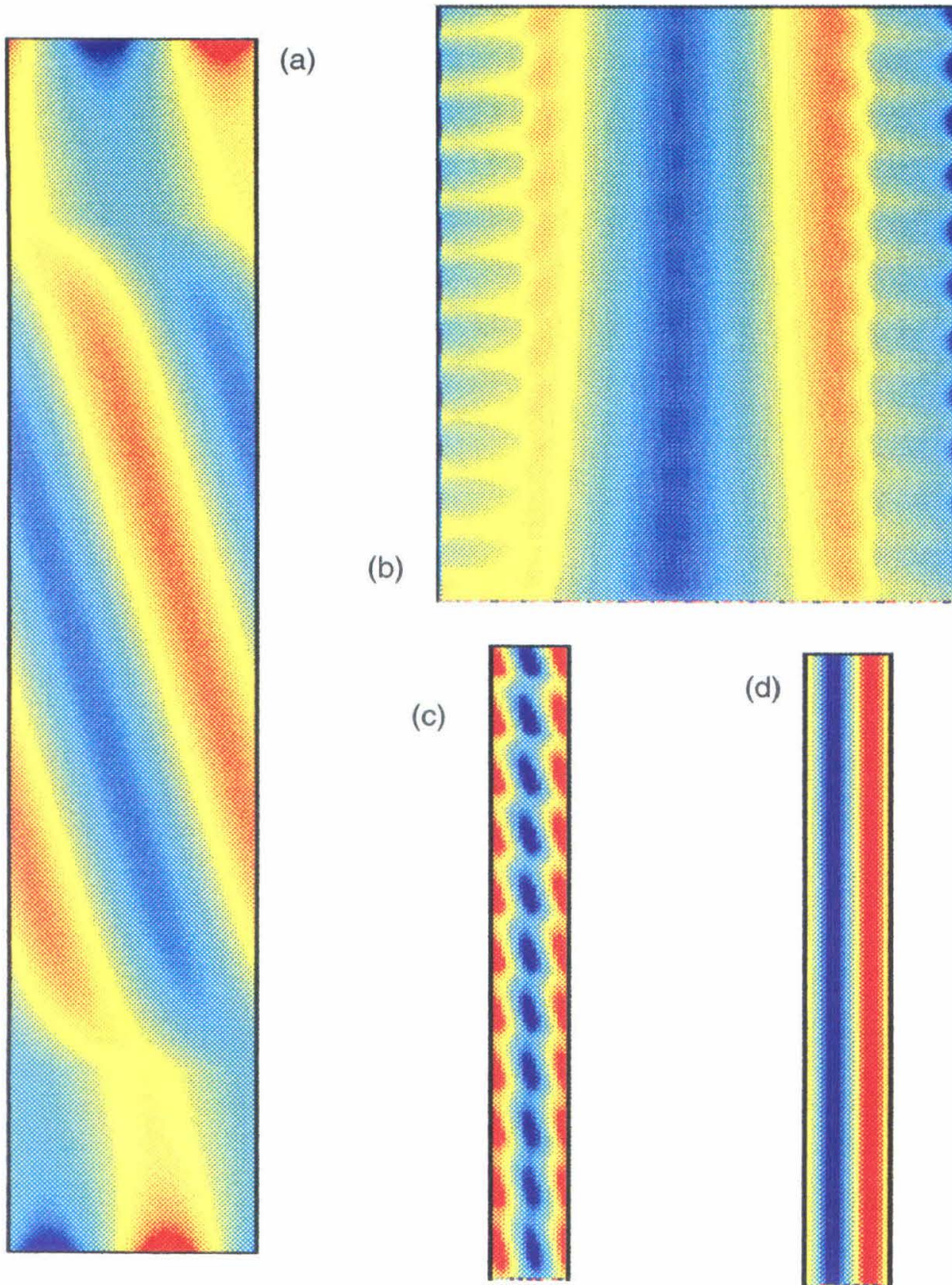


Figure 4-26: Oscillating one-state: $q_x = 1.28$ and $\epsilon = 0.44$. (a) $\psi(x,y)$ for $t = 3000$. (b) $\psi(y,t)$ for $x = l_x/4$ and for $0 \leq t \leq 3000$. (c) $\psi(x,t)$ for $y = 1$ and $0 \leq t \leq 3000$. (d) For $y = 75$.

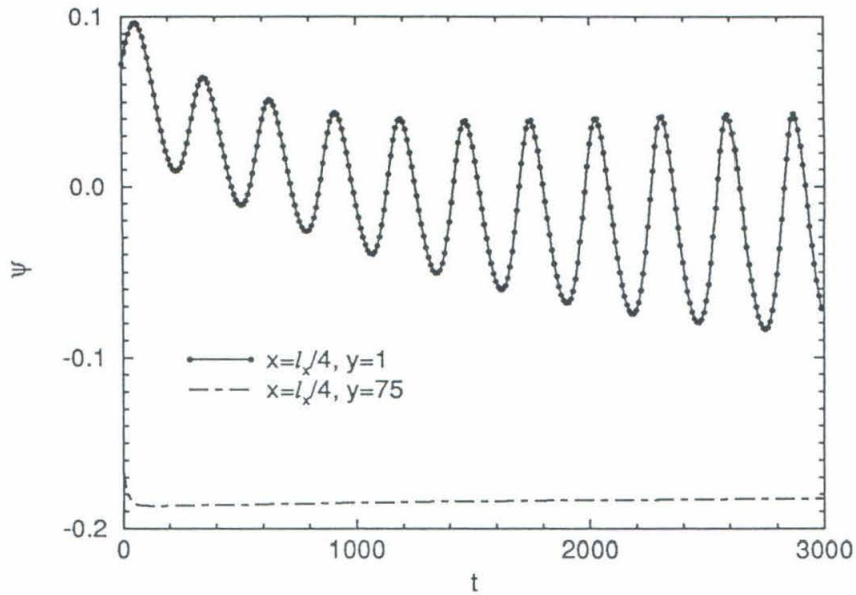


Figure 4-27: $\psi(t)$ for $x = l_x/4$ and $y = 1$ and $y = 75$; for the oscillating one-state in Fig.(4-26).

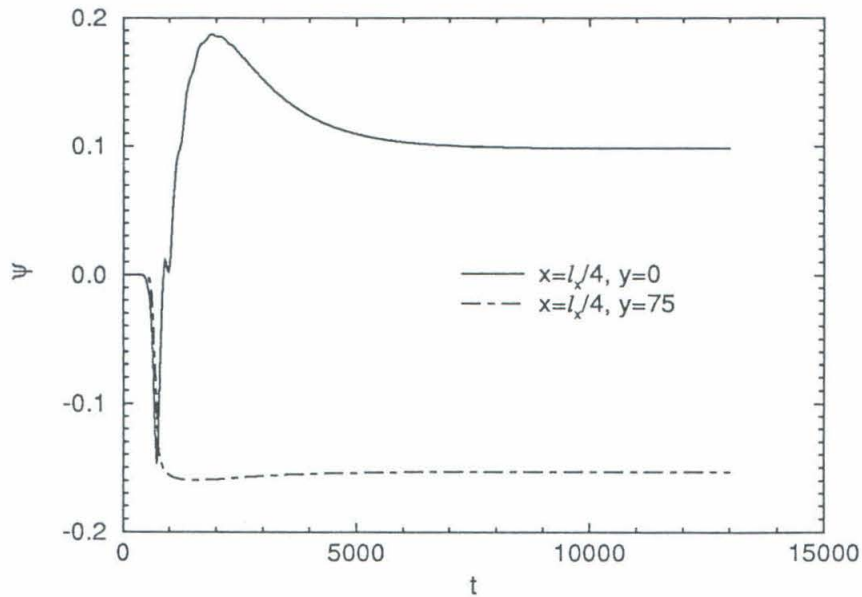


Figure 4-28: $\psi(t)$ for $x = l_x/4$ and $y = 0$ and $y = 75$; for the steady state in Fig.(4-29).

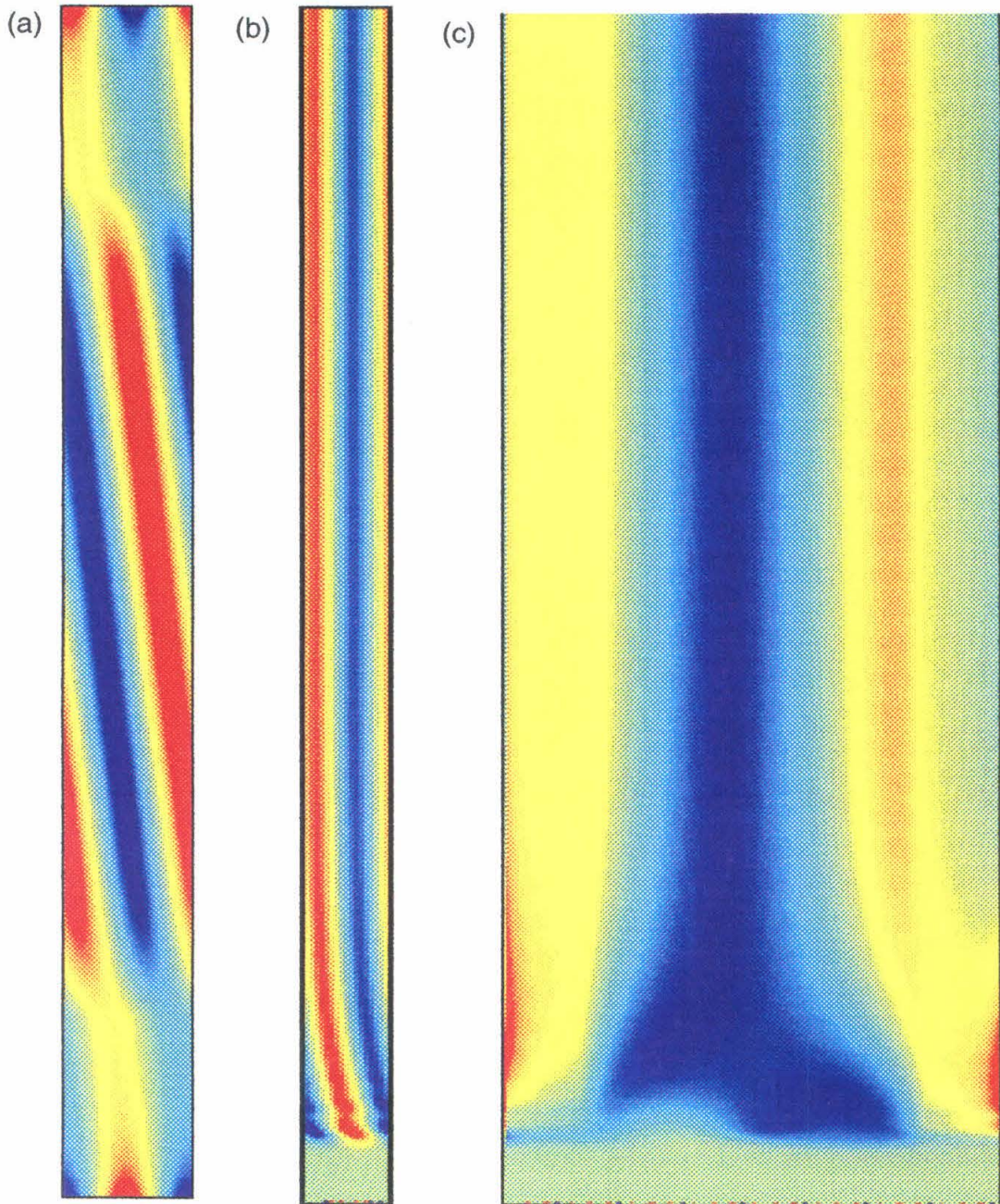


Figure 4-29: Steady one-state: $q_x = 1.28$ and $\epsilon = 0.43$. (a) $\psi(x,y)$ for $t = 13,000$. (b) $\psi(x,t)$ for $y = 0$ and for $0 \leq t \leq 13,000$. (c) $\psi(y,t)$ for $x = l_x/4$ and for $0 \leq t \leq 13,000$.

4.5.3 A Detailed Study of the Nonlinear Steady-State Frequency at $q_x = 1.2$

The nonlinear frequency of the wall and the wall-plus-bulk state decreases as ϵ increases, and culminates in the transition from wall-plus-bulk state to steady one-state, at which the frequency goes to zero. In Fig.(4-30) we show this change for $q_x = 1.2$. Also shown in the figure is the critical linear onset frequency of the wall state, ϵ_c^W . The frequencies in Fig.(4-30) were calculated using two methods on essentially the same data.

The equations were evolved in time for each ϵ until it was judged that the system was ‘reasonably’ close to its steady-state. The values of $\psi(x = l_x/4, y = 1, t)$ for when the system is ‘sufficiently close’ to its steady-state were then used to calculate its nonlinear frequency – both by taking a Fourier transform (Welch window) of the relevant segment of data, and by calculating an average period using several periods, usually over a shorter length of data which is at the end (and hence is supposedly close to the final steady-state). In Fig.(4-31) and Fig.(4-32) we show an example of the time-dependence of $\psi(x = l_x/4, y = 1)$ for $\epsilon = 0.3483$, and part of its Fourier spectrum. Note the rapid drops in ψ from its maximum value to its minimum value followed by a gradual and slowing rise back to its maximum value.

In Fig.(4-33) we show the frequency near the bifurcation point, where the wall-plus-bulk state bifurcates to the steady one-state. In this figure we also show the

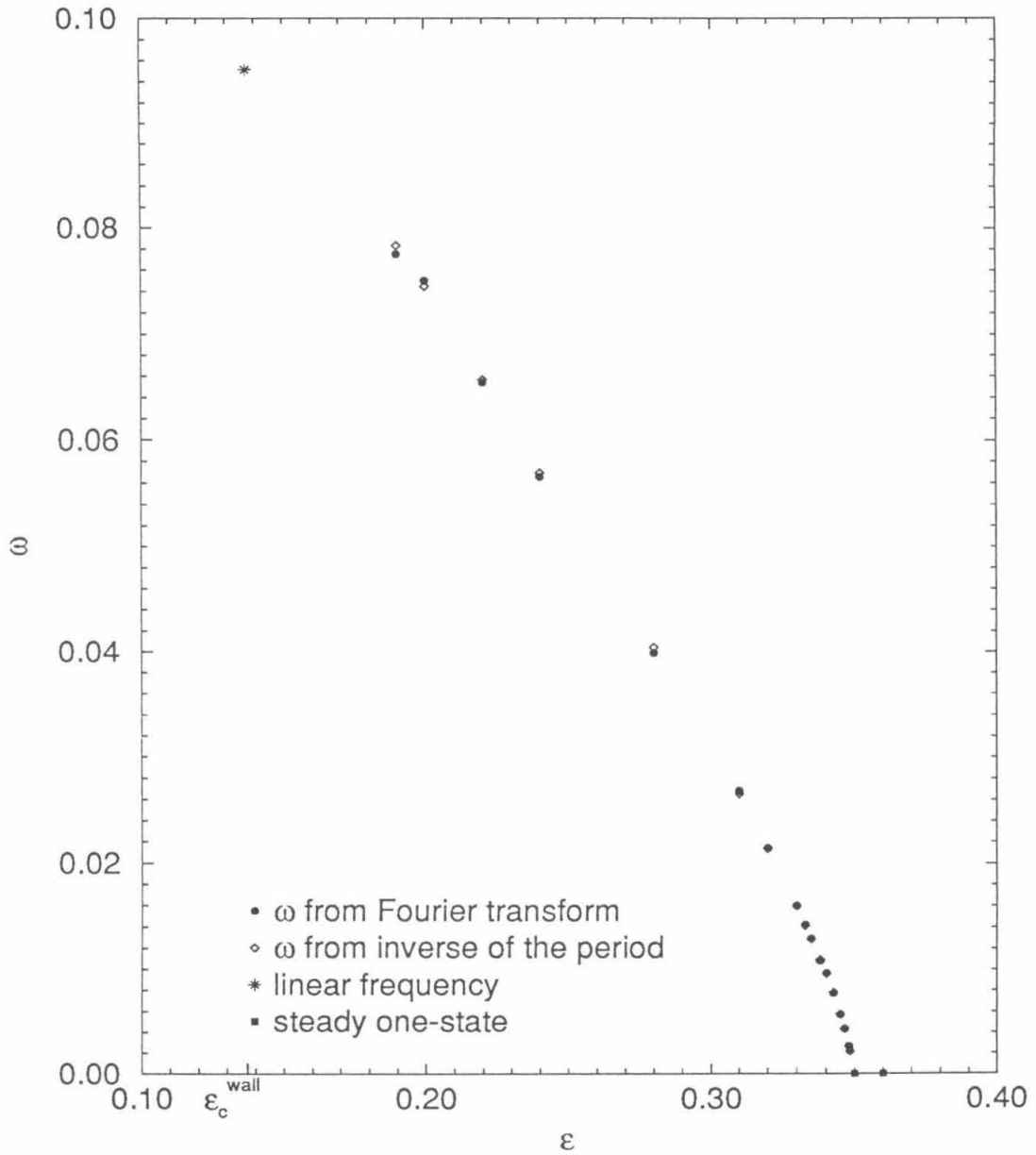


Figure 4-30: Nonlinear frequency ω as a function of ϵ at $q_x = 1.2$.

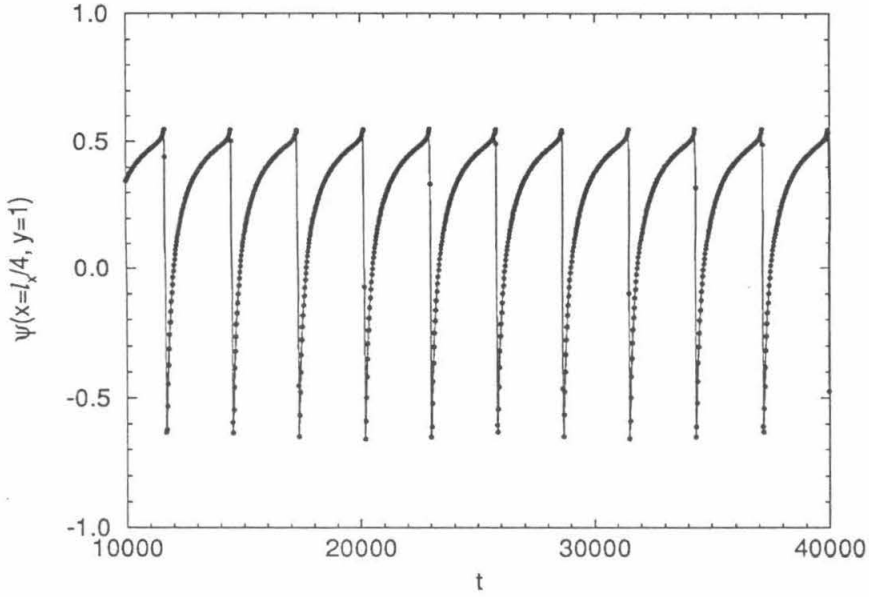


Figure 4-31: $\psi(t)$ for $(x, y) = (l_x/4, 1)$ at $q_x = 1.2$ and $\epsilon = 0.3483$.

three parameter fit to the data of the form

$$\omega = \eta_1(\epsilon_0 - \epsilon)^{1/2} + \eta_2(\epsilon_0 - \epsilon).$$

For both sets of frequency data, we find

$$\epsilon_0 = 0.349,$$

$$\eta_1 = 0.068,$$

$$\eta_2 = 0.34.$$

We expect the frequency to approach zero at the bifurcation point as $\omega \sim (\epsilon_0 - \epsilon)^{1/2}$, because if $\dot{\phi} = \dot{\phi}(\phi)$ has a minimum value $\dot{\phi}_{min}$, at some value $\phi = \phi_0$ (as it must if $\dot{\phi}$ is a 2π -periodic function of ϕ), then the bifurcation point corresponds to the transition from $\dot{\phi}_{min} > 0$ to $\dot{\phi}_{min} < 0$ at $\dot{\phi}_{min} = 0$. When $\dot{\phi}_{min} > 0$, ϕ just cycles

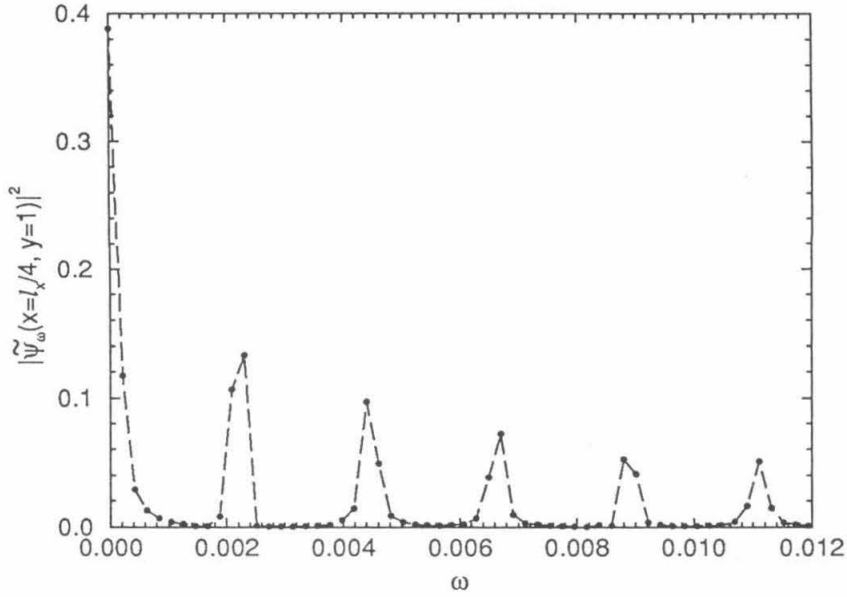


Figure 4-32: Part of the frequency spectrum for Fig.(4-31).

through 2π , but when $\dot{\phi}_{min} < 0$ there is a stable fixed point at one of the values of ϕ for which $\dot{\phi}_{min} = 0$. When $\dot{\phi}_{min} > 0$ is small, the period is dominated by the time spent near $\phi = \phi_0$ where $\dot{\phi}_{min}$ is small. We also expect in general that $\dot{\phi}_{min}$ goes through zero linearly as a function of $(\epsilon_0 - \epsilon) = \Delta\epsilon$, *i.e.*, near the bifurcation point, we can write

$$\dot{\phi} = b_0(\Delta\epsilon) + b_1(\phi - \phi_0)^2, \quad b_i > 0.$$

Thus we can approximate the integral for the period as

$$T = \int dt \approx \int_{-\pi}^{\pi} \frac{d\phi}{b_0(\Delta\epsilon) + b_1\phi^2} \approx \pi(b_0b_1)^{-1/2} \cdot (\Delta\epsilon)^{-1/2}.$$

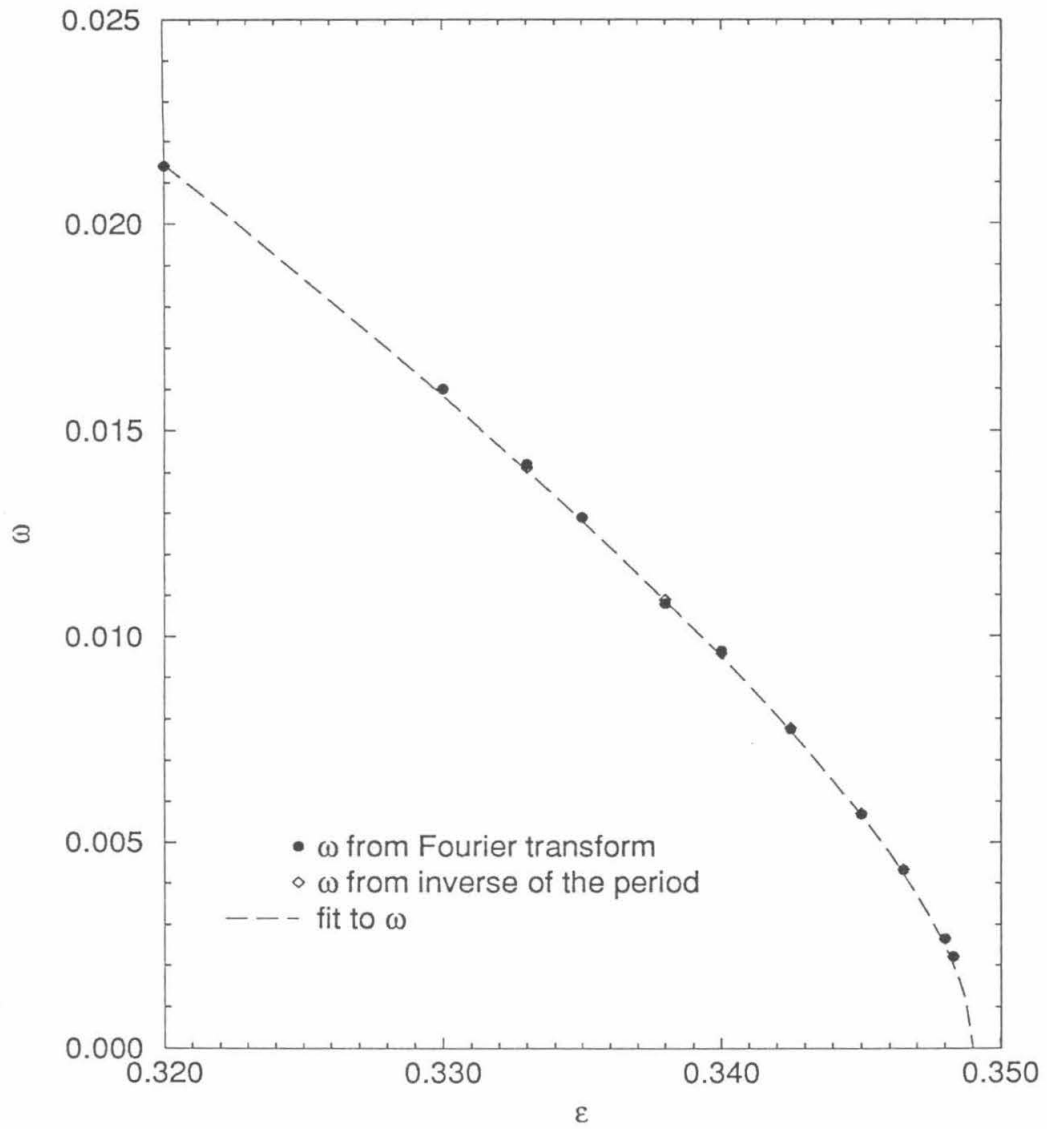


Figure 4-33: Fit to the data of Fig.(4-30) near the bifurcation point.

4.5.4 A Study of the Nonlinear Steady-State Frequency at

$$q_x = 1.278$$

For $q_x = 1.278$, a study of the ϵ -dependence of the frequency was undertaken in order to understand the oscillating one-state to wall-plus-bulk state transition. Unlike the frequency study for $q_x = 1.20$, the frequencies here were not as carefully calculated due to time and disk space constraints, and also for the reason that it turned out not to be necessary for this transition.

In Fig.(4-34) the type of nonlinear steady-state and its frequency is shown for various values of ϵ . The most striking observation is that the value of ω is a smooth function of ϵ as one goes through the transition.

Another important observation (not only here, but also for other values of q_x) is that near the transition, it becomes very hard to distinguish between an oscillating one-state and a wall-plus-bulk state for the reason that periodically the whole boundary region becomes near zero in amplitude. This makes it very hard to know whether the phase ϕ is monotonically increasing (decreasing) or not. For example, see Fig.(4-35(a)) and Fig.(4-35(b)). One would thus also expect the transition point to correspond to the value of ϵ for which the amplitude of the boundary region does actually periodically go through zero, and for which times the phase is therefore undefined.

The transition from oscillating one-state to steady one-state was not studied in detail, as the time scales involved in the approach to steady-state were 'large' com-

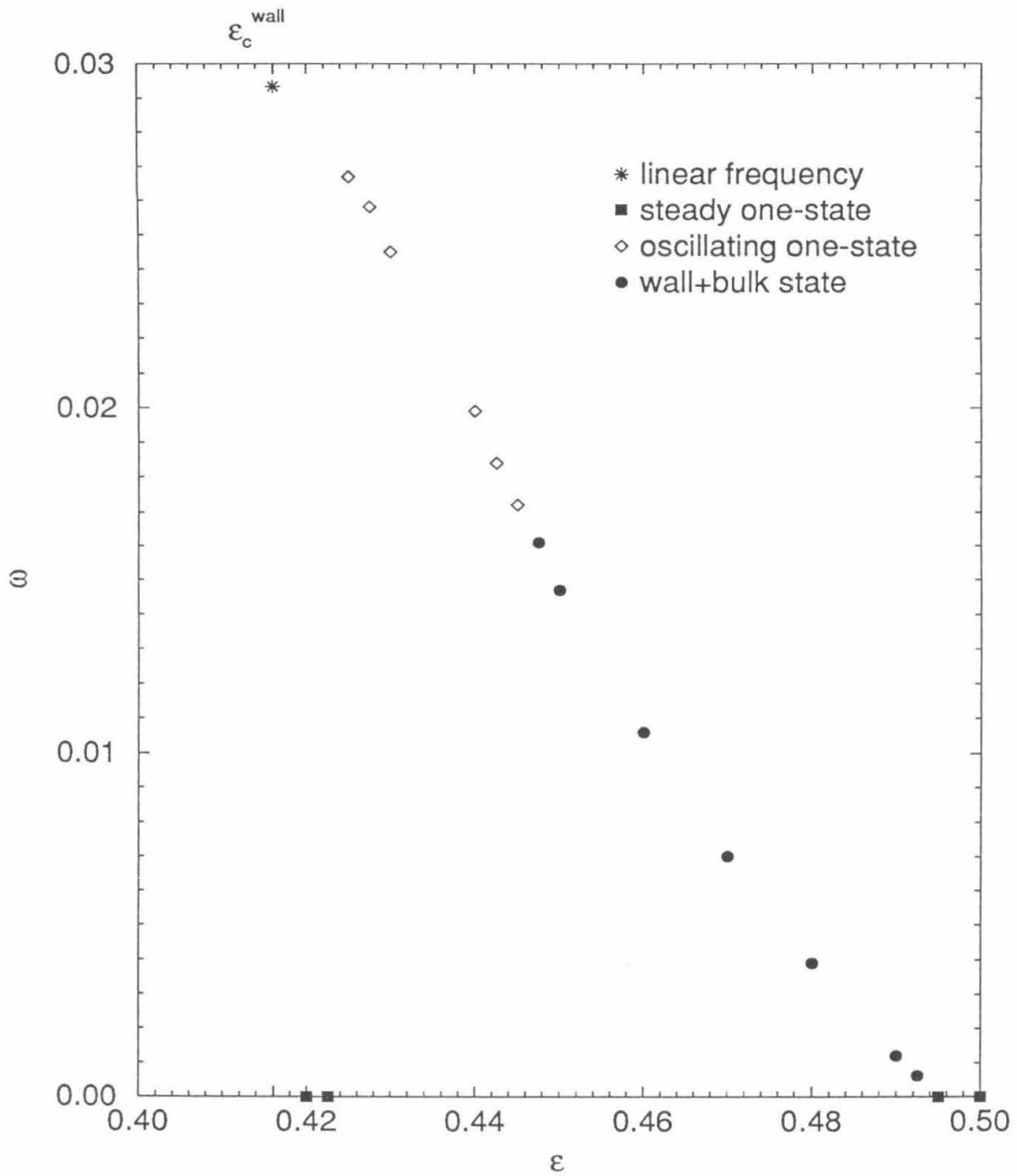


Figure 4-34: Nonlinear frequency ω and the type of steady-state as a function of ϵ at $q_x = 1.278$.

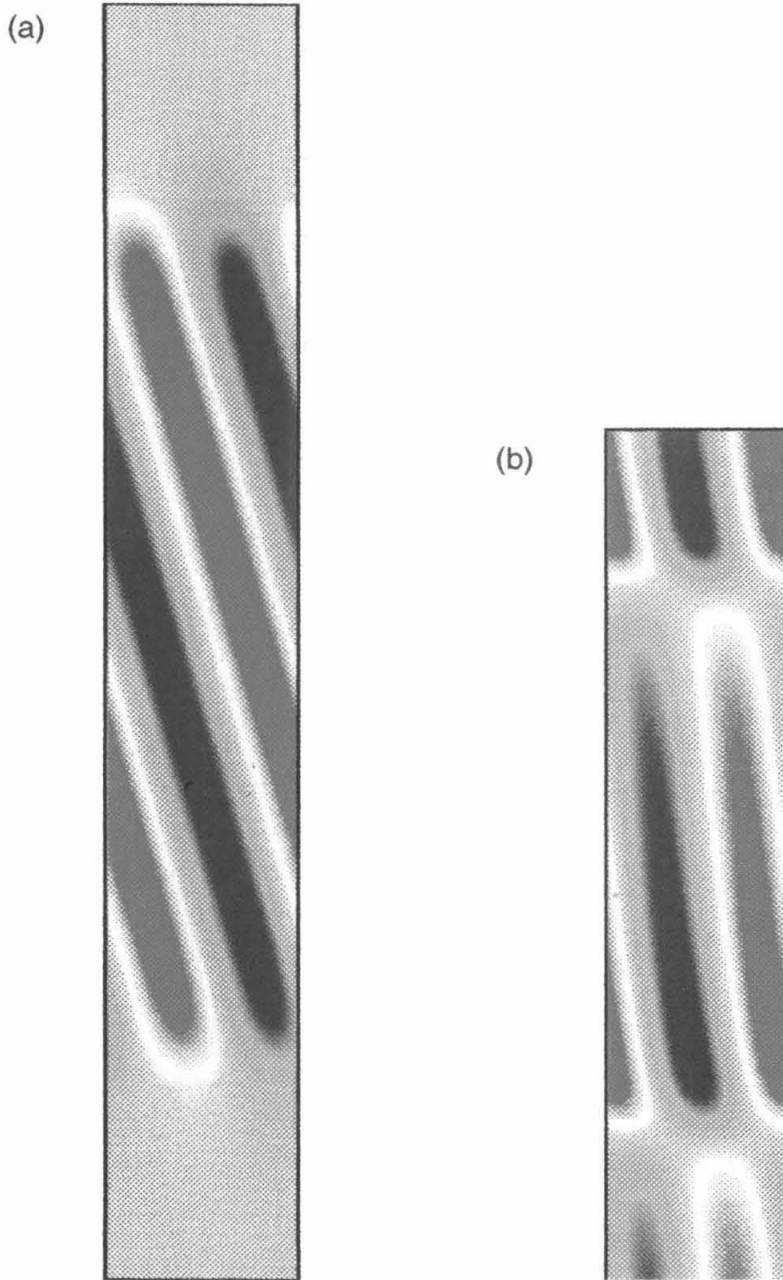


Figure 4-35: (a) $\psi(x, y)$ at a time when the whole boundary region becomes near zero in amplitude. Here $q_x = 1.278, \epsilon = 0.445$. (b) $\psi(x, t)$ at $y = 0$. $\Delta T = 600$ for this sequence. (This is actually an oscillating one-state.)

pared with the period. However, as will be explained later, it is expected that the frequency variation there is just a linear function, $\omega = \omega_0 + \eta(\epsilon - \epsilon_0)$, where ω_0 and ϵ_0 are the values of the frequency and ϵ at the transition point respectively (and η is some negative constant). Coupled to this is the observation that if it were not for the occurrence of the steady one-state, the frequency looks as if it would just continuously change into the linear frequency as ϵ is decreased.

4.5.5 An Amplitude Equation to Describe the Dynamics

In this section, we derive an amplitude equation to describe the dynamics in the transition region. This amplitude equation is an expansion about the state $e^{iq_{xc}x} e^{iq_{yc}y}$, which is the bulk part of the wall state at the point (q_{xc}, ϵ_c) where the critical onset wall state disappears and its frequency goes to zero. This expansion will not be rigorous in the sense of the ‘multiple-scales approach’ with a well-controlled expansion parameter, but will nonetheless provide useful insights into the dynamics of the transition region.

Let us write the linear wall state at the point it disappears as $e^{iq_{xc}x} (\tilde{\psi}_1 e^{iq_{yc}y} + \tilde{\psi}_2 e^{-\kappa y})$ where q_{yc} and $\kappa > 0$ are both real. For fixed q_x , in the neighborhood of this point, *i.e.*, $\Delta q_x = q_x - q_{xc}$ and $\Delta \epsilon = \epsilon - \epsilon_c$ ‘small’, we wish to treat the mode $e^{i(q_{xc} + \Delta q_x)x} e^{iq_{yc}y}$ as the one which has the ‘slowly’ varying envelope amplitude $A(y, t)$ describing its dynamics on large length scales into the distance, and $e^{i(q_{xc} + \Delta q_x)x} e^{-\kappa y}$ as the fast-varying mode localized to the boundary which will be ‘eliminated’ to obtain a boundary condition on A ; a more rigorous exposition of this method can be found,

for example, in [30]. Thus the variable ψ will be written as (for fixed $q_x = q_{xc} + \Delta q_x$)

$$\psi(x, y, t) = e^{iq_{xc}x} e^{i\Delta q_{xc}x} (A(Y, t) e^{iq_{yc}y} + C(t) e^{-\kappa y}) + c.c., \quad (4.55)$$

where here “ $Y = y$ ”, but Y will be treated as the ‘slow’ variable incorporating the slow variations of the envelope amplitude A .

The linear part of the amplitude equation for $A(Y, t)$ can, as usual, be deduced from the dispersion relation, $\Gamma = \epsilon - (q_x^2 + q_y^2 - 1)^2$. Here, we will expand the dispersion relation about the state $e^{iq_{xc}x} e^{iq_{yc}y}$ (which satisfies the relation $0 = \epsilon_c - (q_{xc}^2 + q_{yc}^2 - 1)^2$) to first-order in Δq_x and second-order in $Q = q_y - q_{yc}$. Since we expect an asymmetry $\Delta q_x \leftrightarrow -\Delta q_x$, just keeping the terms to $O(\Delta q_x)$ should retain the relevant phenomena, and we will keep terms of $O(Q^2)$ since we want an amplitude equation that is second-order in $\frac{\partial}{\partial Y}$. With this expansion method, we find the linear part of the amplitude equation for A to be

$$\frac{\partial A}{\partial t} = \tilde{\epsilon}(\Delta q_x) A + i\tilde{\alpha}(\Delta q_x) \frac{\partial A}{\partial Y} + \tilde{\beta}(\Delta q_x) \frac{\partial^2 A}{\partial Y^2}, \quad (4.56)$$

where

$$\begin{aligned} \tilde{\epsilon}(\Delta q_x) &= \Delta\epsilon - 4\sqrt{\epsilon_c} q_{xc} \Delta q_x, \\ \tilde{\alpha}(\Delta q_x) &= 4q_{yc}(\sqrt{\epsilon_c} + 2q_{xc}(\Delta q_x)), \\ \text{and } \tilde{\beta}(\Delta q_x) &= 2\left((\sqrt{\epsilon_c} + 2q_{yc}^2) + 2q_{xc}(\Delta q_x)\right). \end{aligned}$$

We now seek the boundary condition on A . Expanding (4.55) for $\frac{\partial \tilde{\psi}}{\partial y}$ and $\frac{\partial^2 \tilde{\psi}}{\partial y^2}$ where $\psi(x, y, t) = e^{i(q_{xc} + \Delta q_x)x} \tilde{\psi}(y, t)$, we find

$$\frac{\partial \tilde{\psi}}{\partial y} = \left(\frac{\partial A}{\partial Y} + iq_{yc} A \right) e^{iq_{yc}y} + C(-\kappa) e^{-\kappa y}, \quad (4.57)$$

$$\frac{\partial^2 \tilde{\psi}}{\partial y^2} = \left(\frac{\partial^2 A}{\partial Y^2} + 2iq_{yc} \frac{\partial A}{\partial Y} - q_{yc}^2 A \right) e^{iq_{yc}y} + C \kappa^2 e^{-\kappa y}. \quad (4.58)$$

Substituting (4.57) and (4.58) into the boundary conditions on ψ , (4.3) and (4.4), leads to

$$A' + (iq_{yc} - \lambda)A = (\kappa + \lambda)C \quad (4.59)$$

$$\begin{aligned} & \mu i(q_{xc} + \Delta q_x)A'' - 2\mu q_{yc}(q_{xc} + \Delta q_x)A' + \\ & [\mu i(q_{xc} + \Delta q_x)(q_0^2 - (q_{xc} + \Delta q_x)^2 - q_{yc}^2) + 1]A \\ & = -[\mu i(q_{xc} + \Delta q_x)(q_0^2 - (q_{xc} + \Delta q_x)^2 + \kappa^2) + 1]C \end{aligned} \quad (4.60)$$

where $A'' = \frac{\partial^2 A}{\partial Y^2}|_{Y=0}$, $A' = \frac{\partial A}{\partial Y}|_{Y=0}$ and $A = A|_{Y=0}$. We now can use (4.59) to eliminate C in (4.60) and thus find that the boundary condition on A at $Y = 0$ is

$$i\eta_2(\Delta q_x)A'' + \eta_1(\Delta q_x)A' + i\eta_0(\Delta q_x)A = 0, \quad (4.61)$$

$$\begin{aligned} \text{where } \eta_2(\Delta q_x) &= \mu(q_{xc} + \Delta q_x), \\ \eta_1(\Delta q_x) &= \frac{\mu i(q_{xc}\sqrt{\epsilon_c} + (\sqrt{\epsilon_c} - 2q_{xc}^2)(\Delta q_x)) + 1}{\kappa + \lambda} - 2\mu q_{yc}(q_{xc} + \Delta q_x), \\ \text{and } \eta_0(\Delta q_x) &= \left[\frac{iq_{yc} - \lambda}{\kappa + \lambda} (\sqrt{\epsilon_c} - 2q_{xc}^2) - (\sqrt{\epsilon_c} + 2q_{xc}^2) \right] \cdot \mu(\Delta q_x). \end{aligned}$$

4.5.6 Solutions to the Amplitude Equation

For the mode $A \sim e^{iQY} e^{\Gamma t}$, the dispersion relation of the amplitude equation (4.56) gives

$$\Gamma = \tilde{\epsilon} - \tilde{\alpha}Q - \tilde{\beta}Q^2, \quad (4.62)$$

and thus there are two wave vector solutions for each eigenvalue Γ , *viz*

$$Q_{\pm} = \frac{-\tilde{\alpha} \pm \sqrt{\tilde{\alpha}^2 + 4\tilde{\beta}(\tilde{\epsilon} - \Gamma)}}{2\tilde{\beta}}. \quad (4.63)$$

The discriminant $D = \tilde{\alpha}^2 + 4\tilde{\beta}(\tilde{\epsilon} - \Gamma)$ in (4.63) is

$$D = 8[2q_{yc}^2(\epsilon_c + (\Delta\epsilon - \Gamma)) + \sqrt{\epsilon_c}(\Delta\epsilon - \Gamma)] + 16q_{xc}[(\Delta\epsilon - \Gamma) - 2\epsilon_c](\Delta q_x). \quad (4.64)$$

In some sense we have been assuming q_{yc} is ‘small’ (even though in taking out the ‘rapid’ variation $e^{iq_{yc}y}$ we were assuming q_{yc} is $O(1)$ or ‘large!’), because the unstable band of y -wave vectors, captured in the term Q (or $\frac{\partial}{\partial Y}$ of the amplitude equation), is of width $2q_{yc}$ when $\epsilon = \epsilon_c$ and $q_x = q_{xc}$. (This stems from the band of unstable real y -wave vectors being $-q_{yc} \leq q_y \leq q_{yc}$ when $\epsilon = \epsilon_c$ and $q_x = q_{xc}$.) Now we can seek the zero growth rate ($\Gamma = 0$ and $\Gamma = -i\omega$) solutions of the amplitude equation (4.56) and its boundary condition at $Y = 0$, (4.61), since the unstable modes can be captured in ‘slow modulations’ of this mode (in some sense another amplitude equation envelope of even slower variation will modulate this $\Gamma = 0$ mode).

The value of the discriminant D in (4.64) determines the type of solution or mode we are considering. If $D > 0$, then Q_+ and Q_- are real, and represent bulk solutions. We can thus write a bulk solution mode as

$$A_B(Y, t) = A_+ e^{iQ_+ Y} + A_- e^{iQ_- Y}, \quad (4.65)$$

where A_+/A_- is determined by the boundary condition (4.61) to be

$$\frac{A_+}{A_-} = -\frac{Q_-^2 \eta_2(\Delta q_x) - Q_- \eta_1(\Delta q_x) - \eta_0(\Delta q_x)}{Q_+^2 \eta_2(\Delta q_x) - Q_+ \eta_1(\Delta q_x) - \eta_0(\Delta q_x)}. \quad (4.66)$$

Notice that $\tilde{\alpha}(\Delta q_x) < 0$, (for $q_{yc} < 0$ in the cases $\mu < 0$), thus Q_- is ‘small’, and $\frac{A_+}{A_-}$ is small, corresponding to the original mode q_{yc} being dominant. Furthermore, when $\Delta q_x = 0$ and $\Delta\epsilon = 0$, $Q_- = 0$, and thus $A_+/A_- = 0$, reproducing the mode about which we are expanding. However, the ‘best’ value, if any, of $\Delta\epsilon$ for which we should seek the $\Gamma = 0$ mode is not clear.

We can also look for zero growth solutions with an oscillating time-dependence $e^{-i\omega t}$. In this case, the discriminant D is complex and so are Q_+ and Q_- . Even though they are not complex conjugates of one another, their imaginary parts are the negatives of each other, and only one of them, clearly Q_- by continuation from the point of expansion, can be a valid solution with $Im(Q_-) > 0$. Therefore we seek a mode of the form $A_W(Y, t) = A_- e^{iQ_- Y} e^{-i\omega t}$ where ω , Q_- and $\Delta\epsilon$ are determined by the boundary condition (4.61). It seems reasonable to expect the solution to have $\omega \sim \Delta q_x$ and $\Delta\epsilon \sim \Delta q_x$; therefore we expand Q_- and the boundary condition to $O(\Delta q_x)$ in order to seek a lowest order solution. Indeed, this will be found to be self-consistent. Expanding, we find

$$Q_- = \frac{1}{4q_{yc}} \left[\frac{\Delta\epsilon}{\sqrt{\epsilon_c}} - 4q_{xc}(\Delta q_x) + i \frac{\omega}{\sqrt{\epsilon_c}} \right], \quad (4.67)$$

(provided $\omega < 0$ for $q_{yc} < 0$). Separating the real and imaginary parts of the boundary condition (4.61) gives the boundary matrix equations:

$$\begin{pmatrix} a & -b \\ b & a \end{pmatrix} \begin{pmatrix} \frac{\Delta\epsilon}{\sqrt{\epsilon_c}} \\ \frac{\omega}{\sqrt{\epsilon_c}} \end{pmatrix} = \begin{pmatrix} c_1 \\ c_2 \end{pmatrix} (\Delta q_x) \quad (4.68)$$

where

$$\begin{aligned}
 a &= \frac{1}{4q_{yc}} \frac{\mu q_{xc} \sqrt{\epsilon_c} + 1}{\kappa + \lambda} \\
 b &= \frac{\mu q_{xc}}{2} \\
 \text{and } c_1 &= \frac{1}{\kappa + \lambda} \left[\frac{q_{xc}}{q_{yc}} (\mu q_{xc} \sqrt{\epsilon_c} + 1) - \mu q_{yc} (\sqrt{\epsilon_c} - 2q_{xc}^2) \right] \\
 c_2 &= -\mu \left[\sqrt{\epsilon_c} + \frac{\lambda}{\kappa + \lambda} (\sqrt{\epsilon_c} - 2q_{xc}^2) \right].
 \end{aligned}$$

Thus the critical onset wall state has $\Delta\epsilon$ and ω given by

$$\begin{pmatrix} \frac{\Delta\epsilon}{\sqrt{\epsilon_c}} \\ \frac{\omega}{\sqrt{\epsilon_c}} \end{pmatrix} = \frac{1}{a^2 + b^2} \cdot \begin{pmatrix} ac_1 + bc_2 \\ ac_2 - bc_1 \end{pmatrix} \cdot (\Delta q_x). \quad (4.69)$$

As expected, $\Delta\epsilon \sim \Delta q_x$ and $\omega \sim \Delta q_x$. Furthermore when Δq_x changes sign at $\Delta q_x = 0$, and Δq_x becomes positive, the expansion loses its validity as $Im(Q_-)$ becomes negative, and the time oscillating solution ‘disappears’ as expected.

4.5.7 Implications

One expects (or assumes) a saturating nonlinear term to be part of the dynamics of the amplitude equation (4.56). Therefore, we will write the nonlinear amplitude equation as

$$\frac{\partial A}{\partial t} = \tilde{\epsilon}(\Delta q_x) A + i\tilde{\alpha}(\Delta q_x) \frac{\partial A}{\partial Y} + \tilde{\beta}(\Delta q_x) \frac{\partial^2 A}{\partial Y^2} - G|A|^2 A. \quad (4.70)$$

In addition, it was shown in the previous section that there is a bulk state solution, hence we expect G to be real.

At the simplest level, we can write $A(Y, t)$ as a sum of its two types of modes – wall modes

$$A_W(Y, t) = \tilde{A}_W(\Upsilon, t)e^{iQ_W Y} \quad (4.71)$$

and bulk modes

$$A_B(Y, t) = \tilde{A}_B(\Upsilon, t)(re^{iQ_+ Y} + e^{iQ_- Y}) \quad (4.72)$$

where again $\Upsilon = Y = y$ with the assumption that it contains the slow variations on an even longer length scale than Y .

The amplitude equation (4.70) then implies that

$$\begin{aligned} & \frac{\partial \tilde{A}_W}{\partial t} e^{iQ_W Y} + \frac{\partial \tilde{A}_B}{\partial t} (re^{iQ_+ Y} + e^{iQ_- Y}) \\ &= (\bar{\epsilon} - \bar{\alpha}Q_W - \bar{\beta}Q_W^2)\tilde{A}_W e^{iQ_W Y} + i(\bar{\alpha} + 2\bar{\beta}Q_W)\frac{\partial \tilde{A}_W}{\partial \Upsilon} e^{iQ_W Y} + \bar{\beta}\frac{\partial^2 \tilde{A}_W}{\partial \Upsilon^2} e^{iQ_W Y} \\ &+ [(\bar{\epsilon} - \bar{\alpha}Q_+ - \bar{\beta}Q_+^2)re^{iQ_+ Y} + (\bar{\epsilon} - \bar{\alpha}Q_- - \bar{\beta}Q_-^2)e^{iQ_- Y}] \tilde{A}_B \\ &+ i\left((\bar{\alpha} + 2\bar{\beta}Q_+)re^{iQ_+ Y} + (\bar{\alpha} + 2\bar{\beta}Q_-)e^{iQ_- Y}\right)\frac{\partial \tilde{A}_B}{\partial \Upsilon} \\ &+ \bar{\beta}\frac{\partial^2 \tilde{A}_B}{\partial \Upsilon^2}(re^{iQ_+ Y} + e^{iQ_- Y}) - \text{Nonlinear Term}. \end{aligned} \quad (4.73)$$

As the dispersion relation is $\Gamma = \gamma - i\omega = \bar{\epsilon} - \bar{\alpha}Q - \bar{\beta}Q^2$, (4.62), (4.73) becomes

$$\begin{aligned} & \frac{\partial \tilde{A}_W}{\partial t} f_W(Y) + \frac{\partial \tilde{A}_B}{\partial t} f_B(Y) \\ &= (\Delta\epsilon_W - i\omega)\tilde{A}_W f_W(Y) + i(\bar{\alpha} + 2\bar{\beta}Q_W)\frac{\partial \tilde{A}_W}{\partial \Upsilon} f_W(Y) + \bar{\beta}\frac{\partial^2 \tilde{A}_W}{\partial \Upsilon^2} f_W(Y) \\ &+ \Delta\epsilon_B \tilde{A}_B f_B(Y) + i\left(\bar{\alpha}f_B(Y) + 2\bar{\beta}(rQ_+ e^{iQ_+ Y} + Q_- e^{iQ_- Y})\right)\frac{\partial \tilde{A}_B}{\partial \Upsilon} \\ &+ \bar{\beta}\frac{\partial^2 \tilde{A}_B}{\partial \Upsilon^2} f_B(Y) \\ &- G\{|\tilde{A}_W|^2 \tilde{A}_W \cdot |f_W(Y)|^2 f_W(Y) + 2|\tilde{A}_B|^2 \tilde{A}_W \cdot |f_B(Y)|^2 f_W(Y) \end{aligned}$$

$$\begin{aligned}
& + (\tilde{A}_B^* \tilde{A}_W) \tilde{A}_W \cdot f_B^*(Y) f_W^2(Y) \\
& + |\tilde{A}_B|^2 \tilde{A}_B \cdot |f_B(Y)|^2 f_B(Y) + 2 |\tilde{A}_W|^2 \tilde{A}_B \cdot |f_W(Y)|^2 f_B(Y) \\
& + (\tilde{A}_W^* \tilde{A}_B) \tilde{A}_B \cdot f_W^*(Y) f_B^2(Y) \}, \tag{4.74}
\end{aligned}$$

where $\Delta\epsilon_W = \tilde{\epsilon} - \tilde{\epsilon}_c^W$ and $\Delta\epsilon_B = \tilde{\epsilon} - \tilde{\epsilon}_c^B$, and $\tilde{\epsilon}_c^W$ and $\tilde{\epsilon}_c^B$ are the zero growth (or critical onset) $\tilde{\epsilon}$'s for the wall mode $f_W(Y) = e^{iQ_W Y}$, and bulk mode, $f_B(Y) = (r e^{iQ+Y} + e^{iQ-Y})$, respectively.

To properly project out the dynamical equations for \tilde{A}_W and \tilde{A}_B , one needs to find the eigenvectors of the adjoint linear operator and the adjoint boundary conditions to (4.70) and (4.61). We found the adjoint operator to be

$$-\frac{\partial B}{\partial t} = (\tilde{\epsilon}a + i\tilde{\alpha} \frac{\partial}{\partial Y} + \tilde{\beta} \frac{\partial^2}{\partial Y^2})B \tag{4.75}$$

and the adjoint boundary conditions at $Y = 0$ to be

$$\eta_2^* B'' + i(\eta_1^* + 2\eta_2^* \tilde{\alpha} \tilde{\beta}^{-1}) B' + (\eta_0^* - \eta_1^* \tilde{\alpha} \tilde{\beta}^{-1} - \eta_2^* (\tilde{\alpha} \tilde{\beta}^{-1})^2) B = 0,$$

where $B'' = \frac{\partial^2 B}{\partial Y^2}|_{Y=0}, \dots$, and also $\eta_2^* = \eta_2$.

Though we did not find the adjoint eigenvectors and thus project out the equations for \tilde{A}_W and \tilde{A}_B , we can still write down model dynamical equations for the two. In the boundary region, where Υ is small and the spatial variation of \tilde{A}_W and \tilde{A}_B is negligible, we expect to be able to extract the mode equations describing the dynamics of \tilde{A}_W and \tilde{A}_B in the wall region. Leaving out the negligible spatial dependence one obtains:

$$\frac{\partial \tilde{A}_W}{\partial t} = (\Delta\epsilon_W - i\omega) \tilde{A}_W - (g_W^r + i g_W^i) |\tilde{A}_W|^2 \tilde{A}_W$$

$$\begin{aligned}
& - (g_1^r + ig_1^i)(\tilde{A}_B^* \tilde{A}_W) \tilde{A}_W - (g_2^r + ig_2^i) |\tilde{A}_B|^2 \tilde{A}_W \\
& \text{— perhaps other nonlinear coupling terms} \tag{4.76}
\end{aligned}$$

and

$$\begin{aligned}
\frac{\partial \tilde{A}_B}{\partial t} &= \Delta \epsilon_B \tilde{A}_B - g_B \cdot |\tilde{A}_B|^2 \tilde{A}_B - h_1 (\tilde{A}_W^* \tilde{A}_B) \tilde{A}_B - h_2 \cdot |\tilde{A}_W|^2 \tilde{A}_B \\
& \text{— perhaps other nonlinear coupling terms,} \tag{4.77}
\end{aligned}$$

where the g 's and h 's are real-valued parameters.

4.5.8 Dynamical Mode Equations for the Boundary Region

Using (4.76) and (4.77) we can now write down coupled mode equations for \tilde{A}_W and \tilde{A}_B which will describe the dynamics observed in the numerical simulations of the transition region. Writing \tilde{A}_W and \tilde{A}_B in terms of their real-valued magnitudes a_W and a_B , and phases, ϕ_W and ϕ_B , (4.76) and (4.77) become

$$\begin{aligned}
\frac{\partial a_W}{\partial t} &= \Delta \epsilon_W a_W - g_2^r a_B^2 a_W - g_W^r a_W^3 \\
& - [g_1^r \cos(\phi_W - \phi_B) - g_1^i \sin(\phi_W - \phi_B)] a_B a_W^2 \tag{4.78}
\end{aligned}$$

$$\begin{aligned}
\frac{\partial \phi_W}{\partial t} &= -\omega - g_2^i a_B^2 - g_W^i a_W^2 \\
& - [g_1^i \cos(\phi_W - \phi_B) + g_1^r \sin(\phi_W - \phi_B)] a_W a_B \tag{4.79}
\end{aligned}$$

$$\frac{\partial a_B}{\partial t} = \Delta \epsilon_B a_B - h_2 a_W^2 a_B - g_B a_B^3 - h_1 \cos(\phi_W - \phi_B) a_W a_B^2 \tag{4.80}$$

$$\frac{\partial \phi_B}{\partial t} = h_1 \sin(\phi_W - \phi_B) a_W a_B. \tag{4.81}$$

However, as the bulk state extends to ‘infinity’, we expect the phase of \tilde{A}_B to be preferentially pinned to its bulk phase, and thus introduce a damping term,

$-\rho a_B^2 \sin(\phi_B - \phi_B^\infty)$, (or $-\rho a_B^2(\phi_B - \phi_B^\infty)$), into the RHS of (4.81). Additionally, we can without loss of generality, set $\phi_B^\infty = 0$.

There are many unknown parameters in this set of coupled equations, but we do have a few constraints. Most importantly,

$$\Delta\epsilon_W - \Delta\epsilon_B = (\tilde{\epsilon} - \tilde{\epsilon}_c^W) - (\tilde{\epsilon} - \tilde{\epsilon}_c^B) = \tilde{\epsilon}_c^B - \tilde{\epsilon}_c^W$$

therefore $\Delta\epsilon_W - \Delta\epsilon_B$ varies linearly in Δq_x (for small Δq_x) and is constant for fixed Δq_x . At $q_x = q_{xc}$, $\tilde{\epsilon}_c^B - \tilde{\epsilon}_c^W < 0$, but as Δq_x decreases ($\Delta q_x < 0$ in the interesting region), $\tilde{\epsilon}_c^B - \tilde{\epsilon}_c^W$ becomes positive; for example, see the phase diagram in Fig.(4-19).

Naturally, ω , for which we have $\omega \sim \Delta q_x$, goes to zero as $\Delta q_x \rightarrow 0$. Furthermore, we argue that the imaginary parts of the complex coefficients (the g^i), for symmetry reasons, are expandable in odd powers of ω , viz, if $\omega \rightarrow -\omega$, $g^i \rightarrow -g^i$. And hence, when $\Delta q_x \rightarrow 0$, $\omega \rightarrow 0$, and $g^i \rightarrow 0$.

In addition, in order for the magnitudes of the amplitudes to saturate at the cubic-order level, we will assume that

$$g_B > 0, g_W^r > 0, g_2^r > 0,$$

and as it seems that the term $h_2 a_W^2 a_B$ is not important, we will take $h_2 = 0$ (otherwise, we would expect $h_2 > 0$). For similar reasons, we will assume $g_1^r > 0$ and $h_1 > 0$. Finally, because we observe that the nonlinear frequency (in magnitude) decreases as ϵ increases, we will also assume $g_2^i > 0$ and $g_W^i > 0$ for $\omega < 0$.

Solving the coupled ordinary differential equations (4.78) - (4.81), we find that the various nonlinear steady states in the wall state - bulk state transition region can

be explained in terms of the different types of fixed points and limit cycles of these dynamical equations. Since for the simulations of the Swift-Hohenberg equation, the variable we are looking at is actually $\psi = Ae^{i(q_{oc} + \Delta q_0)x} e^{iq_{vc}y} + c.c.$, and for constant and small Y , $A = \eta \tilde{A}_W + \tilde{A}_B$, where η is some complex number, the quantity that is significant is A . We will just study $A = \tilde{A}_W + \tilde{A}_B$, since the actual value of η will not affect the qualitative results.

‘Projecting’ the trajectories of the variables a_W , a_B , ϕ_W and ϕ_B in phase space onto the complex plane $A = ae^{i\phi} = (Re A, Im A) = (a_W \cos \phi_W + a_B \cos \phi_B, a_W \sin \phi_W + a_B \sin \phi_B)$ we find that (not counting the trivial solution $A = 0$, also a fixed point), there are two types of solutions –

- (nontrivial) fixed points, and
- projections of limit cycles.

There are two types of limit cycles – those for which their projection in the A -plane encircles the origin ($A = 0$), and those for which their projection does not. In addition, the cross-over from the latter to the former is smooth – the limit cycle in some sense just gets bigger as a_W increases and its projection passes through $A = 0$!

Thus we identify the steady one-states with the fixed points, the oscillating one-states with limit cycles not encircling the origin of A , (the phase of A , ϕ , cannot be seen as monotonically increasing or decreasing), the wall-plus-bulk states with limit cycles encircling the origin of A , (ϕ in this case can be seen as monotonically increasing or decreasing), and wall states also with limit cycles encircling the origin of

A , but for which $a_B = 0$. This explains the smooth change in frequency through the transition from oscillating one-state to wall-plus-bulk state, as well as the observation that near this transition, periodically the amplitude for the entire boundary region approaches zero (this is just the limit cycle passing through $A = 0$).

One further feature of the phase diagram explained by the model equations, (4.78) - (4.81), is the existence of steady one-states at values of ϵ just above ϵ_c^W when $\epsilon_c^W > \epsilon_c^B$. Equation (4.78) states that the effective growth rate for the traveling-wave wall state is $\epsilon_{eff} = \Delta\epsilon_W - g_2^r a_W^2$, thus if the bulk state onsets *before* the wall state, it *suppresses* the wall state at the linear level. This is the justification for the comment made in §4.5.4 with regard to the frequency just changing linearly through the oscillating one-state to the steady one-state transition – the only reason there is a steady one-state instead of an oscillating one-state is because $a_W \rightarrow 0$, not because $\frac{\partial\phi_W}{\partial t} \rightarrow 0$ as in the wall-plus-bulk state to steady one-state transition.

This leads to another observation and comment. For the steady one-states below (in the sense of ϵ) the oscillating one-states, we observed that to approach its final steady state, the system took the route of decaying oscillations. For the steady one-states above the wall-plus-bulk states, this was not the case, instead the route was essentially one of monotonically approaching the steady-state value. This would seem to correspond to spiralling into the fixed point for the former case, and approaching the fixed point linearly for the latter. In the region very close to the disappearing point, where there are only steady one-states for all values of ϵ , it appears that the

spiral trajectories around the fixed points ‘unwind’ as ϵ increases, probably going continuously from a stable fixed point with complex eigenvalues to a stable fixed point with real eigenvalues.

4.5.9 Numerical Study of the Dynamical Mode Equations

In this section we will present some results (mainly figures) from simulating equations (4.78) - (4.81) numerically (using *Mathematica*). In this particular study, we took

$$\tilde{\epsilon}_c^W = 4\Delta q_x,$$

$$\tilde{\epsilon}_c^B = -0.04 + 3\Delta q_x,$$

$$\text{and } \omega = \Delta q_x.$$

We will show the phase space trajectories for three values of Δq_x , $\Delta q_x = -0.1, -0.02$ and -0.005 . For the first two values (the ones larger in magnitude) we evolved the reduced equations

$$\frac{da_W}{dt} = \Delta\epsilon_W a_W - g_2^r a_B^2 a_W - g_W^r a_W^3, \quad (4.82)$$

$$\frac{da_B}{dt} = \Delta\epsilon_B a_B - g_B a_W^3, \quad (4.83)$$

$$\begin{aligned} \frac{d\phi_W}{dt} = & -\omega - g_2^i a_B^2 - g_W^i a_W^2 \\ & -(g_1^i \cos(\phi_W - \phi_B)) + g_1^r \sin(\phi_W - \phi_B) a_W a_B, \end{aligned} \quad (4.84)$$

$$\frac{d\phi_B}{dt} = -\rho a_B^2 \phi_B + h_1 \sin(\phi_W - \phi_B) a_B a_W, \quad (4.85)$$

which appear to contain the dynamics of the wall-plus-bulk state and the oscillating one-state and their various transitions. For $\Delta q_x = -0.1$, $\tilde{\epsilon}_c^W = -0.40$ and $\tilde{\epsilon}_c^B = -0.34$

- this is the case $\tilde{\epsilon}_c^W < \tilde{\epsilon}_c^B$. For $\Delta q_x = -0.02$, $\tilde{\epsilon}_c^W = -0.08$ and $\tilde{\epsilon}_c^B = -0.10$, and $\tilde{\epsilon}_c^W > \tilde{\epsilon}_c^B$.

For the case $\Delta q_x = -0.1$, and the parameters $g_W^r = 1$, $g_W^i = 0.1$, $g_1^r = 0.2$, $g_1^i = -0.25$, $g_2^r = 0.1$, $g_2^i = 0.2$, $g_B = 2.5$, $h_1 = 0.2$, and $\rho = 1$, as $\bar{\epsilon}$ is increased, we see a transition from wall state to wall-plus-bulk state to steady one-state as anticipated. (See Figures(4-36) - (4-39).) In the case $\Delta q_x = -0.02$, (and the same parameters), we see the transition from steady one-state to oscillating one-state to wall-plus-bulk state to steady one-state. (See Figures(4-40) - (4-43).) For $\Delta q_x = -0.005$, we took the limit of small ω , and let $g^i \rightarrow 0$. In this case, the reduced equations used above were not sufficient to reproduce the expected dynamics, and the magnitudes a_W and a_B needed to be coupled to the phase variables. The equations evolved were

$$\frac{da_W}{dt} = \Delta\epsilon_W a_W - g_2^r a_B^2 a_W - g_W^r a_W^3 - g_1^r \cos(\phi_W - \phi_B) a_B a_W^2, \quad (4.86)$$

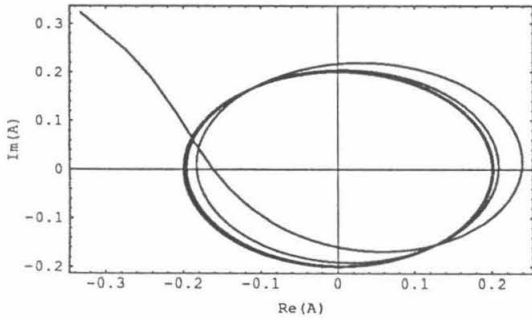
$$\frac{da_B}{dt} = \Delta\epsilon_B a_B - g_B a_W^3 - h_1 \cos(\phi_W - \phi_B) a_W a_B^2, \quad (4.87)$$

$$\frac{d\phi_W}{dt} = -\omega - g_1^r \sin(\phi_W - \phi_B) a_W a_B, \quad (4.88)$$

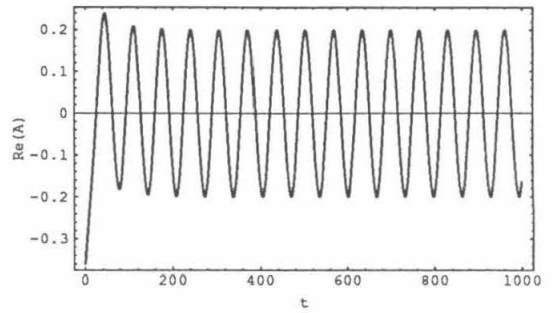
$$\frac{d\phi_B}{dt} = -\rho a_B^2 \phi_B + h_1 \sin(\phi_W - \phi_B) a_W a_B. \quad (4.89)$$

For the parameters $g_W^r = 1$, $g_1^r = 2$, $g_2^r = 0.1$, $g_B = 2.5$, $h_1 = 0.2$, and $\rho = 1$, the long-time solution to these equations was always a fixed point, and in addition, the spirals of the fixed point unwound as ϵ was increased. (See Figures (4-44) - (4-46).)

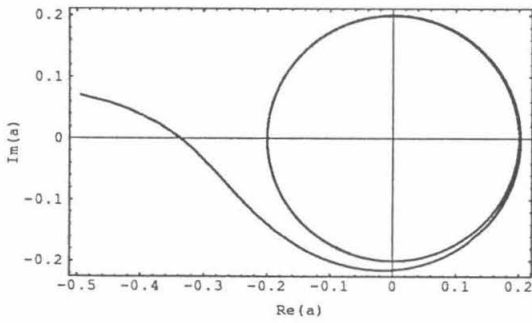
(a)



(b)



(c)



(d)

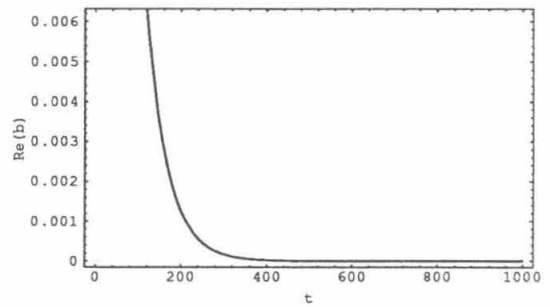
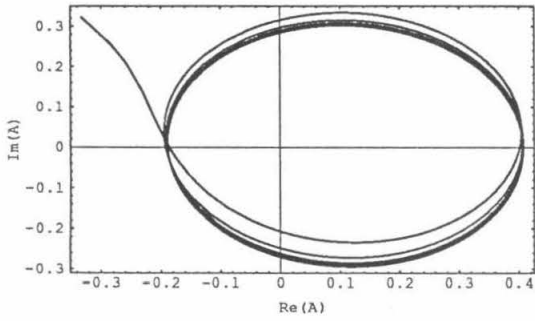
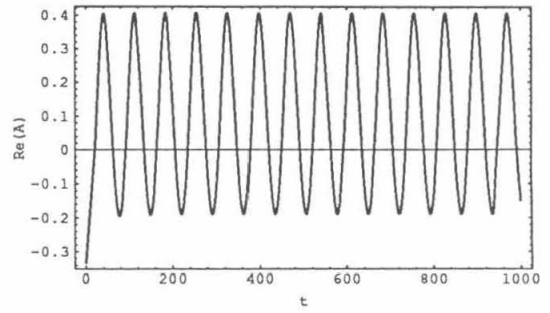


Figure 4-36: $q_x = -0.1, \tilde{\epsilon} = -0.36$. "Wall state" trajectory: (a) complex A -plane; (b) $\text{Re}(A) \sim \psi$ vs t ; (c) complex \tilde{A}_W -plane; (d) $a_B \cos \phi_B$ vs t . (For details see text.)

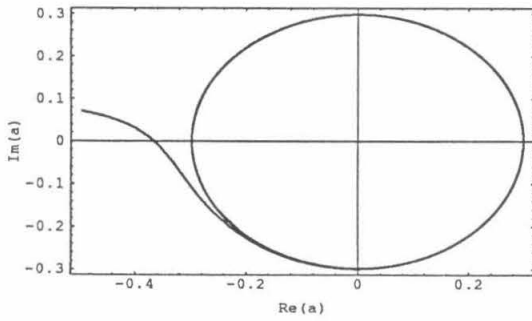
(a)



(b)



(c)



(d)

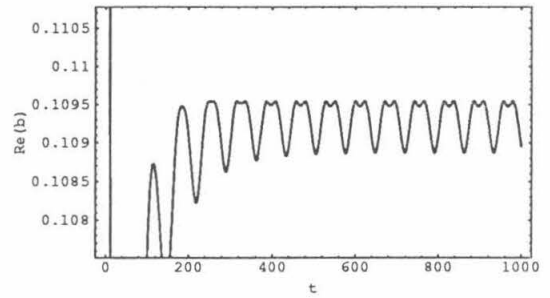
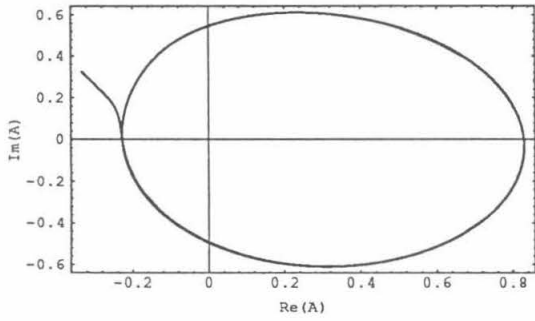
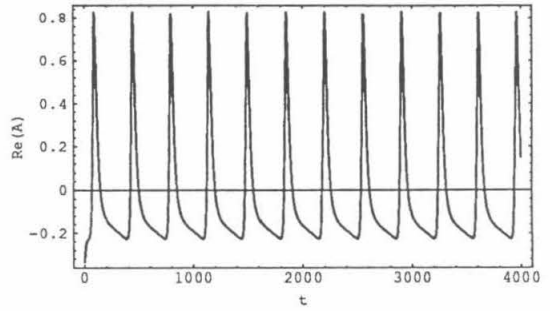


Figure 4-37: $q_x = -0.1, \tilde{\epsilon} = -0.31$. "Wall-plus-bulk state" trajectory: (a) A -plane; (b) $\text{Re}(A) \sim \psi$ vs t ; (c) \tilde{A}_W -plane; (d) $a_B \cos \phi_B$ vs t .

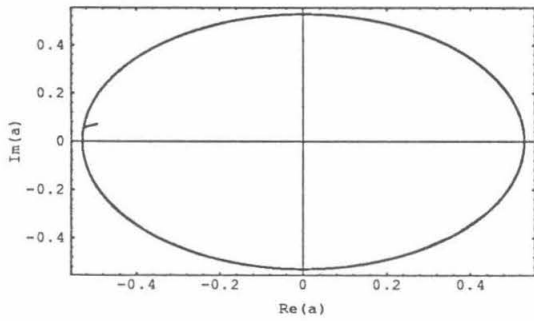
(a)



(b)



(c)



(d)

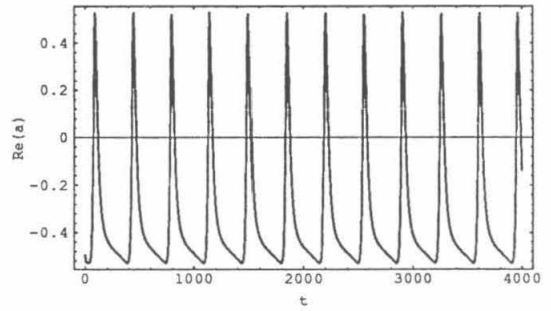
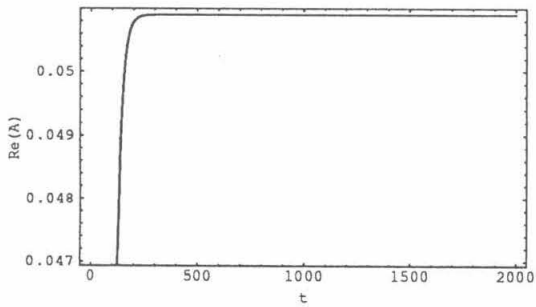
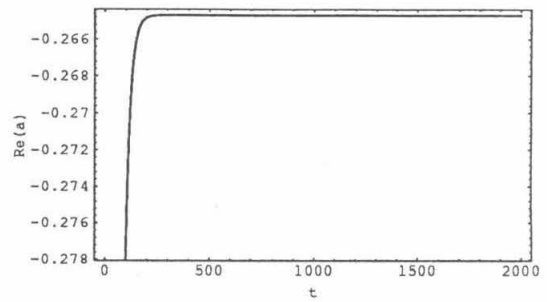


Figure 4-38: $q_x = -0.1, \tilde{\epsilon} = -0.11$. "Wall-plus-bulk state" trajectory: (a) A -plane; (b) $\text{Re}(A) \sim \psi$ vs t ; (c) \tilde{A}_W -plane; (d) $a_W \cos \phi_W$ vs t .

(a)



(b)



(c)

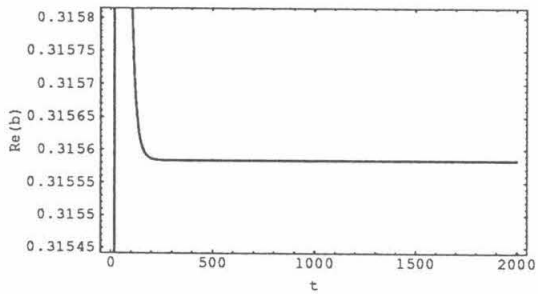
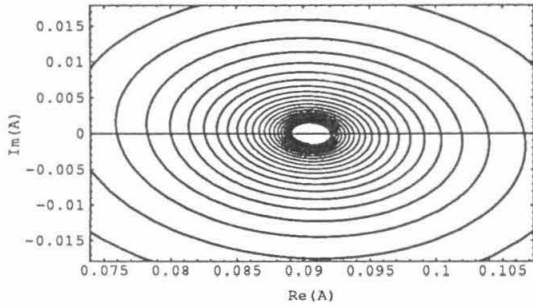
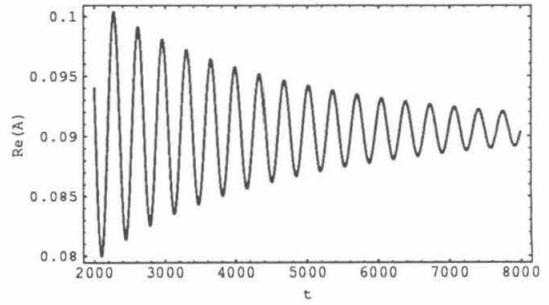


Figure 4-39: $q_x = -0.1, \tilde{\epsilon} = -0.06$. "Steady one-state" trajectory: (a) $\text{Re}(A) \sim \psi$ vs t ; (b) $a_W \cos \phi_W$ vs t ; (c) $a_B \cos \phi_B$ vs t .

(a)



(b)



(c)

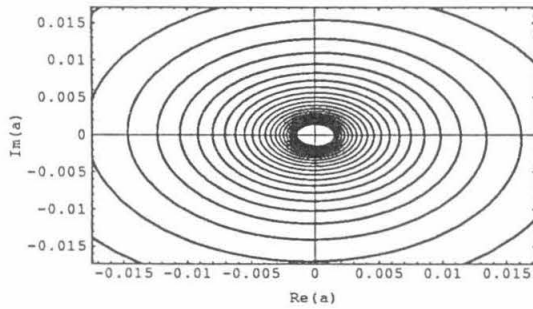
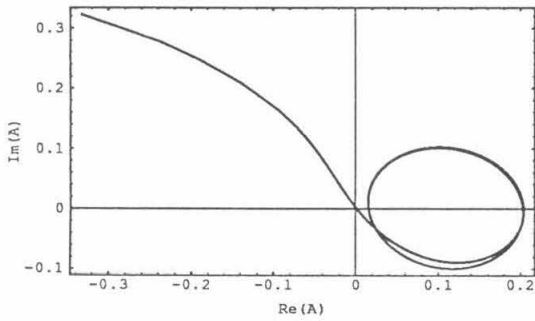
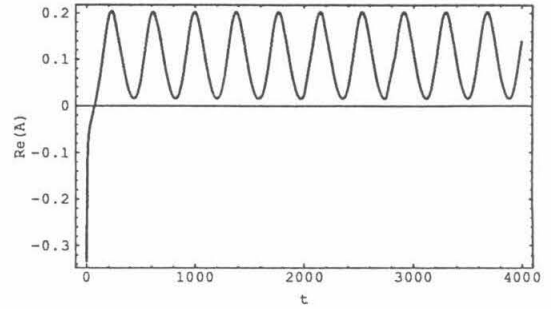


Figure 4-40: $q_x = -0.02, \tilde{\epsilon} = -0.0795$. "Steady one-state" trajectory: (a) A -plane; (b) $\text{Re}(A) \sim \psi$ vs t ; (c) A_W -plane.

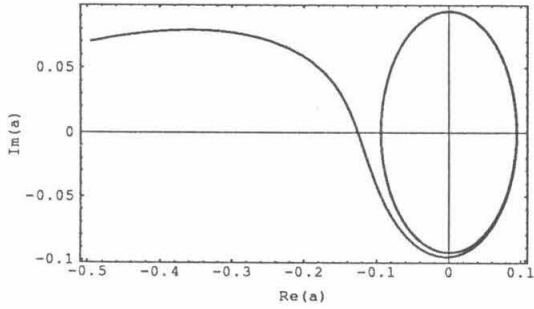
(a)



(b)



(c)



(d)

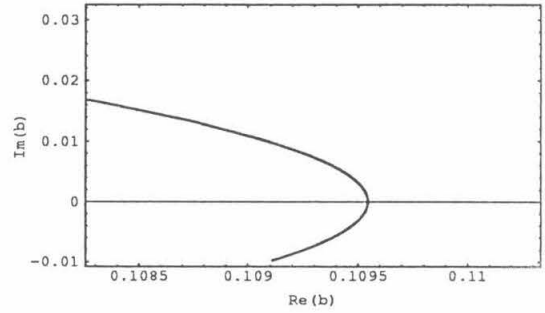
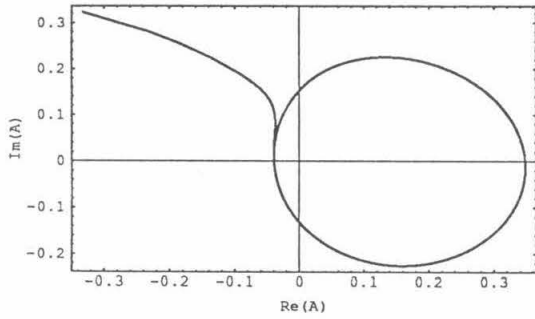
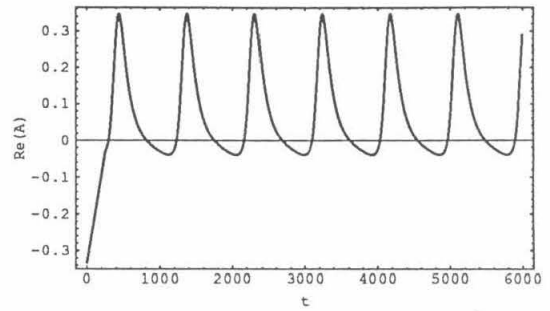


Figure 4-41: $q_x = -0.02, \tilde{\epsilon} = -0.07$. "Oscillating one-state" trajectory: (a) A -plane; (b) $\text{Re}(A) \sim \psi$ vs t ; (c) \tilde{A}_W -plane; (d) \tilde{A}_B -plane.

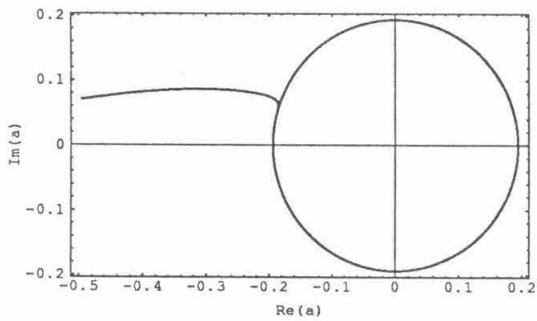
(a)



(b)



(c)



(d)

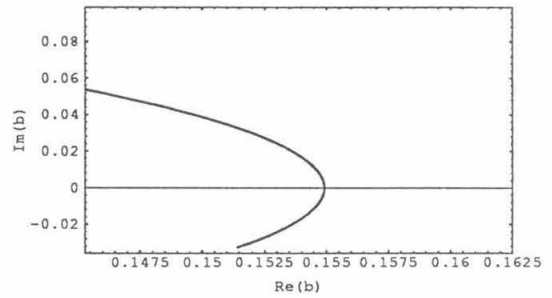
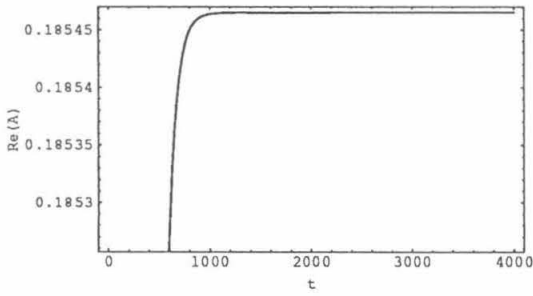
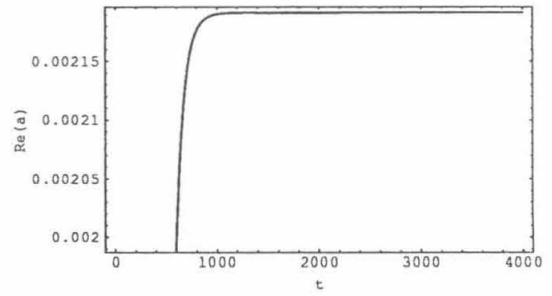


Figure 4-42: $q_x = -0.02, \tilde{\epsilon} = -0.04$. “Wall-plus-bulk state” trajectory: (a) A -plane; (b) $\text{Re}(A) \sim \psi$ vs t ; (c) \tilde{A}_W -plane; (d) \tilde{A}_B -plane.

(a)



(b)



(c)

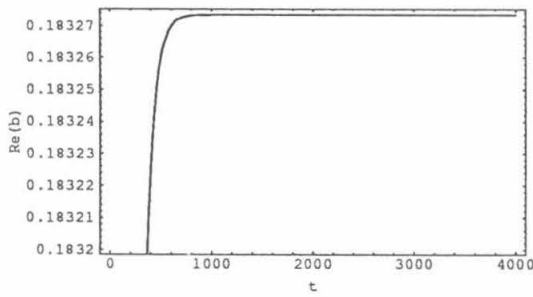
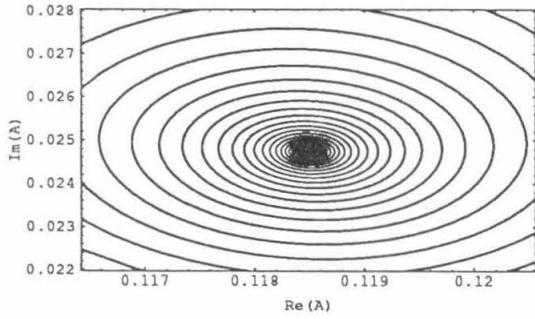
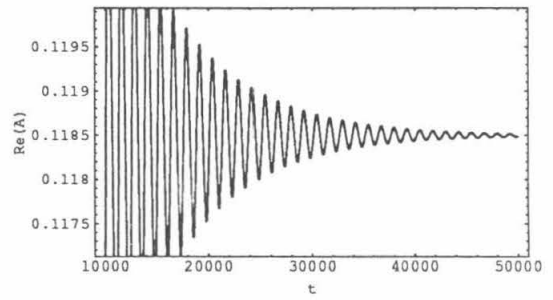


Figure 4-43: $q_x = -0.02, \tilde{\epsilon} = -0.01$. “Steady one-state” trajectory: (a) $\text{Re}(A) \sim \psi$ vs t ; (b) $a_W \cos \phi_W$ vs t ; (c) $a_B \cos \phi_B$ vs t .

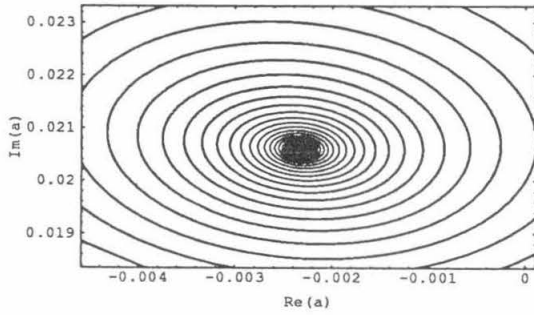
(a)



(b)



(c)



(d)

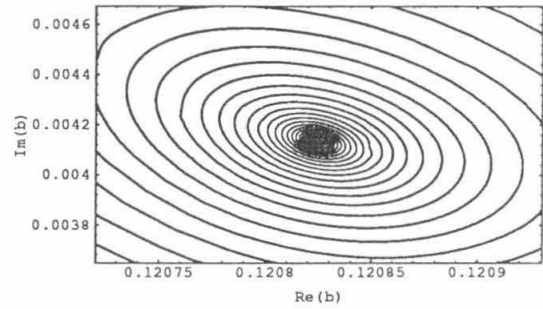
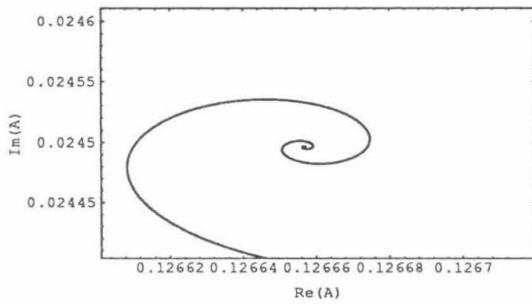
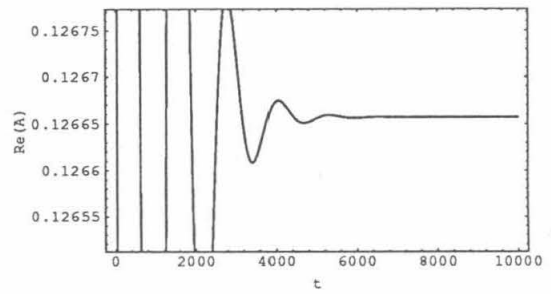


Figure 4-44: $q_x = -0.005$, $\tilde{\epsilon} = -0.0185$. “Steady one-state” trajectory: (a) A -plane; (b) $\text{Re}(A) \sim \psi$ vs t ; (c) \tilde{A}_W -plane; (d) \tilde{A}_B -plane.

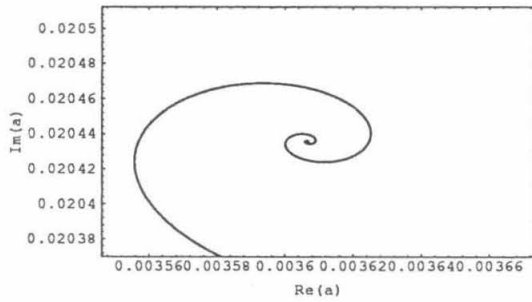
(a)



(b)



(c)



(d)

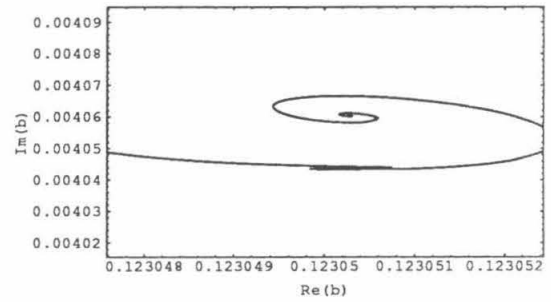


Figure 4-45: $q_x = -0.005, \tilde{\epsilon} = -0.017$. “Steady one-state” trajectory: (a) A -plane; (b) $\text{Re}(A) \sim \psi$ vs t ; (c) \tilde{A}_W -plane; (d) \tilde{A}_B -plane.

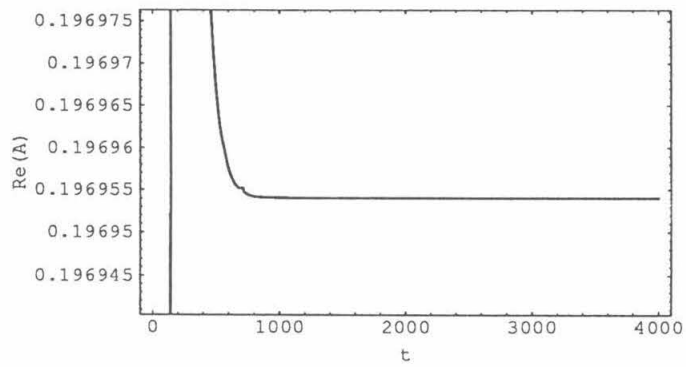


Figure 4-46: $q_x = -0.005, \tilde{\epsilon} = 0$. "Steady one-state" trajectory: $\text{Re}(A) \sim \psi$ vs t .

Chapter 5

Conclusion and Future Work

In this thesis we have shown the existence of a new type of geometry-independent state in nonequilibrium pattern-forming systems – the traveling-wave wall state. We showed its existence is not just confined to rotating Rayleigh-Bénard convection systems, but can exist generically in systems with broken reflection symmetry and side-walls. Furthermore, this state, which exists in an idealized semi-infinite system, possesses the intriguing feature of *disappearing before* the reflection-symmetry-breaking parameter goes to zero. At its point of disappearance, the linear wall state also becomes a bulk state of infinite extent and zero frequency. How the wall state and the bulk state merge was a major thrust to this work.

A detailed numerical study was undertaken of the wall – bulk transition region, and coupled dynamical mode equations for the wall mode and bulk mode were proposed. We were able to use these equations to successfully model the dynamics observed in the wall state – bulk state transition region on a qualitative level, leading to an understanding of the underlying dynamics of the region. This understanding indicates that it is the nonlinear effects involved in the dynamic coupling of the wall

and bulk states which hold the key to understanding how the wall and bulk states come together; this question is of especial relevance when one wants to apply the understanding gained in idealized infinite (or semi-infinite) systems to real experimental systems which are always finite.

More detailed experiments on rotating Rayleigh-Bénard convection systems [18], especially at small rotation rates, would conversely be useful in testing the theoretical models and ideas of the transition region.

There are many avenues for future work on the effects of walls and wall states on bulk state dynamics. The possible effects of wall states on the dynamics of the Küpper-Lortz instability were mentioned earlier. Before we show some pictures that demonstrate an effect, we will first mention another interesting observation of the effects of the wall state – bulk state interaction. In studying the wall – bulk transition region, when the nonlinear steady-state was either a wall-plus-bulk state or an oscillating one-state, it was observed that the two wall states at either boundary tended to ‘break’ (in the case of wall-plus-bulk states) or ‘jerk back’ (in the case of oscillating one-states) at the same time! This is despite being separated by a ‘large’ distance. A more precise statement would perhaps be to say that if one plots ψ vs t for different points in the two boundary regions, they will undergo sharp changes at exactly the same time. (See Fig.(5-1).) Clearly the bulk state and wall states are strongly coupled. It would be interesting to understand this in terms of the idealized infinite system bulk and wall states.

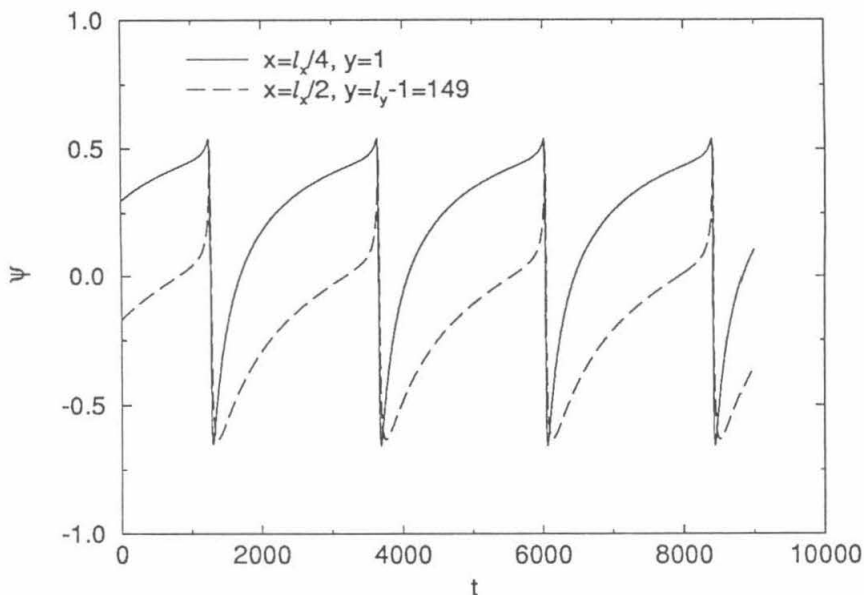


Figure 5-1: $\psi(t)$ for $(x, y) = (l_x/4, 1)$ and $(l_x/2, l_y - 1)$.

Now we conclude with some pictures demonstrating that at least in systems which are not too large, the wall states do affect the bulk dynamics of the Küppers-Lortz instability. These pictures demonstrate a preferential aligning of the bulk rolls along an orientation given by the wall state rolls.

In Fig.(5-2) we would be seeing the domains of ‘preferred’ rolls aligned with the wall rolls moving into the central bulk region.

In Fig.(5-3(a) & (b)), time-slice plots of $\psi(x, t)$ for fixed $y = 49$ and of $\psi(y, t)$ for $x = 32$ respectively clearly demonstrate a preferred orientation of the rolls in the bulk, and a more careful analysis indicates that if the orientation is cycling through $\theta_1 \rightarrow \theta_2 \rightarrow \theta_3 \rightarrow \theta_1$, and θ_1 is the preferred one, then the orientation θ_3 is ‘extremely unstable’ to θ_1 , barely lasting at all. It must remain for future work to understand

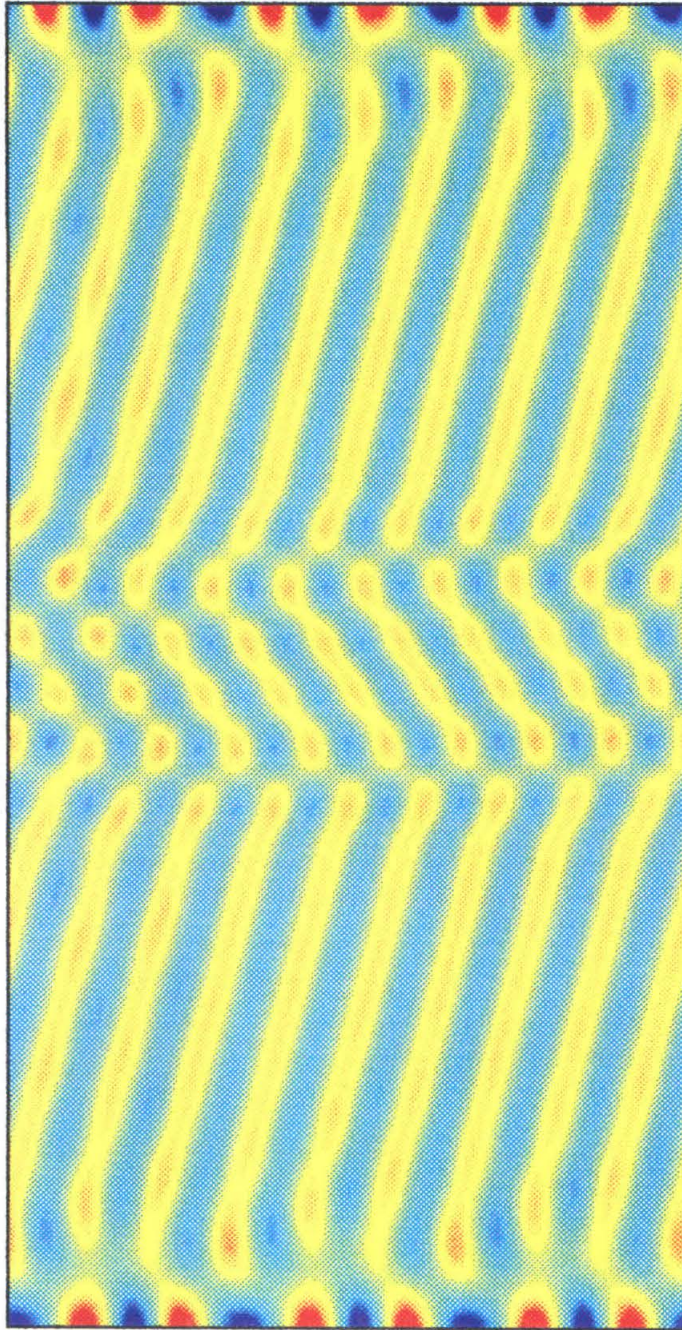


Figure 5-2: $\psi(x, y)$ for $\epsilon = 0.2$, $\lambda = -0.1$, $\mu = -8$, $g_1 = 1$, $g_2 = 2.078$ and $g_3 = 1.2$; the system size is $l_x = 64$, $l_y = 85$ and grid points in the y -direction of $50 + 35 + 50$ for lengths of $25 + 35 + 25$.

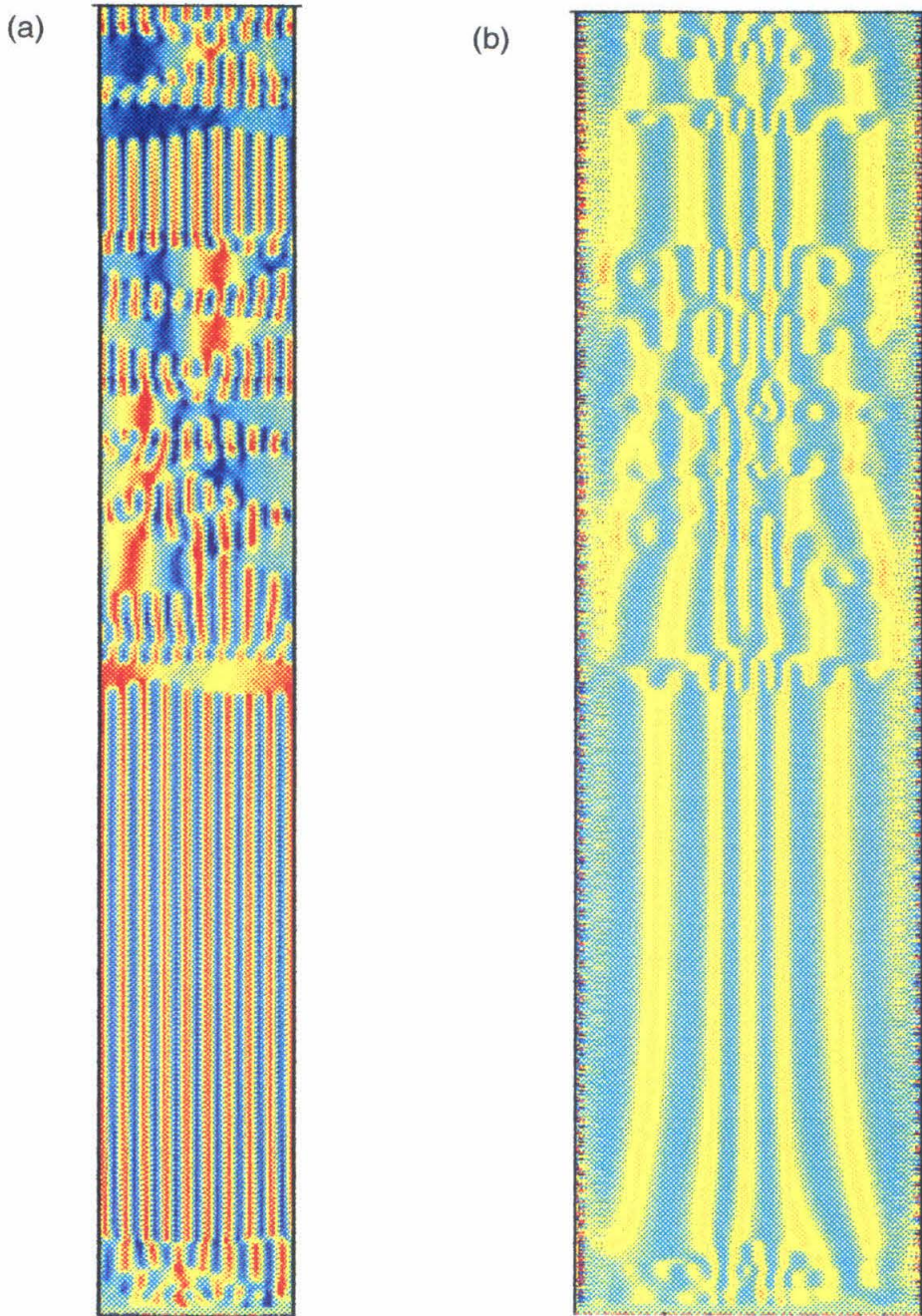


Figure 5-3: (a) $\psi(x, t)$ for $y = 49$; (b) $\psi(y, t)$ for $x = 32$; for the system of Fig.(5-2). Total time is about 1000.

how these and other phenomena carry over into the dynamics of larger systems at a quantitative level.

Appendix A

The Thermal Boundary Condition

In this appendix, we will derive the relationship, (equation (3.13))

$$\mu = K_w k_w \tanh(k_w l_w) \quad (\text{A.1})$$

which is used in the thermal boundary condition, (equation (3.7)),

$$\frac{\partial \theta}{\partial y} - \mu \theta = 0. \quad (\text{A.2})$$

For a sidewall of thickness l_w , one end of which is in contact with the fluid, and the other end with a vacuum, the thermal boundary conditions on the temperature deviation θ_w in the sidewall are (see Fig.(A-1) for the coordinate system),

$$\theta_w = 0 \quad \text{at} \quad z = 0, 1 \quad (\text{A.3})$$

(perfectly conducting plates on the top and bottom)

$$\frac{\partial \theta_w}{\partial y} = 0 \quad \text{at} \quad y = -l_w \quad (\text{A.4})$$

(conservation of heat)

$$\text{and} \quad \theta_w = \theta \quad (\text{A.5})$$

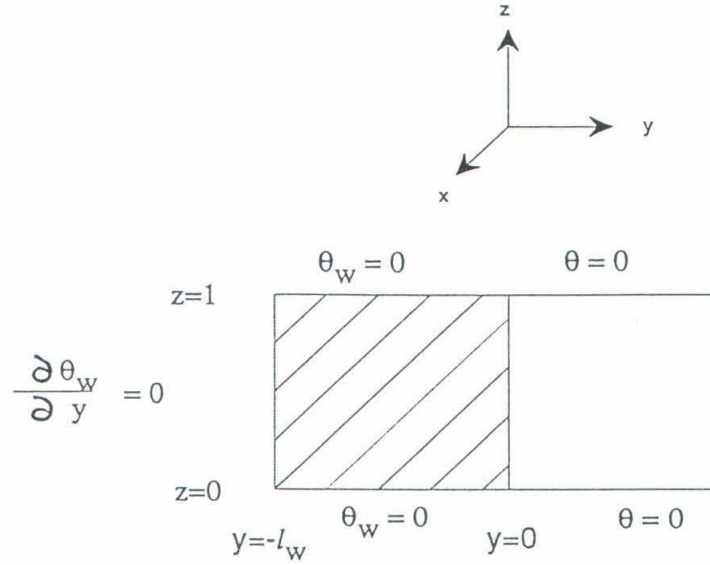


Figure A-1: Coordinate system for sidewall - fluid boundary

$$K_w \frac{\partial \theta_w}{\partial y} = \frac{\partial \theta}{\partial y} \quad \text{at } y = 0, \quad (\text{A.6})$$

where K_w is the ratio of the thermal conductivities of the sidewall to the fluid.

In the sidewall layer ($-l_w < y < 0$), the governing equation is the heat equation

$$\frac{\partial \theta_w}{\partial t} = \kappa_w \nabla^2 \theta_w, \quad (\text{A.7})$$

where κ_w is the thermal diffusivity of the sidewall.

Since the boundary conditions at $z = 0, 1$ are $\theta_w = 0$, we can expand

$$\theta_w(x, y, z, t) = \sum_n \sin(n\pi z) e^{iqz} f_n(y, t) + c.c., \quad (\text{A.8})$$

and as we will just be looking for the lowest order $n = 1$ mode in the fluid, we need only consider the $n = 1$ mode here as well. Thus let us write

$$\theta_w(x, y, z, t) = \sin(\pi z) e^{iqz} e^{\Gamma t} g(y) + c.c.. \quad (\text{A.9})$$

Substituting this into the heat equation gives

$$g(y) = g_+ e^{k_w y} + g_- e^{-k_w y}, \quad (\text{A.10})$$

where $k_w^2 = q_x^2 + \pi^2 + \kappa_w^{-1} \Gamma$. The boundary condition (A.4) is thus

$$\frac{\partial g}{\partial y} = k_w (g_+ e^{-k_w l_w} - g_- e^{k_w l_w}) = 0 \quad \text{at } y = -l_w, \quad (\text{A.11})$$

hence

$$\frac{g_+}{g_-} = e^{2k_w l_w}. \quad (\text{A.12})$$

Using this ratio in (A.10) leads to the form for $g(y)$, $g(y) = g_0 \cosh(k_w(y + l_w))$, where g_0 is some arbitrary constant. Now we use the two boundary conditions (A.5) and (A.6) at $y = 0$ linking θ and θ_w to find the boundary condition on θ at $y = 0$.

Let us write

$$\theta(x, y, z, t) = \sin(\pi z) e^{iq_w x} e^{\Gamma t} h(y) + c.c., \quad (\text{A.13})$$

then (A.5) implies

$$h(0) = g_0 \cosh(k_w l_w), \quad (\text{A.14})$$

and (A.6) implies

$$h'(0) = K_w g_0 k_w \sinh(k_w l_w). \quad (\text{A.15})$$

So we find the boundary condition on θ at $y = 0$ to be $\frac{\partial \theta}{\partial y} = \mu \theta$, where $\mu = K_w k_w \tanh(k_w l_w)$.

References

- [1] M.C. Cross, P.C. Hohenberg, *Rev. Mod. Phys.* **65**, 851 (1993).
- [2] P. Manneville, *Dissipative Structures and Weak Turbulence*, Academic Press, Boston, 1990.
- [3] D. J. Tritton, *Physical Fluid Dynamics*, Second Edition, Clarendon Press, Oxford, p163, 1988.
- [4] S. Chandrasekhar, *Hydrodynamic and Hydromagnetic Stability*, Oxford University Press, Oxford, 1961.
- [5] L. Kramer, P.C. Hohenberg, *Physica* **13D**, 357 (1984).
- [6] M.C. Cross, E.Y. Kuo, *Physica* **D59**, 90 (1992).
- [7] A.C. Newell, J.A. Whitehead, *J. Fluid Mech.* **38**, 279 (1969).
- [8] P. Bergé, M. Dubois, *Contemp. Phys.* **25**, 535 (1984).
- [9] H.T. Rossby, *J. Fluid Mech.* **36**, 309 (1969).
- [10] G. Veronis, *J. Fluid Mech.* **5**, 401 (1959).
- [11] J.C. Buell and I. Catton, *Phys. Fluids* **26**, 892 (1983).

- [12] F. Zhong, R.E. Ecke and V. Steinberg, *Phys. Rev. Lett.* **67**, 2473 (1991).
- [13] L. Ning and R.E. Ecke, *Phys. Rev. E* **47**, 3326 (1993).
- [14] Li Ning, private communication.
- [15] Y.S. Touloukian, R.W. Powell, C.Y. Ho, P.G. Klemens, Editors, *Thermal Conductivity, Nonmetallic Solids, (Thermophysical Properties of Matter, Vol.2)*, p960, IFI/Plenum, New York, 1970. Y.S. Touloukian, R.W. Powell, C.Y. Ho, M.C. Nicolaou, Editors, *Thermal Diffusivity, (Thermophysical Properties of Matter, Vol.10)*, p602, IFI/Plenum, New York, 1973.
- [16] V. Croquette, *Contemp. Phys.* **30**, 113, (1989).
- [17] H.F. Goldstein, E. Knobloch, I. Mercader and M. Net, *J. Fluid Mech.* **248**, 583 (1993).
- [18] R.E. Ecke, F. Zhong, E. Knobloch, *Europhys. Lett.*, **19**, 177 (1992).
- [19] E.Y. Kuo and M.C. Cross, *Phys. Rev. E* **47**, 2245 (1993).
- [20] T. Clune and E. Knobloch, *Phys. Rev. E* **47**, 2536 (1993).
- [21] J. Herrmann and F.H. Busse, *J. Fluid Mech.* **255**, 183 (1993).
- [22] D. Meiron, private communication.
- [23] J.B. Swift and P.C. Hohenberg, *Phys. Rev. A* **15**, 319 (1977).
- [24] G. Küppers and D. Lortz, *J. Fluid Mech.* **35**, 609 (1969).

- [25] G. Küppers, *Physics Lett.* **32A**, 7 (1970).
- [26] F.H. Busse and K.E. Heikes, *Science* **208**, 175 (1980).
- [27] R.M. May and W.J. Leonard, *SIAM J. Appl. Math.* **29**, 243 (1975).
- [28] Y. Tu and M.C. Cross, *Phys. Rev. Lett.* **69**, 2515 (1992).
- [29] Y. Tu, private communication.
- [30] M.C. Cross, P.G. Daniels, P.C. Hohenberg, E.D. Siggia, *J. Fluid Mech.* **127**, 155 (1983).